ISSN 2234-8409 (print)
ISSN 2234-8395 (online)

http://www.jees.kr

JEES

Journal of Electromagnetic Engineering and Science

Volume 17, No. 3
July 2017

KIEES

Journal of Electromagnetic Engineering and Science Volume 17, No.3 July 2017 KIEES

JEES Journal of Electromagnetic Engineering and Science

JEES
Journal of
Electromagnetic Engineering
and Science

Jul. 2017
Vol. 17 No. 3

ISSN 2234-8409 (Print)
ISSN 2234-8395 (Online)

Aims and Scope

The Journal of Electromagnetic Engineering and Science (**JEES**) is an official English-language journal of the Korean Institute of Electromagnetic and Science (**KIEES**). This journal was launched in 2001 and has been published quarterly since 2003. It is currently registered with the National Research Foundation of Korea and also indexed in CrossRef and EBSCO. The objective of **JEES** is to publish academic as well as industrial research results and discoveries in electromagnetic engineering and science. The particular scope of the journal includes electromagnetic field theory and its applications; high frequency components, circuits, and systems; antennas; electromagnetic wave environments; and relevant industrial developments. In addition to the regular stream of contributed papers, the journal occasionally publishes special issues on specific topics of current interest, to promote a focused coverage of the selected topics. In addition, **JEES** regularly posts invited review papers by leading researchers in the relevant fields, which will provide an overview of various subjects from their own perspectives. The editors of **JEES** are aware of the importance of rapid publication for the delivery of new research results to its readers with minimum delay, and fully recognize the need for a short turnaround time. Manuscripts submitted to **JEES** take about 3–5 months from the initial submission to publication. This rapid process applies to all three types of manuscripts that **JEES** publishes: regular papers, letters, and invited papers. The publication of submitted manuscripts is subject to peer review, and the final decision by the Editor-in-Chief is regularly made based on three reviews from experts in the relevant area. This journal actively promotes research in electromagnetic wave-related engineering and sciences, and its ultimate aim is to benefit the global electromagnetic engineering and science community.

Subscription Information

JEES is published quarterly in January, April, July, and October. Full text PDF files are available at the official website (http://www.jees.kr).

The annual subscription rates for this journal are USD 230 for institutional members, USD 55 for regular members, USD 37 for associate members, and USD 28 for student members.

Published by
The Korean Institute of
Electromagnetic Engineering and Science

04376, #706 Totoo Valley, 217 Saechang-ro, Yongsan-gu,
Seoul, Korea
Tel : +82-2-337-9666 / 332-9665
Fax : +82-2-6390-7550
http://www.kiees.or.kr
E-mail : kees@kiees.or.kr

Printed July 25, 2017
Published July 31, 2017

Printed by
Guhmok Publishing Company
Tel : +82-2-2277-3324 / 2277-3364
Fax : +82-2-2277-3390
E-mail : guhmok@guhmok.com

@This paper meets the requirements of KS X ISO 9706, ISO 9706-1994 and ANSI/NISO Z.39.48-1992 (Permanence of Paper).

KOFST
This journal was supported by the Korean Federation of Science and Technology Societies Grant funded by the Korean Government (MEST).

JEES
Journal of
Electromagnetic Engineering
and Science

Jul. 2017
Vol. 17 No. 3

ISSN 2234-8409 (Print)
ISSN 2234-8395 (Online)

INVITED PAPER

REGULAR PAPERS

LETTER

This journal was supported by the Korean Federation of Science and Technology Societies Grant funded by the Korean Government (MEST).

JOURNAL OF ELECTROMAGNETIC ENGINEERING AND SCIENCE, VOL. 17, NO. 3, 113~119, JUL. 2017

http://dx.doi.org/10.5515/JKIEES.2017.17.3.113
ISSN 2234-8395 (Online) · ISSN 2234-8409 (Print)

Application of Compressive Sensing to Two-Dimensional Radar Imaging Using a Frequency-Scanned Microstrip Leaky Wave Antenna

(*Invited Paper*)

Shang-Te Yang · Hao Ling*

Abstract

The application of compressive sensing (CS) to a radar imaging system based on a frequency-scanned microstrip leaky wave antenna is investigated. First, an analytical model of the system matrix is formulated as the basis for the inversion algorithm. Then, L_1-norm minimization is applied to the inverse problem to generate a range-azimuth image of the scene. Because of the antenna length, the near-field effect is considered in the CS formulation to properly image close-in targets. The resolving capability of the combined frequency-scanned antenna and CS processing is examined and compared to results based on the short-time Fourier transform and the pseudo-inverse. Both simulation and measurement data are tested to show the system performance in terms of image resolution.

Key Words: Compressive Sensing, Leaky Wave Antenna, Near Field, Radar Imaging, Resolution.

I. INTRODUCTION

Compressive sensing (CS) is an emerging signal processing technique based on L_1-norm minimization. CS has been applied to two-dimensional (2D) radar imaging to reduce both the number of frequencies and the number of antenna elements (or the number of spatial samples in the case of a synthetic aperture) required for data collection [1–6]. The frequency and element positions are randomized to overcome aliasing in the downrange and grating lobes in the radiation pattern, respectively. In this paper, we explore the use of CS for 2D range-azimuth radar imaging. However, we explore a unique application in which CS is applied to an imaging system based on a frequency-scanned antenna.

A frequency-scanned antenna is a low-cost alternative to a linear phased-array system for obtaining 2D range-azimuth information of targets in a scene. The beam of a frequency-scanned antenna can be steered to different directions by changing the carrier frequency. At the same time, there is still sufficient bandwidth during beam dwell on the target to obtain range information. Consequently, a scene can be imaged with one single frequency sweep. This concept was exploited earlier in [7, 8]. More recently, we have designed, built, and tested a frequency-scanned microstrip leaky wave antenna (MLWA) to track humans [9]. Image formation was performed using the short-time Fourier transform (STFT). Targets are first resolved in range by using a range-gated sliding window. The range-gated response is then Fourier-transformed into the frequency domain, in which target angular information can be obtained. However, the choice of the window function leads to a tradeoff

Manuscript received June 10, 2017 ; Accepted July 11, 2017. (ID No. 20170610-024J)
Department of Electrical and Computer Engineering, The University of Texas at Austin, Austin, TX 78712, USA.
*Corresponding Author: Hao Ling (e-mail: ling@ece.utexas.edu)

in the range and azimuth resolution.

The problem of generating a 2D image from a single frequency response collected using a frequency-scanned antenna can alternatively be approached by considering this problem as a solution to a highly underdetermined system of linear equations. The image domain is a large 2D space, and the measured data is the 1D frequency response. Therefore, the imaging problem is well-suited for CS, that is, how to generate a large but sparse 2D image from a compressed 1D frequency response. Because only a few moving targets are expected within the scene of interest, a solution can be effectively determined by using L_1-norm minimization. Some related preliminary results were reported in [9].

In this paper, we investigate in detail the application of CS to a 2D radar imaging system based on a frequency-scanned antenna. We develop the system matrix based on the antenna characteristics, range delay, and a point-scatterer target model. We then apply L_1-norm minimization to generate the 2D range-azimuth image. The present study is novel in several respects compared to our earlier study in [9]. First, the antenna is a new, narrow-beam antenna that we have designed specifically for operation with a short-pulse radar [10]. It has a length of 90 cm (approximately three times longer than the design reported in [9]), operates between 3 and 6 GHz, and is capable of a beamwidth of the order of 5°. Accordingly, additional near-field considerations are needed to property model the system matrix for applying CS. Second, we closely examine the resolving capability of the combined frequency-scanned radar and CS processing. Both simulation and measurement data are tested to show the system performance in terms of image resolution and to clarify whether the combined system can operate beyond the physical resolution limit.

The remainder of this paper is organized as follows. Section II describes the performance of the long MLWA and discusses the far- and near-field CS formulations. In Section III, we examine the resolution of the combined system based on simulation and measurement. Section IV presents the conclusions of this study.

II. MLWA AND CS FORMULATION

The antenna under consideration is a 90-cm-long, air-filled, half-width MLWA. Fig. 1 shows the built prototype, and the inset shows its cross-sectional dimensions. The antenna is designed to operate from 3 to 6 GHz. Fig. 2 shows the gain pattern of the antenna versus the frequency and angle as simulated using the FEKO electromagnetic simulation software [11]. An infinitely large ground plane is used in the simulation. The gain value is color coded from 0 to 20 dBi. The horizontal axis is the angle θ, which is defined with respect to the longitudinal z-

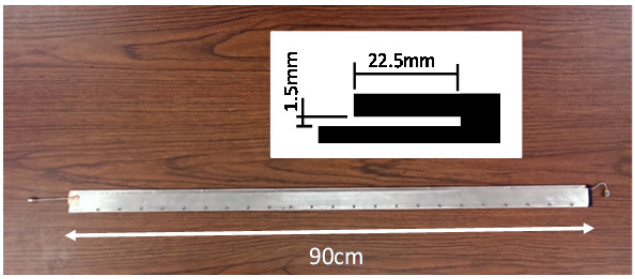

Fig. 1. Photograph of the built 90-cm-long MLWA. The inset shows its cross-sectional dimensions.

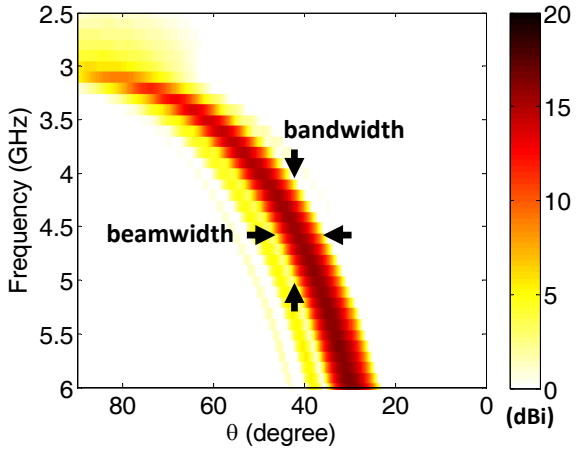

Fig. 2. Simulated gain pattern of the 90-cm-long MLWA as a function of frequency and angle.

direction of the antenna. As the frequency is increased, the antenna beam sweeps from the broadside direction ($\theta = 90°$) toward the endfire direction ($\theta = 0°$), with increasing peak gain. The beamwidth of the antenna is marked by the horizontal arrows in Fig. 2, and it is a function of the beam direction. Similarly, we can define a "target illumination bandwidth" by a vertical cut across the pattern, as shown in the figure. This quantity dictates the achievable range resolution for radar imaging. The tracking of humans using this antenna in combination with a short-pulse radar and STFT processing was reported in [10]. An investigation into further narrowing the beamwidth of the antenna can be found in [12].

To apply CS, we formulate the 2D imaging problem into an underdetermined system of linear equations as follows:

$$\mathbf{y} = \mathbf{A}\mathbf{x} = \sum_{i=1}^{N} \mathbf{a_i} x_i \tag{1}$$

where $\mathbf{x}$ is the large but sparse 2D range-azimuth image, and $\mathbf{y}$ is the measured frequency response. If we neglect the interaction between targets, we can express $\mathbf{y}$ as a superposition of the frequency responses from point targets at different positions. Therefore, x_i, the i-th element of the $\mathbf{x}$ vector, is the strength of a target located at position (R_i, θ_i), and $\mathbf{a_i}$, the i-th column vector of the $\mathbf{A}$ matrix, denotes the corresponding direction-dependent

frequency response of a target with unity strength in the 2D range-azimuth plane. $\mathbf{a}_i$ contains both the antenna response and a free-space propagation factor, and it can be written as follows:

$$\mathbf{a}_i = \left(E^{ff}(f,\theta_i) \cdot \frac{e^{-jk_0 R_i}}{R_i} \right)^2 \tag{2}$$

where $k_0 = 2\pi f/c$. $E^{ff}(f, \theta)$ is the frequency-dependent far-field of the MLWA. The square accounts for the two-way propagation. We next model $E^{ff}(f, \theta)$ as the radiation from an equivalent magnetic line source on the narrow antenna aperture along the z-direction as follows:

$$E^{ff}(f,\theta) = \frac{-jk_0}{2\pi}\sin(\theta)\int_0^L e^{(-\alpha-j\beta)z} \cdot e^{+jk_0\cos(\theta)\cdot z}\, dz \tag{3}$$

where $L = 0.9$ m is the antenna length. α and β are respectively the attenuation and propagation constant of the leaky mode. They can be computed approximately using the transverse resonance method (TRM) [13].

The above CS formulation is based on the far-field radiation pattern of the antenna. However, the far-field distance of the 90-cm-long antenna at 6 GHz is 32.4 m based on the $2L^2/\lambda$ criterion. To properly account for close-in targets, a more exact near-field $\mathbf{a}_i$ can also be formulated as follows:

$$\mathbf{a}_i = \left[\frac{-jk_0}{2\pi}\int_0^L \sin(\theta(z)) \cdot e^{(-\alpha-j\beta)z} \cdot \frac{e^{-jk_0 R(z)}}{R(z)}\, dz \right]^2 \tag{4}$$

where $R(z)$ and $\theta(z)$ are respectively the distance and direction of a near-field target to different parts on the antenna aperture. This equation simplifies to (2) and (3) when the far-field approximation $R(z) = R_i - z\cos(\theta_i)$ is applied. Computing the **A** matrix using the more exact (4) requires carrying out aperture integration repeatedly for every possible target position across the entire 2D range-azimuth plane.

We first test the far-field CS formulation with simulated data from a 3 × 3 grid of point targets. The ground truth is shown in Fig. 3(a). The downrange locations of the targets are 31, 33, and 35 m. The azimuth directions are 37°, 53°, and 67°. Based on the target map, a frequency response **y** is generated using the more exact numerical integration shown in (4). However, the matrix **A** is generated by using the far-field approximation in (2) and (3). The MATLAB package YALL1 [14] is used to solve the L_1-norm minimization with linear constraints, and the resulting image is shown in Fig. 3(b). It is seen that the downrange and azimuth positions of the targets are resolved correctly. The model mismatch between the more exact **y** vector and the far-field **A** matrix is not severe.

Next, the nine targets are moved to 4, 6, and 8 m with the same azimuth positions. The corresponding CS image is shown in Fig. 3(c). It can be observed that the azimuth positions of the close-in targets are not correctly located and that the target response is more diffused. This is due to the model mismatch between the far-field **A** matrix and the target response vector **y**.

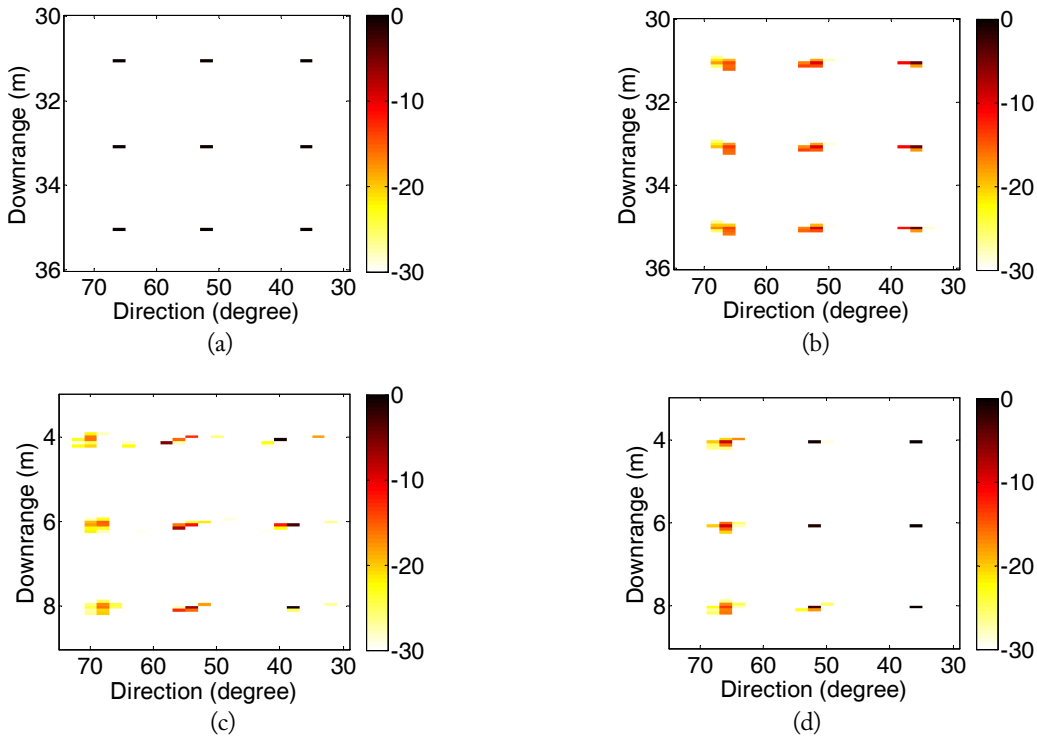

Fig. 3. Testing of far- and near-field formulations. (a) Ground truth map of 3×3 point targets located far away from the antenna. (b) CS image generated using the far-field **A**. (c) CS image of close-in targets generated using the far-field **A**. (d) CS image of close-in targets generated using the near-field **A**.

The same targets are then imaged using the near-field **A** matrix, and the resulting image is shown in Fig. 3(d). In comparison to Fig. 3(c), all the targets are now better focused and the azimuth positions are restored correctly. It is noted that although the targets near the broadside direction are better focused compared to Fig. 3(c), they are still blurrier than the other targets in Fig. 3(d). This could be due to the broader antenna beam near the broadside direction. Lastly, targets are better focused in Fig. 3(d) than in Fig. 3(b), indicating that the minor error introduced by the far-field approximation still degrades the performance of CS. Therefore, it is worthwhile to incorporate as much sensor physics as possible when performing CS imaging. For the remainder of this paper, the near-field **A** matrix computed using (4) is used.

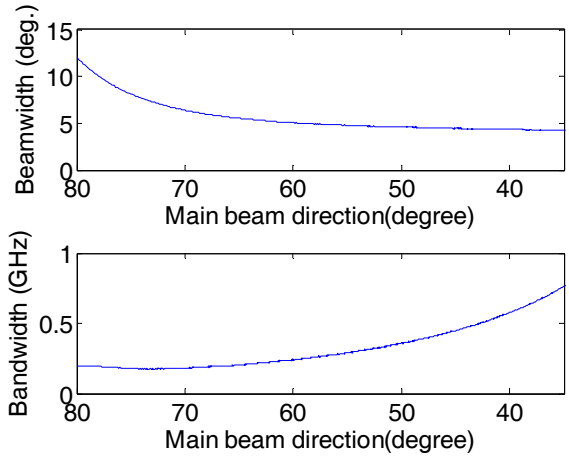

Fig. 4. Two-way 3-dB antenna beamwidth and 3-dB frequency bandwidth of 90-cm-long MLWA. They are plotted as functions of the beam direction.

III. Resolving Capability Study

To examine the resolving capability of the combined CS-MLWA system, closely spaced targets are imaged. For conventional Fourier-based imaging, the azimuth resolving capability is the 3 dB beamwidth of the antenna, and the downrange resolution is inversely proportional to the 3 dB frequency bandwidth. Fig. 4 shows the beamwidth and frequency bandwidth of the 90-cm-long antenna. The same antenna is used for both transmitting and receiving; thus, the 3 dB beamwidth shown in Fig. 4 is based on the square of the gain pattern to account for two-way radiation/reception. It should be noted that the beamwidth and bandwidth are both functions of the beam direction. The beamwidth is approximately 5° for most of the target directions, and the bandwidth ranges from 200 to 750 MHz. Correspondingly, the Fourier resolutions in range, based on the $c/2/bandwidth$ formula, are 75 and 20 cm, respectively. Three groups of three closely spaced targets are placed at approximately $\theta = 40°$, 55°, and 70° to evaluate the direction-dependent resolving capability. Fig. 5(a) shows the ground truth image. The spacing between the targets in azimuth is set to one beamwidth, and the spacing in downrange corresponds to two times

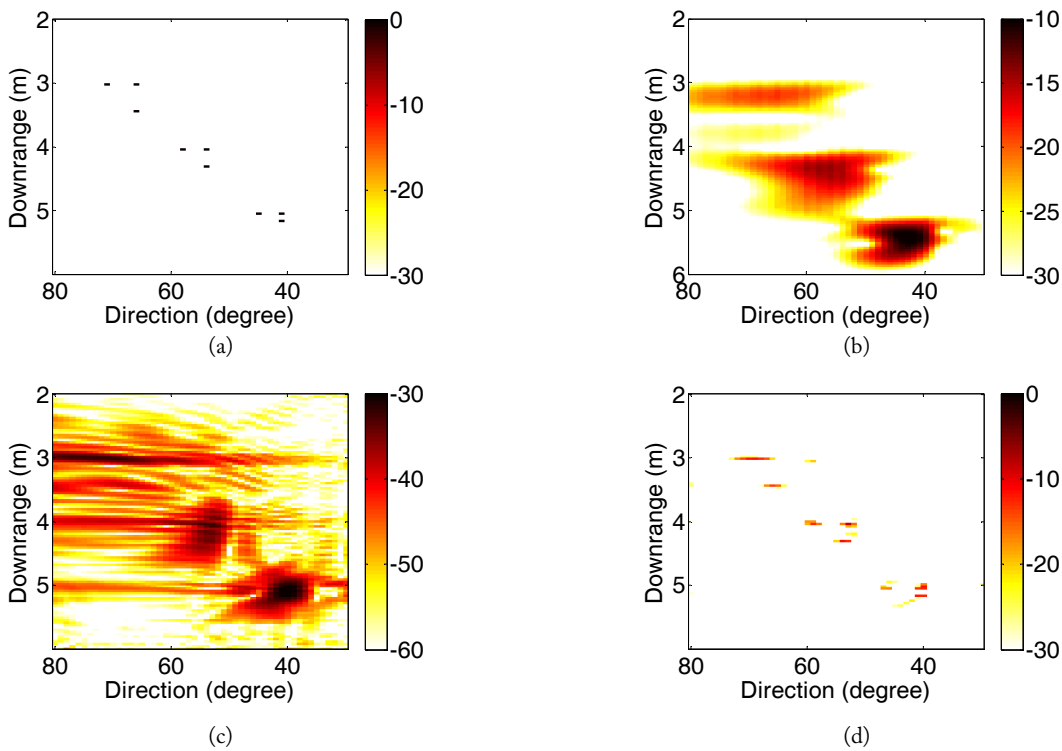

Fig. 5. Testing of target-resolving capability. (a) Ground truth map of three groups of targets spaced by their direction-dependent resolutions. (b) Image generated using STFT. (c) Image generated using a pseudoinverse. (d) Image generated using CS.

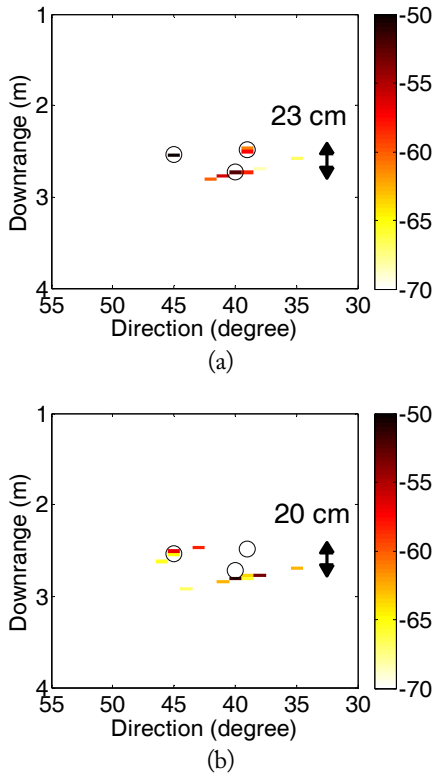

Fig. 6. CS images of three trihedrals measured using the MLWA. (a) Image showing three resolved targets. (b) Image showing only two resolved targets when the farthest trihedral is moved 3 cm closer.

the bandwidth or one-half of the Fourier range resolution. All targets are set to unity strength. As was done in Section III, a frequency response is simulated based on Eq. (4) and a point-scatterer model.

The frequency response is first processed using STFT with a 50-cm sliding Hamming window; the result is plotted in Fig. 5(b). STFT barely resolves targets in downrange, and it cannot resolve targets in the azimuth dimension. It should also be noted that the downrange locations of the targets are not correct, because the direction-dependent group delay of the leaky mode is not modeled by STFT. Next, the pseudoinverse of the near-field **A** matrix is used to generate the image shown in Fig. 5(c). The result is equivalent to solving the underdetermined system of linear equations with L_2-norm minimization. It is observed that targets are better resolved in downrange. Moreover, the targets in the farthest group (at approximately 5 m in downrange) are marginally resolved in azimuth. However, there are substantial artifacts, and it is very difficult to identify the true targets. Lastly, Fig. 5(d) shows the image generated using the near-field **A** matrix and YALL1.

Eight of the nine targets are resolved correctly. Only the target at ($R = 3$ m, $\theta = 66°$) is not shown correctly. Because the targets are placed based on the far-field beamwidth, the two closest-in targets could be spaced too closely to be resolved properly by the near-field beam. Among the three different algorithms, CS achieves the best 2D resolution in the range-azimuth plane. Moreover, it appears that CS can slightly surpass the Fourier resolution in the downrange dimension. More testing revealed that CS could not correctly resolve targets placed closer than one beamwidth, showing that the azimuth resolution is still governed by the physical aperture of the antenna.

Finally, measurement data are collected, and the resolving capability of the system is tested using three trihedrals. A vector network analyzer is used as a radar to collect S_{11} of the antenna in the presence of trihedrals from 2 to 6 GHz. A background subtraction is performed to remove the antenna mismatch and room clutter. During the measurement, the azimuth and downrange spacings between the trihedrals are progressively reduced until just before the trihedrals can no longer be resolved in the corresponding CS image. The result is plotted in Fig. 6(a), where the CS-generated image is shown in color, and the actual target locations are overlaid on the image as open circles. The two targets on the right with roughly the same azimuth position are placed with a 23-cm difference in downrange. The azimuth spacing between the left- and the right-hand-side targets is approximately 5°. These numbers correspond approximately to the beamwidth and frequency bandwidth shown in Fig. 4 at $\theta = 39°$. Next, we move the farthest target 3 cm closer in downrange; the corresponding CS image is shown in Fig. 6(b). It is observed that one target disappears from the image. Moreover, the responses of the remaining two targets become diffused. Testing with measurement data shows that the resolving capability in the azimuth dimension agrees with that found from testing with simulation data. However, we were not able to achieve super-resolution in downrange in the measurement data testing. This could be attributed to several reasons, including mismatch between the TRM-predicted radiation pattern and the built prototype, mismatch between the backscattering from the actual trihedral (18 cm per side) and the point target assumption, and higher-order interactions between targets.

IV. Conclusion

In this paper, the application of CS to 2D radar imaging using a frequency-scanned antenna has been investigated. First, an analytical model of the system matrix was formulated as the basis for the inversion algorithm. Then, L_1-norm minimization was applied to the inverse problem to generate the image of the scene. It was found that because of the antenna length, a near-field formulation is needed to properly image close-in targets. The resolution of the system was then tested rigorously by using closely spaced targets that were placed based on the direction-dependent beamwidth and bandwidth of the frequency-scanned

antenna. It was found that CS achieves the best image resolution in the range-azimuth plane when compared to STFT and a pseudoinverse. Nevertheless, the image resolution achievable using CS is limited by the physical antenna beamwidth in the azimuth dimension and the frequency bandwidth in the downrange dimension. Although the simulations showed some superresolution performance in the downrange dimension, it was not confirmed in the measurement. This could be due to secondary effects not modeled in our formulation, including the actual target response, interactions between targets, and mismatch between the actual antenna prototype and the modeled system matrix. This highlights the importance of accounting for as much of the sensor physics as possible to achieve good performance in terms of image resolution when applying CS.

This work was supported by the Texas Norman Hacerman Advanced Research Program under Grant No. 003658-0065-2009 and the National Science Foundation under Grant No. ECCS-1232152.

REFERENCES

[1] L. C. Potter, E. Ertin, J. T. Parker, and M. Cetin, "Sparsity and compressed sensing in radar imaging," *Proceedings of the IEEE*, vol. 98, no. 6, pp. 1006–1020, 2010.

[2] L. Carin, D. Liu, and B. Guo, "Coherence, compressive sensing, and random sensor arrays," *IEEE Antennas and Propagation Magazine*, vol. 53, no. 4, pp. 28–39, 2011.

[3] L. Zhang, Z. J. Qiao, M. Xing, Y. Li, and Z. Bao, "High-resolution ISAR imaging with sparse stepped-frequency waveforms," *IEEE Transactions on Geoscience and Remote Sensing*, vol. 49, no. 11, pp. 4630–4651, 2011.

[4] E. Lagunas, M. G. Amin, F. Ahmad, and M. Najar, "Joint wall mitigation and compressive sensing for indoor image reconstruction," *IEEE Transactions on Geoscience and Remote Sensing*, vol. 51, no. 2, pp. 891–906, 2013.

[5] L. Poli, G. Oliveri, and A. Massa, "Microwave imaging within the first-order Born approximation of the contrast-field Bayesian compressive sensing," *IEEE Transactions on Antennas and Propagation*, vol. 60, no. 6, pp. 2865–2879, 2012.

[6] N. Whitelonis and H. Ling, "High-resolution radar imaging through a pipe via MUSIC and compressed sensing," *IEEE Transactions on Antennas and Propagation*, vol. 61, no. 6, pp. 3252–3260, 2013.

[7] W. Mayer, M. Wetzel, and W. Menzel, "A novel direct-imaging radar sensor with frequency scanned antenna," in *Proceedings of 2003 IEEE MTT-S International Microwave Symposium Digest*, Philadelphia, PA, 2003, pp. 1941–1944.

[8] Y. Alvarez-Lopez, C. Garcia, C. Vazquez-Antuna, S. Ver-Hoeye, and F. Las Heras Andres, "Frequency scanning based radar system," *Progress in Electromagnetics Research*, vol. 132, pp. 275–206, 2012.

[9] S. T. Yang and H. Ling, "Application of a microstrip leaky wave antenna for range-azimuth tracking of humans," *IEEE Geoscience and Remote Sensing Letters*, vol. 10, no. 6, pp. 1384–1388, 2013.

[10] S. T. Yang and H. Ling, "Combining a frequency-scanned antenna and a short-pulse radar for 2-D imaging," in *Proceedings of 2014 IEEE Antennas and Propagation Society International Symposium (APSURSI)*, Memphis, TN, 2014, pp. 137-138.

[11] EM Software & Systems Inc. FEKO version 6.3. Stellenbosch, South Africa: EM Software & Systems Inc., 2013.

[12] S. T. Yang and H. Ling, "Two-section half-width microstrip leaky wave antenna," *IEEE Transactions on Antennas and Propagation*, vol. 62, no. 10, pp. 4988–4996, 2014.

[13] G. M. Zelinski, G. A. Thiele, M. L. Hastriter, M. J. Havrilla, and A. J. Terzouli, "Half width leaky wave antennas," *IET Microwaves, Antennas & Propagation,* vol. 1, no. 2, pp. 341–348, 2007.

[14] J. Yang and Y. Zhang, "Alternating direction algorithms for l_1 problems in compressive sensing," *SIAM Journal on Scientific Computing*, vol. 33, no. 1, pp. 250–278, 2011.

Shang-Te Yang

received his B.S. degree in Electrical Engineering from National Taiwan University, Taipei City, Taiwan in 2006. He received the M.S. and Ph.D. degrees in Electrical Engineering from the University of Texas at Austin, Austin, TX, USA, in 2011 and 2014, respectively. In August 2014, he joined Apple Inc. in Cupertino, CA. His research interests include frequency-scanned antennas, radar signal processing, low-complexity radar systems, and time-varying radar signatures.

Hao Ling

received his B.S. degrees in Electrical Engineering and Physics from Massachusetts Institute of Technology, Cambridge, MA, USA, in 1982, and his M.S. and Ph.D. degrees in Electrical Engineering from the University of Illinois at Urbana-Champaign, Urbana, IL, USA, in 1983 and 1986, respectively. He joined the faculty of the University of Texas at Austin, Austin, TX, USA, in 1986 and was Professor of Electrical and Computer Engineering and holder of the L. B. Meaders Professorship in Engineering. He retired from the University of Texas in January 2017. Dr. Ling's principal areas of research have been in radar signature prediction and radar feature extraction. He has actively contributed to the development and validation of numerical and asymptotic methods for characterizing the radar signatures from complex targets. In 1986, he and his collaborators pioneered the shooting and bouncing ray (SBR) technique for predicting the radar returns from realistic aerospace vehicles. He was a co-developer of the SBR-based code Xpatch, which has been distributed to over 450 government and industrial organizations in the United States. His recent research interests also include radar signal processing, radar sensing of humans, miniaturized and broadband antenna design, and propagation channel modeling in non-line-of-sight environments. He has published over 200 journal papers and 230 conference papers and coauthored a book on radar imaging (Norwood, MA: Artech House, 2002). Dr. Ling received the NSF Presidential Young Investigator Award in 1987, the NASA Certificate of Appreciation in 1991, and the University of Illinois Distinguished Alumni Award in 2009. From 2015 to 2017, he served as a Program Director in the Electrical, Communications, and Cyber Systems Division at the US National Science Foundation, where he managed a program in communications and sensing. He has been an Associate Editor of the *IEEE Transactions on Antennas and Propagation* since 2013. He is a Fellow of IEEE.

JOURNAL OF ELECTROMAGNETIC ENGINEERING AND SCIENCE, VOL. 17, NO. 3, 120~125, JUL. 2017

http://dx.doi.org/10.5515/JKIEES.2017.17.3.120
ISSN 2234-8395 (Online) · ISSN 2234-8409 (Print)

Monopulse Tracking Performance of a Satcom Antenna on a Moving Platform

Gyuhan Cho* · Gwang Tae Kim

Abstract

A satellite communication (Satcom) antenna mounted on a moving platform provides a controlled heading that enables a geosynchronous satellite to communicate with the ground. A monopulse tracking method is effective for antenna control on a vehicle when it vibrates severely. However, this method has unexpected obstacles and its control performance is insufficient. To improve its control performance, the control command and monopulse error, the signal delay, and the radome effect are evaluated through tests. The authors then propose a method to transform the antenna error from 3D coordinates to 2D antenna coordinates. As a result, the antenna control performance is improved. As indicated in this study, examining antenna systems using the monopulse method on moving platforms is possible by understanding the antenna test process.

Key Words: Geosynchronous Satellites, Inertially Stabilized Platform, Monopulse Signal, Moving Platform, Radome, Satcom Antenna.

I. INTRODUCTION

The satellite communication (Satcom) antenna technology is applied to various systems to communicate with other systems that are distant. A message sent from a Satcom antenna goes through a geosynchronous satellite and is delivered to other antennas [1].

As geosynchronous satellites, which are used for this communication system, remain in the same location at geocentric earth-centered earth-fixed (ECEF) Cartesian coordinates, they appear to remain at one point in the sky. This kind of satellite moves around the Earth in an orbit that is farther away than those of other types of satellites. These two features make it easy for the Satcom antenna to connect with the satellite. As the antenna heads in one direction in the ECEF Cartesian coordinates, this antenna will communicate with the satellite regardless of time and space if the antenna does not move far away from its initial location. This characteristic enables the Satcom antenna technology to be simply applied to various types of moving vehicles, including those used in military applications [2].

To use the Satcom antenna technology on a moving platform, the inertially stabilized platform (ISP) techno-logy is usually applied to hold or control the line of sight (LOS) of the antenna relative to the satellite direction (Fig. 1). Several methods can be used to control the antenna. For an antenna on a stationary body, the step-tracking method is effective at finding the satellite direction by scanning the beacon level in the air and choosing the direction where the highest beacon level is scanned [3, 4].

The monopulse tracking method is preferred for controlling an antenna on a moving body. Monopulse measures the radiation direction in real time using a beam that is spread out across the centerline of the antenna. Therefore, the monopulse track-

Manuscript received January 17, 2017 ; Revised April 21, 2017 ; Accepted May 24, 2017. (ID No. 20170117-005J)
Agency for Defense Development, Daejeon, Korea.
*Corresponding Author: Gyuhan Cho (e-mail: gyuhan.cho@gmail.com)

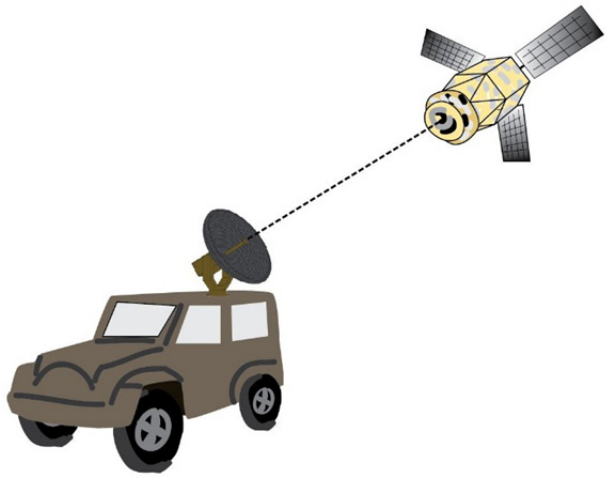

Fig. 1. Concept of the Satcom antenna control on a moving platform (This antenna uses ISP to hold the LOS stationary).

ing method is more effective on a moving body than the step tracking method, which requires sufficient time to scan the beacon level [5].

In this study, we seek to enhance the control performance of a Satcom antenna on a moving platform, such as a car, ship, or airplane. Wave motion can be imparted to these moving platforms or vibrated by external forces. As this research focuses on defense development for military purposes, most angles are normalized by multiplying them by an arbitrary number *K*, and several specific algorithms are not included.

II. Test Conditions

1. Antenna

The antenna pedestal structure used in this research consists of a two-axis gimbaled pedestal, with an azimuth axis and an elevation axis. Each axis is moved by a motor and a resolver [6]. The third motor is located behind the antenna aperture and rotates the feed antenna to adjust the angle to the monopulse signal, which exhibits linear polarization. As this axis is not used to control the LOS to the satellite, it is not considered in this research. A number of radio frequency-related components, such as a low noise amplifier, are placed at the back side of the antenna. As this moving platform has to change its direction freely, a slip-ring is used on the azimuth axis to rotate the axis beyond one revolution. The parabolic reflector is made from carbon composites, and the pedestals are fabricated from stainless steel.

In this research, two coordinates are set. The first one is the ground coordinate that is fixed on the ground under the antenna. It does not change even if the moving platform vibrates or if the antenna moves. Therefore, the LOS of the antenna on the ground coordinate is stationary because geosynchronous satellites remain unchangeable in terms of ECEF Cartesian coordinates. The second one is the antenna coordinate, which considered the center bottom of the antenna as the standard datum. The heading direction of the antenna can be represented on this coordinate using the azimuth and elevation gimbal angles.

In the ISP technology, a gimbal lock can occur when the LOS and the azimuth axis are driven into a parallel configuration. The gimbal lock effect means that the pedestals lose one degree of freedom of control. Fortunately, the moving platform on which this antenna is attached is expected to perform only in a designated area, and the gimbal lock effect is not considered.

2. Test Method

This research aims to stabilize the LOS of this antenna in a vibrating environment that imitates the platform's movement. A number of instruments are applied in this test.

A motion simulator is utilized to cause platform vibration. Fig. 2 illustrates the concept of this test. The antenna is fixed to a simulator, which generates a disturbance on the moving platform. This motion simulator can impart six axes of motion: roll, pitch, yaw, surge, sway, and heave. The test disturbance is calculated according to the test flight kinematic information. As the purpose of this test is to stabilize the LOS of the antenna, this antenna is tested only for the rotational axis.

The inertial navigation system (INS) is a sensor that can measure the motion and rotation of a moving object without external references using a combination of three gyro sensors and three accelerator sensors. For most moving platform systems, the platform's position information is delivered from the platform's main INS system to the control unit of the antenna. However, for this antenna test, another INS is mounted to measure disturbances of the motion simulator.

As the monopulse method is used to detect the satellite direction using specific signals sent by satellites, selecting the correct satellite with which to make the data link is important. For this test, a Korean geosynchronous satellite, which is a Ku-band

Fig. 2. Antenna on a six-axis motion simulator.

satellite that uses linear polarization, is applied.

This test is conducted inside a radome to protect the antenna from disturbances, such as wind, rain, and dust.

3. Performance

The antenna tracking test is conducted with the following prescribed conditions. The disturbance is a sine wave movement (17° 0.4 Hz) for the roll axis of the simulator. This wave is calculated using the real flight of an airplane, and the most severe expected external force is applied. Using the INS sensor and the monopulse signal, the control target angles of the azimuth and elevation motors are calculated on the basis of the antenna's position status.

Fig. 3 and Table 1 show the results of the monopulse tracking test. The black line is the control error, which indicates how well the antenna follows the target angle; the gray bold line indicates the monopulse error. For security purposes, the angles are multiplied by an arbitrary number *K*. The root mean square (RMS) and the peak angle of the error are provided in Table 1. The RMS of the monopulse error is 10 times higher than that of the control error. Therefore, the motors of the antenna pedestal follow the commanded angles well, but the LOS of the antenna does not head precisely for the satellite.

Section III describes the process to check for possible causes of instances in which the antenna cannot track the satellite accurately. Whether the command angles correspond with the direction of the satellite is not certain. The delay of the signal processing is then checked. The radome effect is also tested.

Table 1. Monopulse tracking test results (sine wave 17° 0.4 Hz)

	RMS (°)	Peak (°)
Control error	0.0786	0.2600
Monopulse error	0.7919	1.5559

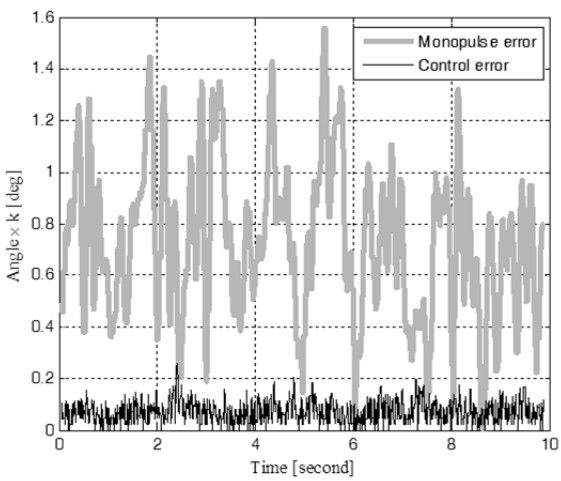

Fig. 3. Results of the monopulse tracking test: monopulse error and control error (sine wave disturbance 17° 0.4 Hz).

III. Cause Analysis

1. Command Angle and Monopulse Signal

To improve the control performance, a number of tests are conducted to confirm the critical factors affecting the control. The command angle is first tested. To check the command angle, the command angle and the monopulse angle are translated into direction angles on the ground coordinate. The monopulse angle is the sum of the motor angle feedback from the resolver and the monopulse error; this value is a direction heading for the satellite on the antenna coordinate measured by the monopulse system. By comparing the two angles on the ground coordinate, confirming which angle is wrong is possible. Given these two angles, the right angle must be unchangeable and the other is a variable that is considered a disturbance as the satellite is stationary.

In this comparison, the command angle and the monopulse angle are translated from the antenna coordinate to the ground coordinate. Using a trigonometric function, the vector for the LOS of the antenna on the antenna coordinate is written in terms of the azimuth and the elevation motor angles $\boldsymbol{\theta_{AZ}}$ and $\boldsymbol{\theta_{EL}}$, which are obtained from the monopulse tracking test.

$$\begin{bmatrix} \boldsymbol{x_l} \\ \boldsymbol{y_l} \\ \boldsymbol{z_l} \end{bmatrix} = \begin{bmatrix} \boldsymbol{\cos\theta_{EL}\cos\theta_{AZ}} \\ \boldsymbol{\cos\theta_{EL}\sin\theta_{AZ}} \\ \boldsymbol{\sin\theta_{EL}} \end{bmatrix}, \tag{1}$$

where the subscript l indicates that this vector is represented on the antenna coordinate. The subscript g indicates the global coordinate.

Using the inverse rotation matrix, which is a Euler matrix, about the X, Y, and Z axes, the vector in the ground coordinate can be calculated from the vector in the antenna coordinate as follows:

$$\begin{bmatrix} \boldsymbol{x_g} \\ \boldsymbol{y_g} \\ \boldsymbol{z_g} \end{bmatrix} = \boldsymbol{E_Z(\psi_1)^{-1}E_Y(\theta_1)^{-1}E_X(\varphi_1)^{-1}}, \tag{2}$$

where the position angles on the stationary simulator ψ_1, θ_1, φ_1 are applied to the Euler matrix.

$$\begin{bmatrix} \boldsymbol{\theta_{AZ}^{ground}} \\ \boldsymbol{\theta_{EL}^{ground}} \end{bmatrix} = \begin{bmatrix} \boldsymbol{\tan^{-1}(x_g/y_g)} \\ \boldsymbol{\tan^{-1}\left(z_g/\sqrt{x_g{}^2+y_g{}^2}\right)} \end{bmatrix}. \tag{3}$$

From the vector on the ground coordinate, the motor angles of the antenna on the ground coordinate can be calculated using the reverse of (1).

$$\begin{bmatrix} \boldsymbol{\theta_{AZ\_error}^{ground}} \\ \boldsymbol{\theta_{EL\_error}^{ground}} \end{bmatrix} = \begin{bmatrix} \boldsymbol{\theta_{AZ}^{ground}} \\ \boldsymbol{\theta_{EL}^{ground}} \end{bmatrix} - \begin{bmatrix} \boldsymbol{\theta_{AZ}^{satellite}} \\ \boldsymbol{\theta_{EL}^{satellite}} \end{bmatrix}. \tag{4}$$

The precise ground angle cannot be revealed in this study be-

cause this antenna is developed for military purposes. The error against the theoretical satellite direction is plotted. The results are separated into the azimuth angle and the elevation angle, and the two graphs are synchronized based on time [7].

Fig. 4 shows how the monopulse angle and the command angle differ according to the actual direction. Although the gaps can change because of the disturbance from the simulator, the difference between the two angles is remarkable at the elevation angle. At the elevation angle, the variance of the monopulse error is two times more severe than that of the command angle. This graph indicates that the heading point of the input command angle is not the point where the satellite exists. The antenna cannot determine the heading of the satellite even if the motors follow the command angles. However, whether this is due to the command angle being miscalculated or not is not certain.

2. Monopulse Signal Delay

The previous test confirmed a gap between the satellite direction and the command angle. However, what degrades the antenna control performance remains unclear. To check for possible factors that can affect the control performance, a number of additional tests are conducted.

The phase difference between the command angle and the monopulse angle is about 0.4 second, as illustrated in Fig. 4. Therefore, the monopulse signal delay is considered to be an important factor affecting the antenna control. To determine the signal delay, the monopulse tracking test is conducted with a changed value of disturbance (sine wave 17° 0.01 Hz). The speed of the disturbance is only changed in comparison with the value in the previous test. Using a slowdown of the simulator movement, the effect of the signal delay can be minimized.

Fig. 5 shows the results of the monopulse tracking test on the

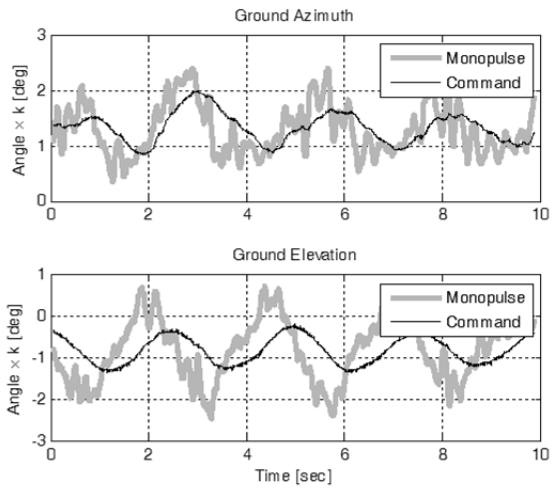

Fig. 4. Monopulse tracking test results for the ground coordinate (sine wave 17° 0.4 Hz).

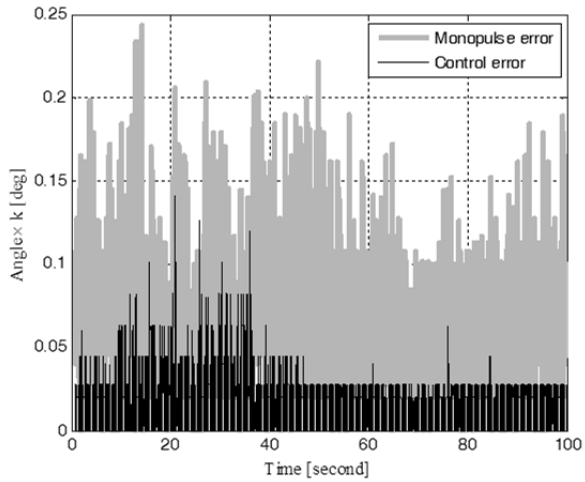

Fig. 5. Monopulse tracking test results: monopulse error and control error (sine wave disturbance 17° 0.01 Hz).

Table 2. Monopulse tracking test results (sine wave 17° 0.01 Hz)

	RMS (°)	Peak (°)
Control error	0.0197	0.1414
Monopulse error	0.0828	0.2433

17° 0.01 Hz sine wave disturbance. The RMS and the peak of the error are provided in Table 2. In comparison with the previous test, a control error that has four times better RMS and two times better peak error is found. In addition, a nine times better RMS error and a six times better peak error are found for the monopulse error. Greater improvement is achieved for the monopulse error than for the control error.

These results imply that the time delay of the monopulse signal processing can be regarded as one of the important aspects that degrade the antenna control performance.

To obtain an accurate analysis, the angles are translated to ground coordinates in the same way as in the previous test. Fig. 6 shows the results of the angle translation. As shown in this graph, the command angle and the monopulse angle are headed toward the same direction as in the previous test. That is, the command angle is accurately headed for the satellite direction. However, even though the monopulse error decreases, the heading direction of the antenna changes with the movement of the motion simulator.

3. Radome

According to the previous test results, the LOS of the antenna is not constant with the movement of the simulator. As the satellite is located far from the Earth, the LOS of the antenna must be constant regardless of the position of the antenna. For this reason, the radome is unlikely to be the source of the variable LOS of the antenna.

A radome is used to protect the antenna from external im-

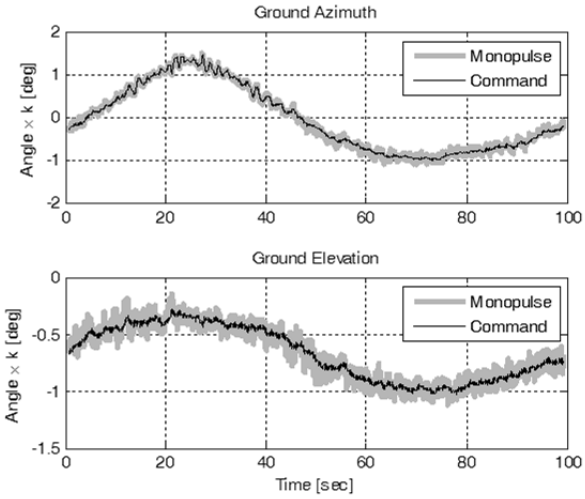

Fig. 6. Results of the stabilization test for disturbance (sine wave 17° 0.01 Hz).

pacts that can affect the antenna control, make the heading direction inaccurate, and lower the antenna communication ability. However, a radome can attenuate, depolarize, and distort the antenna wave, which can all degrade the antenna pattern. Fig. 7 shows the LOS distortion problems that can result from using a radome. The Satcom antenna's LOS follows the dotted line, but the signal LOS changes to a solid line after going through the antenna radome [8]. The Satcom antenna is usually located on the topside of the moving platform and is covered by the radome. The body of the moving platform is designed to consider the aerodynamics and weight balance of the vehicle. For this reason, the shape of the radome is not simple and modeling the radome is complicated when attempting to compensate for the bending of the antenna signal.

Although the use of a radome brings these problems, the antenna nonetheless must be protected by the radome on the platform. Distortion of the antenna signal occurs regardless of how precisely the radome is designed. Another solution is to try to improve the performance of the antenna control. Although distortion exists, the control error is sufficiently low that the antenna's control performance can be improved by decreasing the monopulse signal delay.

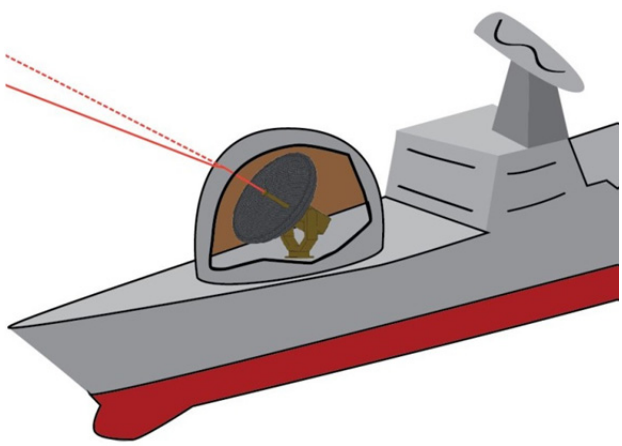

Fig. 7. Effect of radome on the LOS of antenna.

Table 3. Monopulse tracking test results (sine wave 17° 0.4 Hz with the changed monopulse signal filter)

	RMS (°)	Peak (°)
Control error	0.0389	0.1826
Monopulse error	0.1486	0.2236

Monopulse signals are used to detect the direction of a satellite. When using such signals, a filter is essential because monopulse signals are noisy and unclear. To clarify the monopulse signal, a finite impulse response (FIR) filter is applied for system robustness, which is the most important factor in defense applications. The FIR filter incurs no feedback from output to input and is stable because all the poles lie in the origin. However, this filter requires more taps than the infinite impulse response (IIR) filter. This requirement increases the filter processing time and causes the monopulse signal to have a long delay [9].

To decrease this delay, the filter is changed from an FIR to an IIR. The IIR filter incurs feedback from output to input but requires fewer taps to obtain the step-up and step-down responses. Therefore, the sensing delay can be decreased by changing the filter. The robustness of the filter is compensated for by the software setup. The specific filter algorithm is not revealed in this study for security reasons of defense development.

IV. Improved Performance

Fig. 8 presents the results of the monopulse tracking test for a 17° 0.4 Hz sine wave disturbance with the changed monopulse

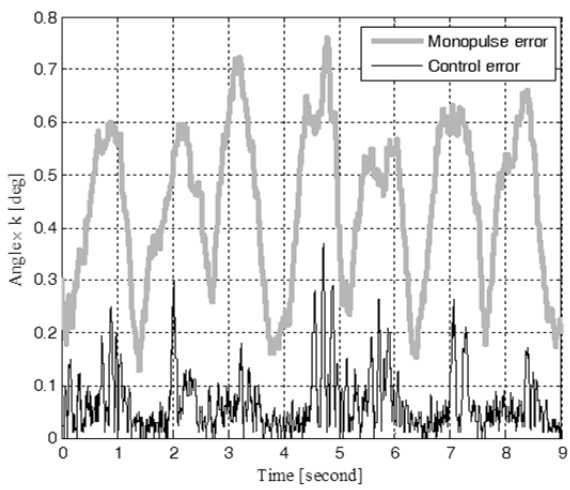

Fig. 8. Monopulse tracking test results of the monopulse error and control error (sine wave disturbance 17° 0.4 Hz and changed monopulse signal filter).

signal filter. The RMS and peak error are shown in Table 3. The control error is similar to that in the test using the previous filter. However, the monopulse error is 2.5 times smaller than the RMS and a 3.5 times lower peak error is found. These results confirm that the antenna using the new monopulse signal processing filter can track the satellite more accurately than the antenna with the previous filter.

V. CONCLUSION

A Satcom antenna on a moving platform points to a geosynchronous satellite and communicates through it. Moving platforms are subject to vibration by external disturbances when they move. According to the disturbance data of the platform, an antenna control test is conducted for the disturbances. A way to change the antenna heading error from ground coordinates to antenna coordinates is suggested through the test. Accordingly, delay is decreased and the performance of the antenna control is enhanced by changing the monopulse signal processing. The antenna shows 2.5 times better control performance than before. Overall, this study provides a better understanding of monopulse antenna systems on the move.

REFERENCES

[1] J. Ryu, D. Oh, H. Kim, and S. Hong, "Proposal of an algorithm for an efficient forward link adaptive coding and modulation system for satellite communication," *Journal of Electromagnetic Engineering and Science*, vol. 16, no. 2, pp. 80–86, 2016.

[2] J. M. Hilkert, "Inertially stabilized platform technology, concepts and principles," *IEEE Control Systems*, vol. 28, no. 1, pp. 26–46, 2008.

[3] M. K. Masten, "Inertially stabilized platforms for optical imaging systems," *IEEE Control Systems*, vol. 28, no. 1, pp. 47–64, 2008.

[4] H. G. Wang and T. C. Williams, "Strategic inertial navigation systems-high-accuracy inertially stabilized platforms for hostile environments," *IEEE Control Systems*, vol. 28, no. 1, pp. 65–85, 2008.

[5] S. M. Sherman and D. K. Barton, *Monopulse Principles and Techniques*, 2nd ed. Boston, MA: Artech House, 2011.

[6] J. Debruin, "Control systems for mobile satcom antennas," *IEEE Control Systems*, vol. 28, no. 1, pp. 86–101, 2008.

[7] D. J. Kozakoff, *Analysis of Radome-Enclosed Antennas*, 2nd ed. Boston, MA: Artech House, 2010.

[8] G. Burks, E. Graf, and M. Fahey, "A high frequency analysis of radome-induced pointing error," *IEEE Transactions on Antennas Propagation*, vol. 30, no. 5, pp. 947–955, 1982.

[9] L. Litwin, "FIR and IIR digital filters," *IEEE Potentials*, vol. 19, no. 4, pp. 28–31, 2000.

Gyuhan Cho

obtained his B.S. degree in control and system engineering from the Tokyo Institute of Technology, Japan, and his M.S. in mechanical engineering from Seoul University, Korea. He has worked for the Agency for Defense Development since 2014. His research interest is robotics dynamic design and control.

Gwang Tae Kim

received B.S. degree in electrical engineering from Inha University, Incheon, Korea, in 2012, and M.S. degree in electrical engineering from KAIST, Daejeon, Korea, in 2014. He has worked as a researcher at the Agency for Defense Development, Korea, since 2014. His research interests include nonlinear control, tracking algorithm, and control applications.

JOURNAL OF ELECTROMAGNETIC ENGINEERING AND SCIENCE, VOL. 17, NO. 3, 126~132, JUL. 2017

http://dx.doi.org/10.5515/JKIEES.2017.17.3.126
ISSN 2234-8395 (Online) · ISSN 2234-8409 (Print)

Magnetic Resonant Wireless Power Transfer with L-Shape Arranged Resonators for Laptop Computer

Jung Han Choi[1] · Seok Hyon Kang[2] · Chang Won Jung[2,*]

Abstract

In this study, we designed, measured, and analyzed a rearranged L-shape magnetic resonance coupling wireless power transfer (MR-WPT) system for practical applications with laptops. The typical four resonator MR-WPT (Tx part: source loop and Tx coil; Rx part: Rx coil and load loop) is difficult to apply to small-sized stationary and mobile applications, such as laptop computers, tablet-PCs, and smartphones, owing to the large volume of the Rx part and the spatial restrictions of the Tx and Rx coils. Therefore, an L-shape structure, which is the orthogonal arrangement of the Tx and Rx parts, is proposed for indoor environment applications, such as at an L-shaped wall or desk. The relatively large Tx part and Rx coil can be installed in the wall and the desk, respectively, while the load loop is embedded in the small stationary or mobile devices. The transfer efficiency (TE) of the proposed system was measured according to the transfer distance (TD) and the misaligned locations of the load loop. In addition, we measured the TE in the active/non-active state and monitor-open/closed state of the laptop computer. The overall highest TE of the L-shape MR-WPT was 61.43% at 45 cm TD, and the TE decreased to 27.9% in the active and monitor-open state of the laptop computer. The conductive ground plane has a much higher impact on the performance when compared to the impact of the active/non-active states. We verified the characteristics and practical benefits of the proposed L-shape MR-WPT compared to the typical MR-WPT for applications to L-shaped corners.

Key Words: L-Shape, Laptop Applications, Magnetic Resonance, Transfer Efficiency, Wireless Power Transfer.

I. Introduction

Conventional indirect-fed magnetic resonant coupling wireless power transfer (MR-WPT) systems consist of four resonators in the following order: source loop, transmitter (Tx) coil, receiver (Rx) coil, and load loop [1]. Spiral-shaped coils (Tx and Rx) are located between the source and load loops for strong magnetic coupling. In indirect-fed MR-WPT systems, the Tx part consists of the source loop and the Tx coil, while the Rx part consists of the load loop and the Rx coil. Most user experiences indicate that in practical applications, it is difficult to use strongly-coupled magnetic resonance wireless charging system [2, 3]. This is mainly because of the large volume of the Rx part and the spatial restrictions of the Tx and Rx coils. There is a limitation to the thickness of mobile devices, and hence, the distance between the load loop and Rx coil must be optimized for to the highest transfer efficiency. Further, if only the load loop is inserted in mobile devices, it would be inconvenient to carry the Rx coil and place it near the mobile device. This would need additional considerations, such as alignment of the Tx and Rx parts, the practical transfer distance (TD), the transfer efficiency (TE), and limited charging places.

Manuscript received February 14, 2017 ; Revised May 24, 2017 ; Accepted June 23, 2017. (ID No. 20170214-008J)
[1]Fraunhofer Heinrich-Hertz Institute, Berlin, Germany
[2]Graduate School of Nano·IT·Design Fusion, Seoul National University of Science and Technology, Seoul, Korea.
[*]Corresponding Author: Chang Won Jung (e-mail: changwoj@seoultech.ac.kr)

In this work, we explore an L-shaped MR-WPT system for applications in "L" shaped corners, such as at a wall or a desk in an indoor environment. The Tx and Rx parts are orthogonal to each other, and hence the term "L-shape".

The concept of the proposed structure is "easy application in many places". Fig. 1(a) shows the L-shape MR-WPT. The typical MR-WPT consists of four resonators. The order of arrangement of the resonators in MR-WPT does not experimentally affect the TE [4, 5]. Therefore, the order of the arrangement of the load loop could be varied without TE changes in typical MR-WPT systems for practical applications. However, the rearranged Out-In MR-WPT shown in Fig. 1(b) has a spatial limitation for the Tx and Rx coils [5]. Electronic devices including a load loop must be placed between the Tx and Rx coils. Therefore, the system shown in Fig. 1(c) is proposed to this solve problem of the spatial limitation and to apply this system to L-shaped corners of the wall or at desks in an indoor environment. The proposed structure is basically modified from the Out-In MR-WPT as follows [5]: source loop - Tx coil - Load loop - Rx coil. In real applications, the large sized Tx part (Tx coil and source loop) and the Rx coil of the Rx part can be located in the wall and the desk, respectively, while the load loop of the Rx part is embedded in the stationary or mobile devices.

In measurement of the TE, three kinds of load loops according to the shape (circle and rectangle) and thickness (0.5 cm for wire and 1.0 cm for pipe) of the load loop for the performance comparison in practical laptop applications are tested. The TE is measured according to the TD, and it is also measured according to the misaligned location of the load loop on the Rx coil. In addition, for comparison of the practical performance according to the states of a laptop computer, we measured the TE in the active/non-active states and monitor-opened/closed states of the laptop computer. It is noted that the active/non active states of the laptop computer mean power on/off.

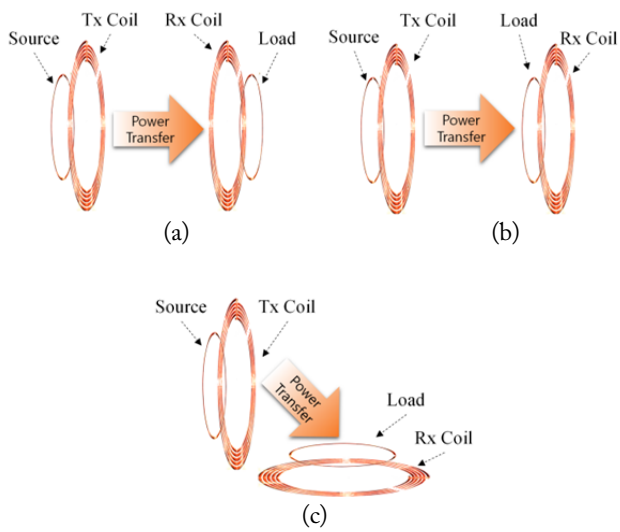

Fig. 1. Concept of the L-shape MR-WPT. (a) Typical MR-WPT, (b) Out-In MR-WPT, and (c) L-shape MR-WPT.

Section II describes the design and the fabrication of the proposed system. Thorough experiments and in-depth analysis are conducted, for comparing TEs in various use cases as described in Section III. The conclusion of this work is made in Section IV.

II. Design and Configuration of the L-Shape MR-WPT

The proposed L-shape MR-WPT is modified from the Out-In MR-WPT [5]. Cross-coupling value between Tx coil and load loop was neglected for simplicity because the value is low [6]. Fig. 2 shows the structure and configuration of the proposed system. Distance A is TD, which is defined as the distance from centers of the Tx and Rx coils. Distance B is the height of the load loop from the Rx coil. Distance A is adjusted by two parameters. One is the height of the Tx part from the Rx coil, i.e., distance C, while the other is the distance between the Tx part and the Rx coil, i.e., distance D.

The source loop is excited by input power of 0 dBm. A magnetic field is generated around the source loop. Then, there is mutual inductance between the source loop and the Tx coil. Similarly, there is mutual inductance between the Tx and Rx coil as well. Finally, the power is transferred to the load loop by the mutual inductance between the Rx coil and the load loop.

The Rx coil and the load loop in the Rx part are vertical to the Tx part and parallel to the floor in the L-shape MR-WPT. The resonators, loops, and coils are fabricated using 1.0-cm-thick copper pipe. The source loop is a circular structure with a 40 cm diameter. The Tx and Rx coils are designed with the same-sized spiral coils. The outer circle is 60 cm, and the pipe is wound for 5 turns with a 1.5-cm pitch. A 6-pF capacitor is connected at the ends of coils to resonate at the operating frequency.

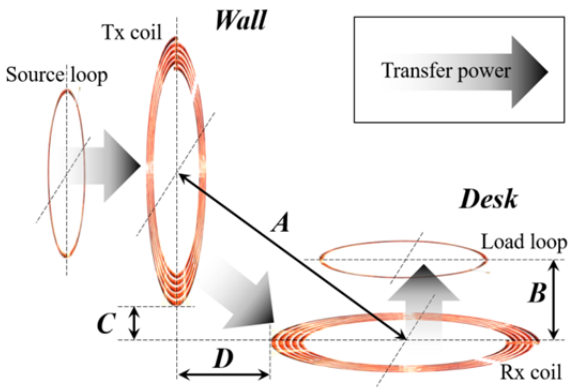

Fig. 2. Structure of L-shape MR-WPT.

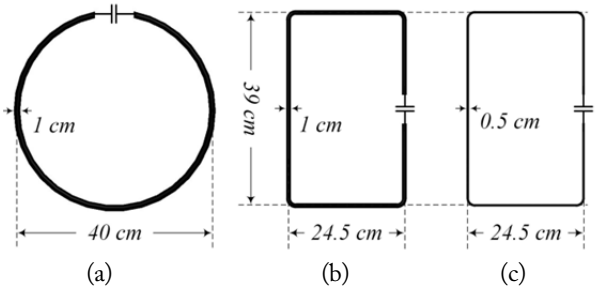

Fig. 3. Load loops of Rx part. (a) Circular loop (CL), (b) rectangular pipe loop (RPL), and (c) rectangular wire loop (RWL).

As shown in Fig. 3, there are three load loops with dimension combinations of two thicknesses and two shapes in the L-shape MR-WPT. One load loop, which is the control group, is a circular loop (CL) made with 1.0-cm-thick pipe. The CL is designed as a full-size replica of the source loop. The Tx and Rx parts in MR-WPT with the CL are symmetrical configurations. The other two load loops are fabricated from 1.0-cm-thick copper pipe and 0.5-cm-thick copper wire, and are designed using the same sized rectangular loops as those of a laptop computer, i.e., 24.5 cm × 39 cm. These load loops are referred to as rectangular pipe loop (RPL) and rectangular wire loop (RWL). The total length of the rectangular and circular loops is about 127 cm. With these two different shapes, we can determine the effect of the shape of the resonator on the magnetic coupling with the nearest one. Table 1 shows the simulated *RLC* values for each resonator. The equivalent circuit for the L-shape is usually expressed using *RLC* values. The equivalent circuit of L-shape MR-WPT is similar to that of Out-In MR-WPT [4, 5]. All loops and coils were connected with capacitors, resulting in the wanted resonance frequency of 6.96 MHz. The capacitance values in Table 2 were calculated to have the same resonance frequency after extracting the inductances of the coils using a three-dimensional full-wave electromagnetic wave simulator.

Table 1. Simulated RLC values and Q-factor of coils and loops used in L-shape MR-WPT

Resonator	R (Ω)	L (nH)	C (pF)	Q-factor
Source loop, CL	0.07	955.33	576.8	89.59
RPL	0.05	804.79	684.7	112.04
RWL	0.08	955.00	577.0	86.33
Tx coil, Rx coil	0.33	55,103.71	10.0	1,134.19

Table 2. Capacitance values of coils and loops used in L-shape MR-WPT

Resonator	Simulated value (pF)	Experimental value (pF)
Source loop, CL	576.8	560.0
RPL	684.7	680.0
RWL	577.0	560.0
Tx coil, Rx coil	10.0	6.0

III. Results of Measurements and Simulation

1. Measurement and Simulation of the L-shape MR-WPT

In the measurements, we compared the TE of the L-shape MR-WPT with that of the Out-In MR-WPT at the same TD, i.e., distance A [5]. The effects of the thickness and shape of the load loop on the TE of the MR-WPT are investigated. The trends of the TE of the L-shape MR-WPT with three load loops with respect to the TD are analyzed using the simulation and measurement results. We also investigated the trends of the TE of the L-shape MR-WPT when the load loop is misaligned from the center position at the optimized height. In addition, we verified the TE change in the monitor opened/closed states and active/non-active states of a laptop computer.

In these experiments, the source loop, Tx coil, and Rx coil described in Section II were fixed resonators in the fabricated MR-WPT. There are two variables in the measurement of transmission of the scattering parameter (S_{21}) in Fig. 1(b). One is TD, i.e., distance *A*. The measurement was conducted at TD values of 45 cm, 55 cm, 65 cm, and 75 cm. To set up the four TDs mentioned above, we keep distance *C* constant when distance *D* is variable. The other variable is distance *B*.

The measurement was conducted at distance *B* values of 0 cm, 10 cm, and 20 cm. When the distance *A* is varied, the distance *D* is arbitrarily chosen. The distance between the source loop and the Tx coil was moved to match the impedance for the highest TE. The TE is calculated from the Eq. (1) using S_{21} measured by a vector network analyzer (VNA; Agilent E5071B). The equation for the relationship between TE (η) and S_{21} is given in Eq. (1) for the TE of the MR-WPT [6, 7].

$$\eta = \frac{P_{output}}{P_{input}} = \frac{V_{load}^{\ 2} / (R_{load} + R_{output})}{V_{source}^{\ 2} / \{4(R_{source} + R_{input})\}} = |S_{21}|^2 \qquad (1)$$

The TE were calculated using the resistance (R) of the resonator, input impedance ($R_{input} = R_{output} = 50\ \Omega$), and input voltage ($V_{source}$). By measuring the S_{21} using the VNA, one can calculate the TE for the MR-WPT.

As shown in Table 3, the highest TE of the system with the CL was 64.48% at distance A of 45 cm and distance B of 0 cm. In the case of the system with the RPL, the highest TE was 61.43%, as shown in Table 3. There was about a 3.05% difference between the system with the CL and the RPL in terms of the TE. In the case of the RWL, the TE was 61.39%, as shown in Table 3. The two TEs between the system with the RWL and the RPL were almost the same. The average resonant frequency was about 6.96 ± 0.002 MHz. The trend of TE at dis-

Table 3. Measurement results of TE of L-shape MR-WPT according to load loops (distance $C = 0$ cm)

MR-WPT (Load loop)	Distance B	Transfer distance (cm) 45 (%)	55 (%)	65 (%)	75 (%)
Typical MR-WPT	-	78.71	73.50	65.45	53.32
L-shape MR-WPT					
CL	0	64.48	49.21	30.47	14.80
	10	49.94	40.85	29.58	14.82
	20	26.24	19.48	13.50	6.71
RPL	0	61.43	49.10	32.86	16.04
	10	40.58	32.35	22.55	10.54
	20	17.03	13.00	8.835	4.08
RWL	0	61.39	47.70	32.11	15.71
	10	38.48	31.04	21.00	10.28
	20	17.00	12.29	7.41	3.41

tance C of 0 cm is shown in Fig. 4. With a decrease in distance A and distance B, the TE increases.

Quantitative comparisons of the TEs are carried out for the Out-In MR-WPT and the L-shape MR-WPT, as shown in Fig. 4. The two configurations are identical except for a right angle of the two parts. When the *CL* is the same size, i.e., 40 cm, the TEs for the *Out-In* and L-shape MR-WPTs were 78.41% and 64.48%, respectively [5]. This difference, 13.93%, is attributed to the decrease in magnetic coupling between the Tx and Rx coils [8, 9]. The shape and thickness of the load loop, such as the RPL or the RWL, do not affect the TE of the L-shape MR-WPT.

The TEs of the systems with three kinds of the load loops are plotted in Fig. 5. The system with the CL operates best at the

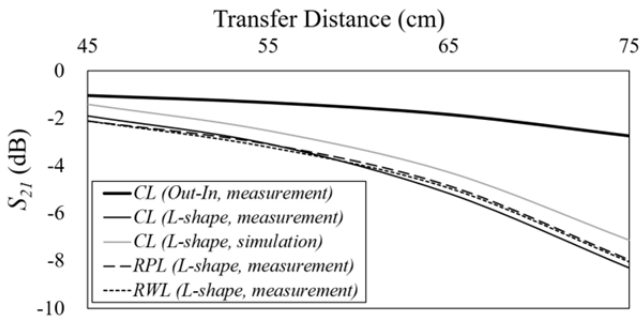

Fig. 4. Simulation and measurement results of TE according to TD.

TDs of 45 to 55 cm. There was a slight difference among the three cases. It should be noted that the shape and the dimension of the load loop do not affect the TE dominantly.

$$Q = \frac{\omega L}{R} \tag{2}$$

The resistance of the bent part of the rectangular loop is relatively higher than any other parts [10]. This affects the Q-factor of *RPL* and *RWL* according to Eq. (2), but the decreasing Q-factor is not enough to decrease S_{21}.

2. Measurement and Simulation of the Practical Applications

During use, the laptop computer could be laid on a misaligned location from the center on the Rx coil. This can cause a decrease in the TE. Depending on the misaligned distance of the load loop on the Rx coil, the magnitude of magnetic coupling in the L-shape MR-WPT can be changed. Note that for the wireless charging product, the optimal locations for the load loop and the Rx coil should be designed such that the TE is the highest. To verify the TE for various locations that a stationary-type electronic device can be laid, the horizontal position on the plane of the Rx coil was divided into 25 square unit sections, as shown in Fig. 6(a). When the center of the *RPL* matched with the center of the arbitrary square unit section, the S_{21} was measured for the specific formation of the L-shape MR-WPT. Dis-

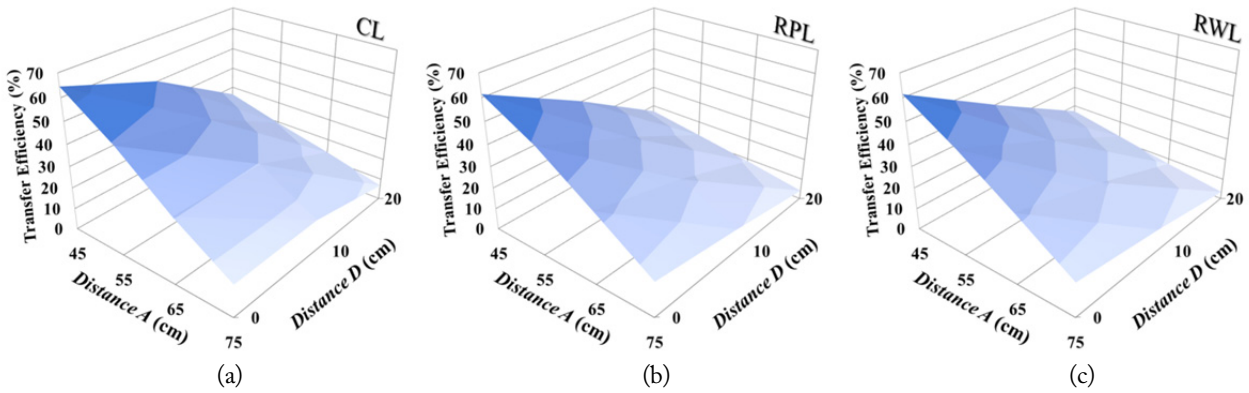

Fig. 5. Measurement results of TE of L-shape MR-WPT (distance B = distance C = 0 cm). (a) CL, (b) RPL, and (c) RWL.

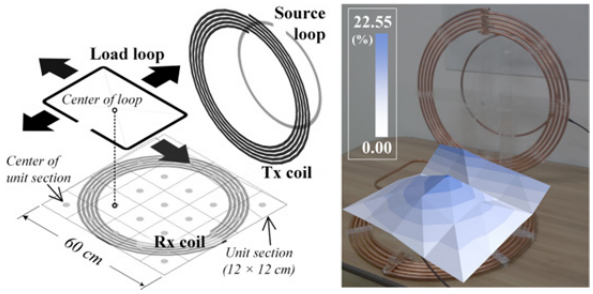

(a) (b)

Fig. 6. TE changes by misalignment of load loop. (a) Measurement method and (b) 3D-distribution of TEs of L-shape MR-WPT.

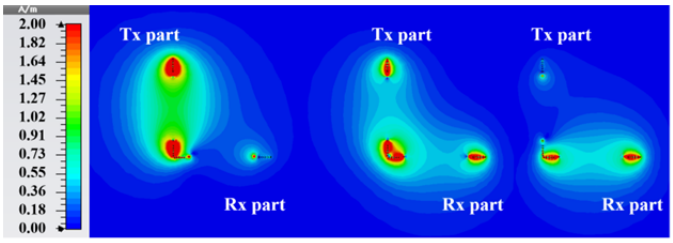

(a) (b) (c)

Fig. 7. Simulation results of H-field distribution of L-shape MR-WPT according to phase differences of H-field. (a) 90°, (b) 180°, and (c) 270°.

tances *A*, *B*, *C*, and *D* were 65 cm, 10 cm, 0 cm, and 28 cm, respectively. In this case, the L-shaped MR-WPT operates at 6.98 ± 0.057 MHz. According to Fig. 6(b), the highest S_{21} was measured when the RPL was located at the center point of the Rx coil. The farther the *RPL* is from the center of the Rx coil, the lower the S_{21} of the L-shape MR-WPT. However, the S_{21} increases as the RPL get close to the junction area of Tx part. This phenomenon is clearly observable in Figs. 7 and 8. Fig. 7 shows the simulation results of the H-field distribution of the proposed system. The power is transferred wirelessly through the magnetic coupling at the junction part between the Tx and Rx coils according to the phase. This is because the intensity of the magnetic flux is populated at the area adjacent to the two Tx and Rx coils when the distance C approaches zero, as shown in Fig. 8. The magnitude of the magnetic field intensity at these

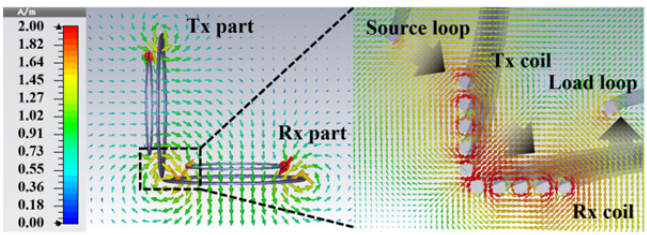

(a) (b)

Fig. 8. Simulation results of the H-field distribution of L-shape MR-WPT. (a) H-field at phase 180° and (b) detailed H-field at junction.

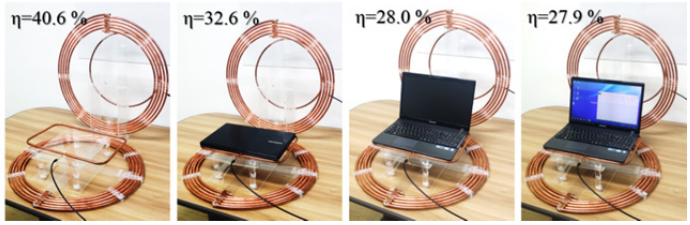

(a) (b) (c) (d)

Fig. 9. Photographs and TEs of L-shape MR-WPT in practical laptop applications. (a) Without laptop computer, (b) monitor closed and non-active, (c) monitor opened and non-active, and (d) monitor open and active.

areas is inversely proportional to the height difference of the coils. Therefore, this trend was common under most conditions of the L-shape MR-WPT including other load loops.

In addition, there are typically two electrical grounds, namely the display panel in the monitor frame and the circuit board in main frame. The conductive ground planes affect the magnetic field and coupling coefficient according to the position of laptop computer. To verify the effect of the conductive ground plane on the TE, a laptop-sized RPL was attached to the bottom of the laptop. As shown in Fig. 9, distance C was 0 cm, and the laptop computer with the load loop was placed over 10 cm from the Rx coil. These experiments showed that electronics such as the display panel and electronic circuit board, prevent the magnetic coupling. The laptop computer with the conductive ground plane affects the magnetic coupling in the proposed system. When the laptop computer was opened, the TE decreased from 32.6% to 28.0%. In contrast, in the active/non-active state of the laptop, there is not much effect on the magnetic coupling of the L-shape MR-WPT. This result shows that the conductive ground plane has a greater impact on the electromagnetic performance than the active/non-active states.

IV. Conclusion

In this paper, we analyzed the proposed MR-WPT system with L-shape configurations for applications to the stationary or mobile devices. The electromagnetic field distributions and TEs of the proposed L-shape MR-WPT were simulated and measured. Results show that the TE of the L-shape MR-WPT is 64.48%, which is at least 13.93% lower than that of the *Out-In* MR-WPT because the mutual inductance is decreased due to the concentration of the magnetic resonant coupling at the junction between the Tx and Rx coils. The shape of the load loop does not affect the TEs of the MR-WPT. As distances *A*, *B*, *C*, and *D* increase, the TEs decrease. In addition, the active/non-active states of the laptop computer do not have much effect on the magnetic resonant coupling between the Tx and Rx parts. This result shows that the conductive ground plane

has a much greater impact on the electromagnetic performance than the active/non-active states of the laptop computer. Although reconfiguration of the MR-WPT caused some performance degradation, the proposed system is highly applicable when considering indoor structures such as L-shaped corner, as compared to the typical and Out-In MR-WPT.

This work was supported by a National Research Foundation (NRF) of Korea Grant funded by the Korean government (No. 2016R1D1A1B02012957).

REFERENCES

[1] A. Kurs, A. Karalis, R. Moffatt, J. D. Joannopoulos, P. Fisher, and M. Soljacic, "Wireless power transfer via strongly coupled magnetic resonances," *Science,* vol. 317, no. 5834, pp. 83–86, 2007.

[2] H. Arai, "Wireless power transfer system," *Journal of the Korean Institute of Electromagnetic Engineering and Science*, vol. 11, no. 3, pp. 143–151, 2011.

[3] G. Kim and B. Lee, "Alternative experimental for mutual inductance and coupling coefficient applied wireless power transfer," *Journal of the Korean Institute of Electromagnetic Engineering and Science,* vol. 16, no. 2, pp. 112–118, 2016.

[4] S. H. Kang and C. W. Jung, "Analysis of WPT system using rearranged indirect-fed method for mobile applications," in *Proceedings of 2015 IEEE Wireless Power Transfer Conference (WPTC)*, Boulder, CO, 2015, pp. 1–4.

[5] S. H. Kang and C. W. Jung, "Magnetic resonant wireless power transfer with rearranged configurations," *Journal of Electromagnetic Engineering and Science*, vol. 17, no. 2, pp. 76–85, 2017.

[6] A. P. Sample, D. T. Meyer, and J. R. Smith, "Analysis, experimental results, and range adaptation of magnetically coupled resonators for wireless power transfer," *IEEE Transactions on Industrial Electronics*, vol. 58, no. 2, pp. 544–554, 2011.

[7] R. Mongia, *RF and Microwave Coupled-Line Circuit*. Boston, MA: Artech House, 2007.

[8] J. G. Hayes, N. O'Donovan, and M. G. O'Donnell, "Inductance characterization of high-leakage transformers," in *Proceedings of 18th Annual IEEE Applied Power Electronics Conference and Exposition (APEC'03)*, Miami Beach, FL, 2003, pp. 1150–1156.

[9] J. Kim, H. Son, D. Kim, K. Kim, and Y. Park, "Efficiency of magnetic resonance WPT with two off-axis self-resonators," in *Proceedings of 2011 IEEE MTT-S International Microwave Workshop Series on Innovative Wireless Power Transmission: Technologies, Systems, and Applications (IMWS)*, Uji, Japan, 2011, pp. 127–130.

[10] S. H. Lee and R. D. Lorenz, "Development and validation of a model for 95%-efficiency 220-W wireless power transfer over a 30-cm air gap," *IEEE Transactions on Industry Applications*, vol. 47, no. 6, pp. 2495–2504, 2011.

Jung Han Choi

received his B.S. and M.S. degrees in Electrical Engineering from the Sogang University, Seoul, Korea, in 1999 and 2001, respectively, and a Dr.–Ing. degree from the Technische Universität München, Munich, Germany in 2004. From 2001 to 2004, he was a research scientist in the Institute for High-Frequency Engineering at the Technische Universität München, Germany. During this time, he worked on high-speed device modeling and circuit development for high-speed optical communications. From 2005 to 2011, he was with the Samsung Advanced Institute of Technology and the Samsung Digital Media & Communication Research Center, where he worked on RF bio sensors, nano device modeling, and circuit design for millimeter wave applications, including 60 GHz CMOS. In 2011, he joined the Fraunhofer Institute (Heinrich-Hertz Institute), Berlin, Germany. His current research interests include active/passive device design and their modeling, high-frequency circuit design, and metamaterials.

Seok Hyon Kang

received his B.S. and M.S. degrees in Optometry from Seoul National University of Science and Technology (SeoulTech), Seoul, Korea, in 2010 and 2014, respectively. He is currently working toward a Ph.D. degree in Electrical Engineering from Seoul National University of Science and Technology (SeoulTech), Seoul, Korea. His current research interest focuses on wireless power transfer.

Chang Won Jung

received his B.S. degree in Radio Science and Engineering from Kwangwoon University, Korea, in 1997, and his M.S. degree in Electrical Engineering from the University of Southern California, Los Angeles, USA, in 2001, He also obtained a Ph.D. in Electrical Engineering and Computer Science from the University of California, Irvine, U.S., in 2005. Since 2008, he has been a professor with the Graduate School of Nano·IT·Design Fusion, Seoul National University of Science and Technology. From 1997 to 1999, he was a research engineer in the wireless communication department of LG Information and Telecommunication in Korea. From 2005 to 2008, he was a senior research engineer in the communication laboratory of Samsung Advanced Institute of Technology, Korea. He has published over 190 papers in refereed journals and conference proceedings, and more than 50 domestic and international patents. His research interests include antennas for MMMB communication systems, multifunctional reconfigurable antennas, EMI/EMC, millimeter-wave applications, wireless power transfer for energy harvesting, transparent RF passive components etc.

JOURNAL OF ELECTROMAGNETIC ENGINEERING AND SCIENCE, VOL. 17, NO. 3, 133~137, JUL. 2017

http://dx.doi.org/10.5515/JKIEES.2017.17.3.133
ISSN 2234-8395 (Online) · ISSN 2234-8409 (Print)

A 28-GHz Wideband 2×2 U-Slot Patch Array Antenna

Nanae Yoon · Chulhun Seo*

Abstract

In this study, a 28-GHz U-slot array antenna for a wideband communication system is proposed. The U-slot patch antenna structure consists of a patch, two U-shaped slot, and a ground plane. With the additional U-slot, the proposed antenna has around 10% of bandwidth at –10 dB. To increase gain, the U-slot antenna is arrayed to 2×2. The proposed antenna is designed and fabricated. The 2×2 array antenna volume is 41.3 mm × 46 mm × 0.508 mm. The proposed antenna was measured and compared with the simulation results to prove the reliability of the design. The bandwidth and gain of the measurement results are 3.35 GHz and 13 dBi, respectively and the operating frequency is around 28 GHz.

Key Words: 28 GHz, 5G, Antenna, U-Slot, Wideband.

I. INTRODUCTION

The development of a 5G system has been begun recently to obtain higher data rates. The standardization activity of 5G is expected to be available in the early 2020s. Compared with a 4G system, the 5G system uses millimeter-wave bands, which are a challenging requirement in the design of an antenna in 5G mobile systems. As the mobile industry looks toward scaling up into the millimeter-wave spectrum, carriers are likely to use the 28, 38, and 73 GHz bands that will become available for future technologies [1–3].

Microstrip antennas have become attractive for use in mobile applications. This antenna has attracted much interest because of its low profile (i.e., compact size), light weight, low cost mass production, and ease of installation. However a major limitation in its application is its narrow bandwidth. The technique that has been used extensively for increasing bandwidth is stacked patches, in which a parasitic element is placed vertically over the lower patch. A microwave antenna that introduces a U-slot or slit into a rectangular radiating patch is a simple and efficient method for obtaining the desired compactness and multiband and broadband properties, as this shape radiates electromagnetic energy efficiently. This design avoids the use of stacked or parasitic patches, and etching U-slot on the patch is simple [4–7].

A 2×2 U-slot patch is used to obtain the design characteristic of a wide bandwidth and a simple structure at around 28 GHz. This antenna frequency is a candidate band for 5G mobile communication. Two U-slots in a single patch antenna is designed, and this antenna is arrayed to increase antenna gain. The proposed structurer is simpler than a stack patch, which has the characteristic of a wideband, but indicates a wide bandwidth.

II. ANTENNA DESIGN

Fig. 1 shows the conventional and the proposed single-patch antenna structures. Fig. 1(a) is the conventional rectangular single-patch antenna structure that is calculated and optimized using patch antenna equations [8]. Fig. 1(b) and (c) present the one and two U-shaped slots etched on the rectangular patch,

Manuscript received May 9, 2017 ; Revised June 20, 2017 ; Accepted July 5, 2017. (ID No. 20170509-021J)
Department of Electronic Engineering, Soongsil University, Seoul, Korea.
*Corresponding Author: Chulhun Seo (e-mail: chulhun@ssu.ac.kr)

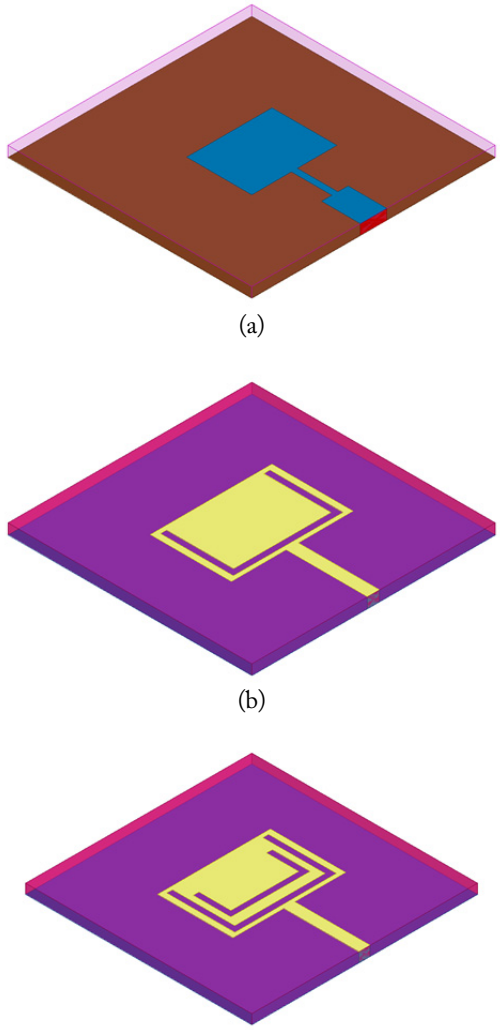

Fig. 1. (a) Conventional, (b) one-U-slot, and (c) two-U-slot single antennas.

respectively. The bottom plane is ground. The U-slot patch introduces an additional resonance frequency [9-10]. Therefore, for ease of control frequency, the antenna with two U-slots is selected. The substrate of the antenna is a Rogers RT/Duroid5880, which has permittivity of 2.2. The dimensions of the conventional antenna and proposed structure are the same to 12 mm × 12 mm × 0.508 mm. The rectangular patch sizes are

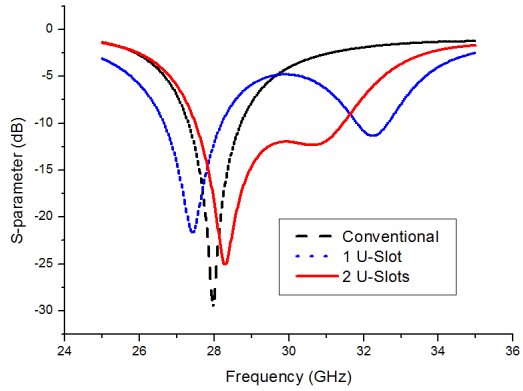

Fig. 2. Simulation result of the single-patch antenna (*S*-parameter).

different. The conventional patch size is 4.2 mm × 3.2 mm and the proposed patch size is 6 mm × 4 mm. The slot thickness of proposed antenna is 0.3 mm. As the operating frequency is high, it needs to be designed with a simple structure; therefore, a microstrip feeding line is used. The antennas are simulated using the ANSYS HFSS EM simulator. Fig. 2 illustrates the characteristic of the *S*-parameter simulation results. The black and blue dash lines represent the S_{11} of the conventional antenna and the one-U-slot patch antenna, respectively. The red solid line is the S_{11} of the proposed antenna. Consequently, the proposed two-U-slot structure obtains a wide bandwidth. The one-U-slot structure has a dual-band frequency. However, as our purpose is to obtain a wide bandwidth, we consider the two-U-slot structure. The proposed structure with two U-slots has a 27.5–31.44 GHz bandwidth, which is approximately 13.36% bandwidth (3.94 GHz) with a center frequency of 29.47 GHz. Fig. 3 shows the simulation results of the radiation pattern. To compare the gain, we indicate the radiation pattern of all structures at the same frequency of 28 GHz. The proposed structure has the highest gain. Comparing the conventional with the proposed structure, the proposed patch size is larger than the conventional one. However, it increases to around 1.8 times more than the conventional patch. The proposed structure has a wider bandwidth than and the highest gain among the three antennas with the same size. Table 1 compares the proposed and conventional antennas. The proposed antenna has a higher

Table 1. Comparison between single and array antennas

	Conventional	1 slot	2 slots	2×2 simulation	2×2 measurement
Patch size (mm)	4.2 × 3.2	6 × 4	6 × 4	6 × 4	6 × 4
Center frequency (GHz)	28.01	27.42 / 32.24 (Dual-band)	29.47	29.01	28.43
Bandwidth (%)	4.93	5.54 / 2.48 (Dual-band)	13.37	14.27	11.8
Gain @28 GHz (dBi)	7.71	7.89	8.57	14.30	13

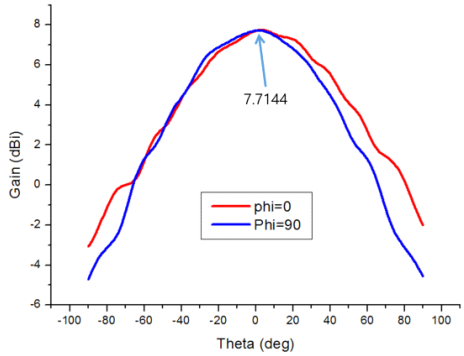

(a)

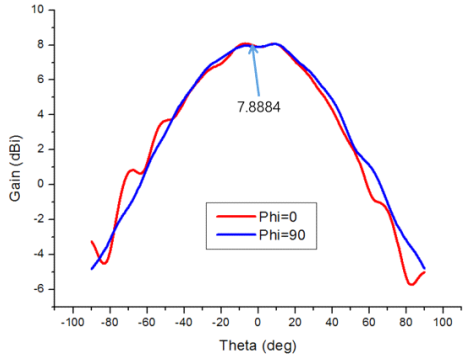

(b)

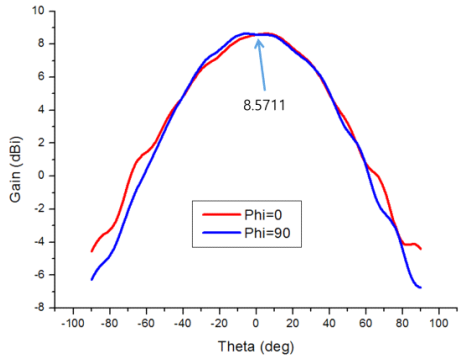

(c)

Fig. 3. Simulation result of the single-patch antenna (radiation pattern): (a) conventional, (b) one-U-slot, and (c) two U-slots.

gain and a wider bandwidth than the conventional antenna.

To increase the gain, the proposed antenna is arrayed to 2×2 as shown in Fig. 4. Each patch distance is greater than the half wavelength because of the reduced mutual coupling effect. The *S*-parameter and radiation pattern simulation results are presented in Fig. 5 [11-14]. The simulation result shows that the bandwidth is 26.94–31.08 GHz (14.27%), and the radiation pattern result indicates a gain of 14.30 dBi. The array antenna has the characteristic of a wide bandwidth. The gain increased to 6 dB because the antenna is arrayed to 2×2.

III. Experiment

Fig. 6(a) and (b) show the fabricated proposed structure its

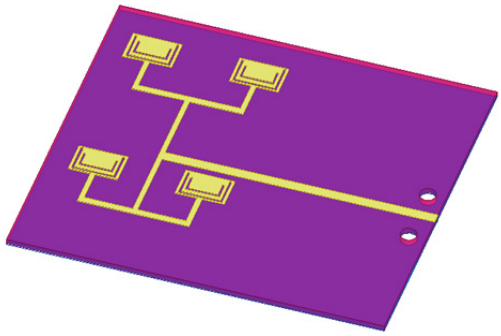

Fig. 4. The proposed 2×2 array antenna.

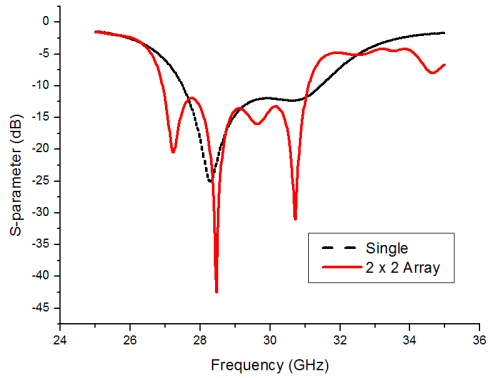

(a)

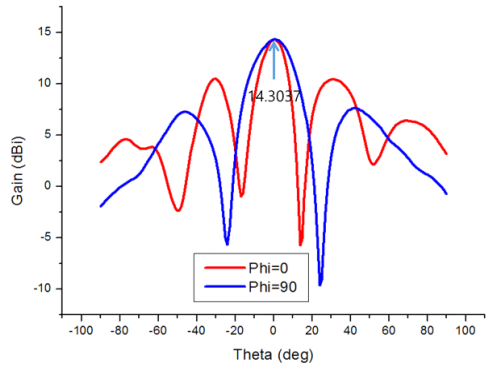

(b)

Fig. 5. Simulation results of the proposed antenna: (a) *S*-parameter and (b) radiation pattern.

measurement setup, respectively. For measuring, the port is connected. The proposed antenna is measured using a network analyzer and a far-field antenna chamber. The measurement results are presented in Fig. 7. Fig. 7(a) illustrates the *S*-parameter with the simulation result. The bandwidth obtained is 11.8%. As shown in Fig. 7(b), the radiation pattern of the proposed antenna is about 13 dBi. Table 1 compares the simulation and measurement results. A good agreement is observed between simulated and the measured results.

IV. Conclusion

This study proposes two 2×2 U-slots array patch antenna for

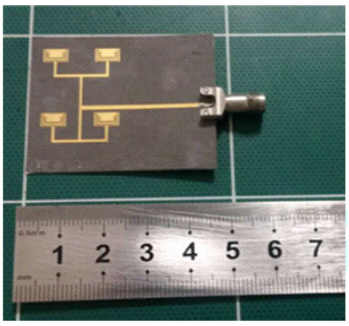

(a)

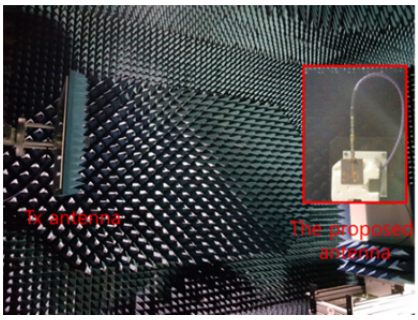

(b)

Fig. 6. Fabrication and measurement of the 2×2 U-slot patch array antenna: (a) fabrication and (b) measurement setup.

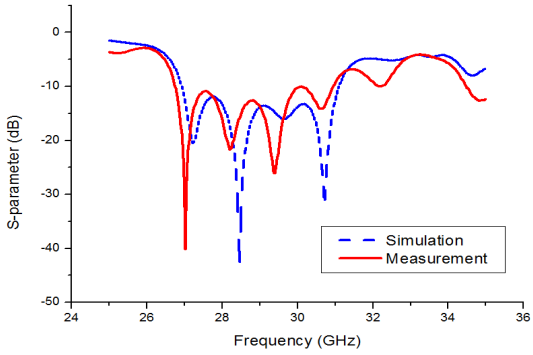

(a)

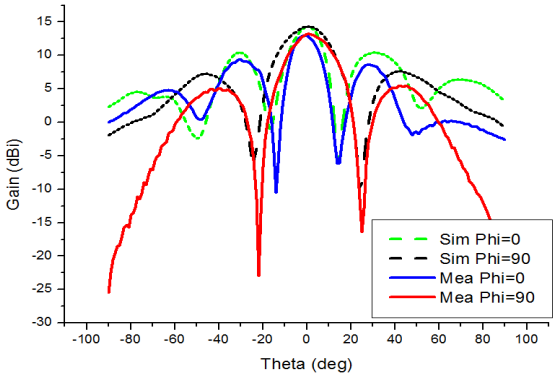

(b)

Fig. 7. Measurement results of the proposed antenna: (a) *S*-parameter and (b) radiation pattern.

a wide band communication application. The operating frequency is around 28 GHz for a 5G system candidate. Compared with the conventional and one-U-slot antenna, the proposed antenna has a wide bandwidth of 11.8% and high gain of 13 dBi. This antenna is an ideal candidate for 5G mobile system applications.

This work was supported by the National Research Foundation of Korea (NRF) grant funded by the Korean government (MSIP) (No. NRF-2017R1A5A1015596).

REFERENCES

[1] T. S. Rappaport, S. Sun, R. Mayzus, H. Zhao, Y. Azr, K. Wang, G. N. Wong, J. K. Schulz, M. Samimi, and F. Guterrez, "Millimeter wave mobile communications for 5G cellular: it will work!," *IEEE Access*, vol. 1, pp. 335–349, 2013.

[2] N. Ojaroudiparchin, M. Shen, S. Zhang, and G. F. Pedersen, "A switchable 3D-coverage phased array antenna package for 5G mobile terminals," *IEEE Antenna and Wireless Propagation Letters*, vol. 15, pp. 1747–1750, 2016.

[3] A. I. Sulyman, A. T. Nassar, M. K. Samimi, G. R. MacCartney, T. S. Pappaport, and A. Alsanie, "Radio propagation path loss models for 5G cellular networks in the 28 GHz and 38 GHz millimeter-wave bands," *IEEE Communications Magazine*, vol. 52, no. 9, pp.78–86, 2014.

[4] J. A. Ansari and R. B. Ram, "Broadband stacked U-slot microstrip patch antenna," *Progress in Electromagnetics Research Letters*, vol. 4, pp. 17–24, 2008.

[5] S. D. Targonski, R. B. Waterhouse, and D. M. Pozar, "Wideband aperture coupled stacked patch antenna using thick substrates," *Electronics Letters*, vol. 32, no. 21, pp. 1941–1942, 1996.

[6] A. Rani and A. K. Gautam, "Improvement in gain and bandwidth of rectangular and U slot loaded patch," *International Journal of Computer Science Issues*, vol. 8, pp. 283–288, 2011.

[7] D. Uzer, S. S. Gultekin, and O. Dundar, "Estimation and design of U-slot physical patch parameters with artificial neural networks," in *Proceedings of Progress in Electromagnetics Research Symposium*, Kuala Lumpur, Malaysia, 2012, pp. 27–30.

[8] C. A. Balanis, *Antenna Theory: Analysis and Design*. Hoboken, NJ: John Wiley & Sons Inc., 2005.

[9] K. F. Lee and K. M. Luk, *Microstip Patch Antennas*. London: Imperial College Press, 2010.

[10] S. Weigand, G. H. Huff, K. H. Pan, and J. T. Bernhard,

"Analysis and design of broad-band single-layer rectangular U-slot microstip patch antennas," *IEEE Transactions on Antennas and Propagation*, vol. 51, no. 3, pp. 457–468, 2003.

[11] J. I. Lee, B. M. Lee, and Y. J. Yoon, "CPW feed wideband U-slot microstrip antenna," *Journal of the Korea Electromagnetics Engineering Society*, vol. 2, no. 1, pp. 11–15, 2002.

[12] R. A. Bhatti, B. Y. Park, Y. T. Im, and S. O. Park, "Design of a planar slotted waveguide array antenna for X-band radar applications," *Journal of the Korea Electromagnetics Engineering Society*, vol. 11, no. 2, pp. 97–104, 2011.

[13] H. Kaouach, A. Kabashi, and M. T. Simsim, "Bandpass antenna-filter-antenna arrays for millimeter-wave filtering applications," *Journal of Electromagnetic Engineering and Science*, vol. 15, no. 4, pp. 206–212, 2015.

[14] G. Byun, J. C. Hyun, S. M. Seo, and H. Choo, "Optimum array configuration to improve null steering time for mobile CRPA systems," *Journal of Electromagnetic Engineering and Science*, vol. 16, no. 2, pp. 74–79, 2016.

Nanae Yoon

received her B.S. degree in electronics engineering from Kangnam University, Korea in 2011 and her M.S. degree in electronics engineering from Soongsil University, Korea, in 2013. She is currently pursuing the Ph.D. degrees in Information and Communication Engineering at Soogsil University, Seoul, Korea.

Chulhun Seo

received B.S., M.S., and Ph.D. degrees from Seoul National University, Seoul, Korea, in 1983, 1985, and 1993, respectively. From 1993 to 1995, he was with the Massachusetts Institute of Technology (MIT), Cambridge, MA, USA, as a Technical Staff Member. From 1993 to 1997, he was with Soongsil University, Seoul, Korea, as an assistant professor. From 1999 to 2001, he was with MIT as a visiting professor. From 1997 to 2004, he was with Soongsil University as an associate professor. Since 2004, he has been a professor of electronic engineering with Soongsil University. He was IEEE MTT Korea Chapter Chairman from 2011 to 2014. He is the President of the Korean Institute of Electromagnetic Engineering and Science (KIEES) and Dean of Graduate School at Soongsil University. He is the director of the Center for Intelligent Biomedical Wireless Power Transfer supported by the National Research Foundation of Korea (NRF) grant funded by the by the MSIP. His research interests include wireless technologies, antenna, and metamaterials.

JOURNAL OF ELECTROMAGNETIC ENGINEERING AND SCIENCE, VOL. 17, NO. 3, 138~146, JUL. 2017

http://dx.doi.org/10.5515/JKIEES.2017.17.3.138
ISSN 2234-8395 (Online) · ISSN 2234-8409 (Print)

New Configuration of a PLDRO with an Interconnected Dual PLL Structure for K-Band Application

Yuseok Jeon[1,*] · Sungil Bang[2]

Abstract

A phase-locked dielectric resonator oscillator (PLDRO) is an essential component of millimeter-wave communication, in which phase noise is critical for satisfactory performance. The general structure of a PLDRO typically includes a dual loop of digital phase-locked loop (PLL) and analog PLL. A dual-loop PLDRO structure is generally used. The digital PLL generates an internal voltage controlled crystal oscillator (VCXO) frequency locked to an external reference frequency, and the analog PLL loop generates a DRO frequency locked to an internal VCXO frequency. A dual loop is used to ease the phase-locked frequency by using an internal VCXO. However, some of the output frequencies in each PLL structure worsen the phase noise because of the *N* divider ratio increase in the digital phase-locked loop integrated circuit. This study examines the design aspects of an interconnected PLL structure. In the proposed structure, the voltage tuning; which uses a varactor diode for the phase tracking of VCXO to match with the external reference) port of the VCXO in the digital PLL is controlled by one output port of the frequency divider in the analog PLL. We compare the proposed scheme with a typical PLDRO in terms of phase noise to show that the proposed structure has no performance degradation.

Key Words: Analog PLL, Digital PLL, Dual-Loop, Front-End, Phase-Locked PLL, PLDRO.

I. Introduction

In microwave communication systems that require high-capacity data transmission such as satellites' base station systems and electronic warfare (EW), the local oscillators at the transmitter/receiver terminals should maintain the characteristics of low phase noises and excellent spectral purity [1].

As the frequency resources of C, S, and Ku bands for such microwave communication systems have already been saturated, frequency resources should be developed in the K and Ka bands, which are quasi-millimeter wave bands (18–40 GHz) [2].

Digital modulation systems are used to transmit high-capacity data at high speeds using the K band. In particular, in the case of phase modulation systems, the oscillator characteristics of high-stability and low-phase noises are required because the frequency stability and phase noise characteristics have major effects on the beat error ratio characteristics [3]. In the fields of radars and electronic warfare, precise frequencies up to several MHz or several hundred kHz (e.g., 9.625xx GHz) are required for oscillators instead of integer multiples of the external reference frequency.

Satellite communication base stations and EW systems require the characteristics of the in-band phase noises of the local oscillators of microwave communication systems, which use the Ka-band or millimeter bands not to exceed –70 dBc/Hz at the offset frequency of 1 kHz and –90 dBc/Hz at the offset fre-

Manuscript received March 21, 2017 ; Revised June 7, 2017 ; Accepted July 11, 2017. (ID No. 170321-014J)
[1]Research and Development Department, Broadern Inc., Hwaseong, Korea
[2]Division of Electronic and Electric Engineering, Dankook University, Yongin, Korea.
[*]Corresponding Author: Yuseok Jeon (e-mail: halsuida@naver.com)

quency of 100 kHz according to the center frequency specified by IESS-308. Therefore, phase-locked dielectric resonator oscillators (PLDROs) are widely used to satisfy the required standards [4].

In the case of existing PLDROs, the internal voltage controlled crystal oscillator (VCXO) frequency is phase-locked at the external reference frequency in the primary digital phase-locked loop (PLL) circuit, and the phase-locked VCXO frequency and the DRO output frequency are phase-locked and used in sequence in the secondary analog PLL circuit. In this case, if the internal VCXO frequency is not an integer multiple (e.g., 96 MHz) of the external reference frequency (10 MHz) but a complicated frequency (e.g., 96.25 MHz), the comparison frequency will become smaller when the phase is compared in the phase detector (PFD) of the integer phase-locked loop integrated circuit (PLLIC). Accordingly, the divider ratio of the PLLIC increases, thus resulting in bad phase noise characteristics.

To output precise frequencies, two loops (digital PLL and analog PLL) are used together for each change in frequency. In this case, the divider ratio of the PLLIC of the digital PLL circuit for primary phase comparison with the external reference frequency (10 MHz) increases and leads to bad phase noise characteristics in the in-band loop bandwidth of the analog PLL circuit (final output frequency) [5–7].

The proposed PLDRO is in a new structure in which no phase noise deterioration occurs in the analog loop filter band, and the output frequency can be freely adjusted. Recently, precision to several hundred kHz (e.g., 9.625xx GHz) has been required as the center frequency of local oscillators in accordance with the requirements of communication systems.

A design equation for the proposed PLL structure was derived and presented in this study.

The output frequency of the DRO was coupled and made to pass through the frequency divider and the phase was directly compared with that of the external reference frequency (10 MHz) in the PLLIC. Then, the error voltage that corresponds to the phase difference was made to pass through the loop filter to control the voltage tuning (VT) terminal of the VCXO. To verify theprposed PLDRO, a new PLL with 9.625 GHz band was designed. The final output frequency was multiplied by two to become 19.25 GHz, and the result was experimentally verified. Fig. 1 shows the block diagram of the proposed PLDRO structure.

II. Circuit Topology

The concept of the proposed PLDRO is configured as an interconnected dual-loop PLL structure, in which a digital PLL and an analog PLL are interconnected. The proposed PLDRO is designed so that the phase error voltage resulting from the

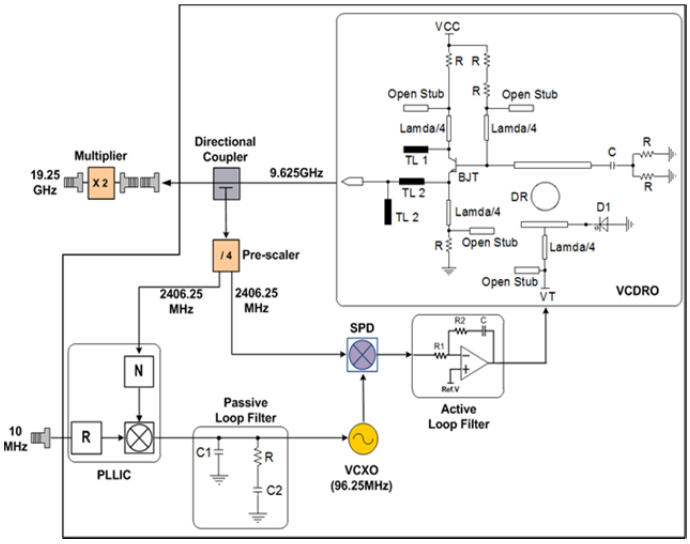

Fig. 1. Block diagram of the proposed total PLDRO.

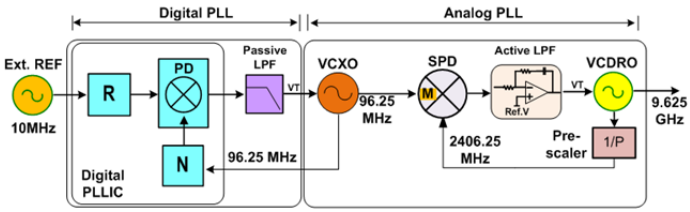

Fig. 2. Block diagram of the general PLDRO.

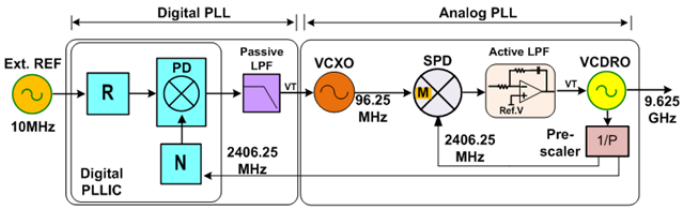

Fig. 3. Block diagram of the proposed PLDRO.

phase comparison between the reference frequency input and the output frequency of the VCDRO controls the VT terminal of the VCXO, which is not a subject of the direct comparison.

Fig. 2 shows the block diagram of the general PLDRO for the independent PLL loop flow. The increase in the *N* divider ratio is related to the complex frequency of the VCXO (96.25 MHz), as the phase should be compared with the external reference in the digital PLL configuration. Fig. 3 presents the block diagram of the proposed PLDRO for the PLL loop flow.

The phase of the output frequency of the VCDRO divided by four and that of the external reference frequency (10 MHz) are directly compared with the PFD to output the error voltage, which corresponds to the phase difference between the two signals. The error voltage controls the VT terminal of the VCXO, which is not a subject of direct phase comparison, through the secondary manual loop filter, which has the characteristics of low-pass filters. Thereafter, the controlled VCXO controls the

VCDRO, and the error voltage is obtained through the phase comparison with the harmonics multiplied 25 times in the sampling phase detector (SPD) through the analog loop filter.

Then, the output frequency of the VCDRO that corresponds to the phase error voltage is inputted into the phase detector of the PLLIC, and the above process is repeated until the VCXO comes under the in-phase condition. This way, as the phase is compared with the output frequency of the VCDRO instead of the integer multiple of the external reference frequency (10 MHz), only the VCXO, which is a subject of the PLL circuit, is followed, and the deterioration of phase noises resulting from the increase in the divider ratio does not occur within the analog PLL bandwidth. That is, by changing only the frequency of the VCXO, the output frequency of the PLDRO can be freely implemented to the precise frequencies of several hundred kHz.

As shown in Fig. 3, the output frequency is as follows:

$$f_{OUTPUT} = (PXM) f_{VCXO}, \tag{1}$$

where P is the divider ratio(4) of the pre-scaler, f_{VCXO} is the output frequency (96.25 MHz) of the internal VCXO, and M is the number of multiplication (25) of the SPD. The secondary passive loop filter of the digital PLL of the proposed PLDRO shown in Fig. 1 is presented in Fig. 4. The impedance transfer function is as follows:

$$Z(s) = \frac{1 + s\tau_2}{sc_t(1 + s\tau_1)}, \quad \tau_1 = \frac{RC_1C_2}{c_t}, \quad \tau_2 = RC_2 \tag{2}$$

$$C_t = \frac{K_\varphi K_{VCO}}{N\omega^2_C} \cdot \sqrt{\frac{(1 + \omega^2_C \tau^2_2)}{(1 + \omega^2_C \tau^2_1)}} \tag{3}$$

where $K_\emptyset$ is the phase detector gain (V/rad), K_{VCO} is the VCXO gain (Hz/V), ω_C is the loop bandwidth, and N is the divider ratio, which is a value obtained by dividing the VCXO frequency by the comparison frequency (PFD).

The secondary active loop filter of the analog PLL of the proposed PLDRO shown in Fig. 1 is presented in Fig. 5. The transfer function is as follows:

$$F(s) = \frac{\tau_2 s + 1}{\tau_1 s}, \quad \tau_1 = R_1C, \quad \tau_2 = R_2C \tag{4}$$

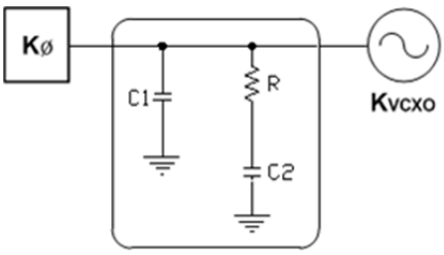

Fig. 4. Secondary passive loop filter of the digital PLL.

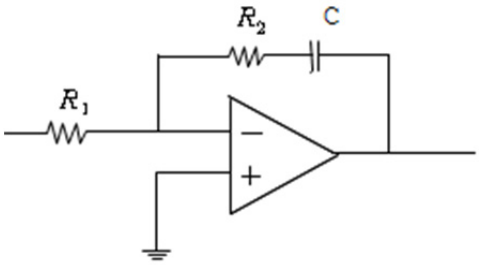

Fig. 5. Secondary active loop filter of the analog PLL.

III. Design and Simulation

The components that contribute to the noises inserted into the interconnected dual-loop PLLs of the proposed PLDRO structure are shown in Fig. 6. The noise term variables are as follows:

ϕ_{nR} : Reference VCXO phase noise

ϕ_{nM} : Reference divider or SRD phase noise

ϕ_{nO} : Total output phase noise

ϕ_{nN} : Pre-scaler divider phase noise

ϕ_{nDRO} : DRO phase noise

V_{nPD} : Phase detector phase noise

V_{nLPF} : Loop amplifier phase noise

The phase noise in the PLDRO final output is derived by Eq. (5):

$$\varphi_{nO} = \left\{\left\{\left[\left(\frac{\varphi_{nR}}{M} + \varphi_{nM}\right) - \left(\frac{\varphi_{nO}}{N} + \varphi_{nN}\right)\right] \cdot K_{PD} + V_{nPD} + V_{nLPF}\right\} H(s)\right\} \cdot \frac{K_{DRO}}{s} \cdot \varphi_{nDRO}, \tag{5}$$

where

K_{DRO} is the VC-DRO modulation sensitivity(radians /second per volt)

K_{PD} is the PD or SPD output sensitivity (volts per radian)

$H(s)$ is the loop filter transfer function

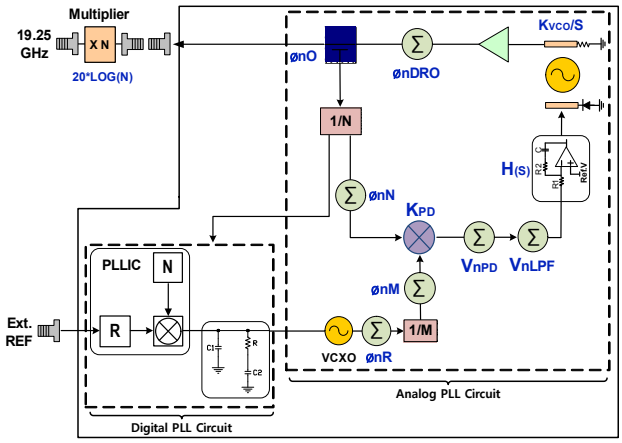

Fig. 6. Phase noise generator in the proposed PLDRO structure.

N is the DRO divider ratio
M is the reference divider ratio

Eq. (5) shows that the loop filter transfer function $H(s)$ is connected to individual noise sources in the analog PLL loop band except for the free-running phase noise of the DRO. In particular, the phase noise characteristics of the VCXO corresponding to the internal reference frequency in the analog PLL circuit directly affect the phase noises in the loop filter band. That is, if the phase noise characteristics of the VCXO are poor, the final output phase noise will be poor in the PLL loop band [8].

How the digital PLL circuit affects the phase noise of the VCXO, which is not a subject of direct phase comparison, is examined in Section III-1, and the phase noise of the final output (analog PLL circuit) is analyzed in Section III-2.

1. Analysis of the Phase Noise of the Digital PLL Circuit

The overall phase noise of the digital PLL is as follows (Table 1):

$$TotalPN = 10 * LOG(10^{\frac{VCXOsPN}{10}} + 10^{\frac{REFsPN}{10}} + 10^{\frac{PSsPN}{10}} + 10^{\frac{PDsPN}{10}}). \quad (6)$$

Eq. (6) obtains the final output phase noise of the digital PLL circuit. The characteristics of the individual components are as follows:

The phase noise of the VCXO output under No. 1 is the value after passing the high pass attenuation of the passive loop filter. The phase noise of the reference output under No. 2 is the value after an increase by the N divider ratio. This value is one (3850) set in the PLLIC but a value (9.625) obtained by dividing the VCXO frequency by the external reference frequency followed by passing the low pass attenuation by the passive loop filter. The phase noise of the pre-scaler output under No. 3 is a value after passing the low pass attenuation by the passive loop filter. The phase noise of the phase detector output under No. 4 can be calculated by Eq. (7), followed by passing through the low pass attenuation by the passive loop filter.

$$\text{Close-in phase noise} = PLLIC's\ noise\ floor - 10 * LOG(PFD) - 20 * LOG(N), \quad (7)$$

where PFD is the phase frequency detector, and N is the divider and pre-scaler ratio of the digital PLLIC.

The results of the calculation of the above equation using Excel are as shown in Table 1.

As the VCXO in the digital PLL circuit is not included in the closed loop PLL route regardless of the increase in the number of N the divider ratio, the pure phase noise characteristics of VCXO can be maintained outside the loop filter band without affecting the phase noise. The phase noise values in the digital PLL circuit calculated as such are –138.6 dBc/Hz and –148.9 dBc/Hz at 1 kHz and 10 kHz offset frequencies for 96.25 MHz, respectively.

2. Analysis of the Phase Noise in the Final Output (Analog PLL Circuit)

The overall phase noise of the analog PLL (Table 2) is as follows:

$$TotalPN = 10 * LOG(10^{\frac{DROsPN}{10}} + 10^{\frac{REFsPN}{10}} + 10^{\frac{PSsPN}{10}} + 10^{\frac{PDsPN}{10}}). \quad (8)$$

The phase noise of the final output is calculated by Eq. (8). The characteristics of the individual components are as follows:

The phase noise of the DRO output under no.1 is the value after passing the high pass attenuation by the active loop filter. The phase noise of the reference output under No. 2 is the phase noise of the VCXO, which is the value after an increase

Table 1. Phase noise calculation for the proposed PLDRO (digital PLL)

Digital PLL (VCXO)	BW (kHz)	PFD (MHz)	F_O (GHz)	N		
96.25 MHz PLVCXO	0.1	10	0.09625	9.625		
Frequency [Hz] @ OFFSET	10	100	1,000	1.0E+04	1.0E+05	1.0E+06
VCXO phase noise	-88	-115	-140	-149	-160	-160
Reference phase noise	-108	-140	-150	-155	-155	-155
Pre-scaler phase noise	-135	-140	-145	-148	-148	-148
PD phase noise	-125.3	-125.3	-125.3	-125.3	-125.3	-125.3
High Pass Attenuation (LF)	20.0	0.0	0.0	0.0	0.0	0.0
Low Pass Attenuation (LF)	0.0	0.0	20.0	40.0	60.0	80.0
Reference multiply	-88.3	-120.3	-130.3	-135.3	-135.3	-135.3
No.1 VCXO output	-108.0	-115.0	-140.0	-149.0	-160.0	-160.0
No.2 Reference output	-88.3	-120.3	-150.3	-175.3	-195.3	-215.3
No.3 Pre-scaler output	-135.0	-140.0	-165.0	-188.0	-208.0	-228.0
No.4 Phase detector output	-125.3	-125.3	-145.3	-165.3	-185.3	-205.3
Total phase noise	-88.3	-113.6	-138.6	-148.9	-160.0	-160.0

Table 2. Phase noise calculation for the proposed PLDRO (analog PLL)

Analog PLL (DRO)	BW (kHz)	PFD (MHz)	F_O (GHz)	N		
9.625 GHz PLDRO	100	100	9.625	96.25		
Frequency [Hz] @ OFFSET	10	100	1,000	1.0E+04	1.0E+05	1.0E+06
DRO phase noise	-30.0	-50.0	-90.0	-100.0	-120.0	-130.0
Reference phase noise	-88.3	-113.6	-138.6	-148.9	-160.0	-160.0
Pre-scaler phase noise	-125	-130	-140	-150	-150	-150
PD phase noise	-125.0	-125.0	-125.0	-125.0	-125.0	-125.0
High Pass Attenuation (LF)	140.0	100.0	60.0	20.0	0.0	0.0
Low Pass Attenuation (LF)	0.0	0.0	0.0	0.0	0.0	20.0
Reference multiply	-48.6	-73.9	-98.9	-109.2	-120.3	-120.3
No.1 DRO output	-170.0	-150.0	-150.0	-120.0	-120.0	-130.0
No.2 Reference output	-48.6	-73.9	-98.9	-109.2	-120.3	-140.3
No.3 Pre-scaler output	-125.0	-130.0	-140.0	-150.0	-150.0	-170.0
No.4 Phase detector output	-125.0	-125.0	-125.0	-125.0	-125.0	-145.0
Proposed PDRO's phase nose	-48.6	-73.9	-98.9	-108.8	-116.5	-129.5
19.25G PLDRO PN (X2)	-42.6	-67.9	-92.9	-102.7	-110.5	-123.5

by the N divider ratio—a product of the number of multiplication (25) of the SRD in the SPD and the divider ratio (4) of division by four, followed by the low pass attenuation by the active loop filter. The phase noise of the pre-scaler output under No. 3 is the phase noise characteristic of the divider (1/4), which is the value after passing the low pass attenuation by the active loop filter, used separately. The phase noise of the phase detector output under No. 4 is the phase noise characteristic of the SPD, which is a value after passing the low pass attenuation by the active loop filter. The results of the calculation of the above equation using Excel are shown in Table 2.

The final phase noise values of 9.625 GHz calculated as such are –98.9 dBc/Hz and –108.8 dBc/Hz at 1 kHz and 10 kHz offset frequencies for 9.625 GHz, respectively.

If 9.625 GHz is changed into the K band (19.25 GHz) using a doubler, the phase noise values will change as follows (deteriorated by 20*log(N)): –92.9 dBc/Hz and –102.7 dBc/Hz at 1 kHz and 10 kHz offset frequencies for 9.625 GHz, respectively. Fig. 7 shows the results of the analysis of the phase noise of the K-band (19.25 GHz) after the multiplication of the proposed PLDRO by two. The values satisfy both the Intelsat Earth Station Standard and the IESS-308 standard. The actual results of the measurement are presented in Section IV. As shown by the results indicated in blue, in the case of the general PLDRO, if the digital PLL and the analog PLL are independently implemented, the IESS-308 standard will not be observed in the 1 kHz offset frequency because of the increase in the N divider of the digital PLL circuit.

As indicated by the blue line in the general PLDRO in Fig. 7, the results of the calculation using Excel are presented in Tables 3 and 4.

The results shown in Table 5 are indicated to be worse than

Table 3. Phase noise calculation for the general PLDRO (digital PLL)

Digital PLL (VCXO)	BW (kHz)	PFD (MHz)	F_O (GHz)	N		
96.25 MHz PLVCXO	0.1	0.25	0.09625	385		
Frequency [Hz] @ OFFSET	10	100	1,000	1.0E+04	1.0E+05	1.0E+06
VCXO phase noise	-88	-115	-140	-149	-160	-160
Reference phase noise	-108	-140	-150	-155	-155	-155
Pre-scaler phase noise	-135	-140	-145	-148	-148	-148
PD phase noise	-109.3	-109.3	-109.3	-109.3	-109.3	-109.3
High Pass Attenuation (LF)	20.0	0.0	0.0	0.0	0.0	0.0
Low Pass Attenuation (LF)	0.0	0.0	20.0	40.0	60.0	80.0
Reference multiply	-56.3	-88.3	-98.3	-103.3	-103.3	-103.3
No.1 VCXO output	-108.0	-115.0	-140.0	-149.0	-160.0	-160.0
No.2 Reference output	-56.3	-88.3	-118.3	-143.3	-163.3	-183.3
No.3 Pre-scaler output	-135.0	-140.0	-165.0	-188.0	-208.0	-228.0
No.4 Phase detector output	-109.3	-109.3	-129.3	-149.3	-169.3	-189.3
Total phase noise	-56.3	-88.2	-117.9	-141.5	-158.0	-160.0

Table 4. Phase noise calculation for the general PLDRO (analog PLL)

Analog PLL (DRO)	BW (kHz)	PFD (MHz)	F_O (GHz)	N	PD(PN)	
9.625 GHz PLDRO	100	100	9.625	96.25	-125	
Frequency [Hz] @ OFFSET	10	100	1,000	1.0E+04	1.0E+05	1.0E+06
DRO phase noise	-30.0	-50.0	-90.0	-100.0	-120.0	-130.0
Reference phase noise	-56.3	-88.2	-117.9	-141.5	-158.0	-160.0
Pre-scaler phase noise	-125	-130	-140	-150	-150	-150
PD phase noise	-125.0	-125.0	-125.0	-125.0	-125.0	-125.0
High Pass Attenuation (LF)	140.0	100.0	60.0	20.0	0.0	0.0
Low Pass Attenuation (LF)	0.0	0.0	0.0	0.0	0.0	20.0
Reference multiply	-16.6	-48.6	-78.3	-101.8	-118.3	-120.3
No.1 DRO output	-170.0	-150.0	-150.0	-120.0	-120.0	-130.0
No.2 Reference output	-16.6	-48.6	-78.3	-101.8	-118.3	-140.3
No.3 Pre-scaler output	-125.0	-130.0	-140.0	-150.0	-150.0	-170.0
No.4 Phase detector output	-125.0	-125.0	-125.0	-125.0	-125.0	-145.0
General PDRO's phase nose	-16.6	-48.6	-78.3	-101.7	-115.5	-129.5
19.25G PLDRO PN(X2)	-10.6	-42.6	-72.2	-95.7	-109.5	-123.5

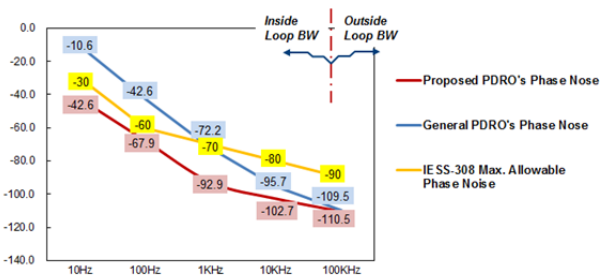

Fig. 7. Graph of the analysis of the phase noise of the proposed PLDRO (9.625 GHz X2 = 19.25 GHz).

Table 5. Summary of Tables 3 and 4

Offset freq.	10 Hz	100 Hz	1 kHz	10 kHz	100 kHz
Digital PLL	-56.3	-88.2	-117.9	-141.5	-158.0
Analog PLL	-16.6	-48.6	-78.3	-101.7	-115.5
After X2	-10.6	-42.6	-72.2	-95.7	-109.5

those of the proposed PLDRO.

IV. Fabrication and Measurement

A PLDRO of 9.625 GHz was implemented on the basis of the proposed PLDRO structure. The frequency is multiplied by two so that the final output frequency is 19.25 GHz. The final output frequency is applied to the local oscillator of the K-band microwave system. In this case, a crystal oscillator of 10 MHz is used for the external reference frequency to obtain the output frequency of 9.625 GHz from the VCDRO. The set values of the individual parameters of the PLLIC are R = 16, REF = 10, and N = 3,850.

The external reference frequency 10 MHz is directly entered into the PLLIC, and the output frequency 9.625 GHz of the VCDRO is divided by four into 2,406.25 MHz. Then, one of the divided frequencies is entered into the PLLIC and another one into the SPD. The phase detector in the PLLIC compares the phase with the VCDRO, and the relevant phase error voltage is connected with the VT terminal of the VCXO. The output frequency 96.25 MHz of the VCXO is multiplied by 25 in the SRD of the SPD to generate 2,406.25 MHz harmonic signals. The phase is compared with that of the output frequency 2,406.25 MHz divided by four of the VCDRO.

As shown in Fig. 8, the VCDRO is designed in the form of a series feedback. The 50-Ω line is connected to the input terminal of the active element to select the location of the DR. therefore, the resonance conditions are formed at the resonance frequency of the dielectric resonator to obtain excellent phase noise characteristics. The VCDRO is designed to oscillate at 9.625 GHz using the BJT element and the high-Q DR (dielectric

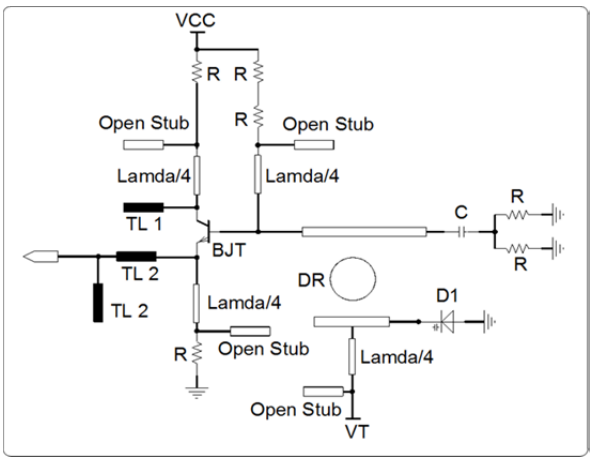

Fig. 8. Voltage-controlled DRO circuit.

resonator). The emitter TL2 of the BJT element is for making the transistor unstable and for output impedance matching. The collector TL1 of the BJT element determines the oscillation frequency and phase noise. The varactor diode (D1) is used to change the internal capacity value of the varactor diode using the phase error voltage output from the SPD through the active loop filter to tune the VT terminal (VT range, 0–12 V).

The analog PLL is implemented with secondary active filters and is designed to have a bandwidth of approximately 100 kHz to obtain optimum phase noise characteristics. To lock the phase, a Schmitt trigger comparator and an integrator are used as frequency acquisition and search circuits, respectively. The integer PLLIC and VCXO (96.25 MHz) with excellent phase noises are adopted for the digital PLL circuit. The doubler is multiplied using passive components, so that it can be operated in the K-band. A band pass filter is applied to remove spurious bands other than the operating frequency.

Fig. 9 shows the output power of PLDRO with +17.07 dBm at the 200 kHz span for 9.625 GHz before multiplication. Fig. 10 presents the output power of PLDRO with +14.43 dBm at the 5 GHz span for 19.25 GHz after multiplication.

The measurement results of the SSB phase noises (dBc/Hz)

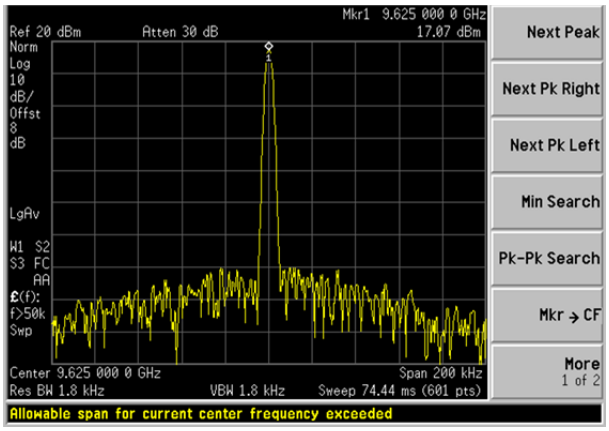

Fig. 9. Measurement results of the output power at the 9.625 GHz output frequency (before multiplication by two).

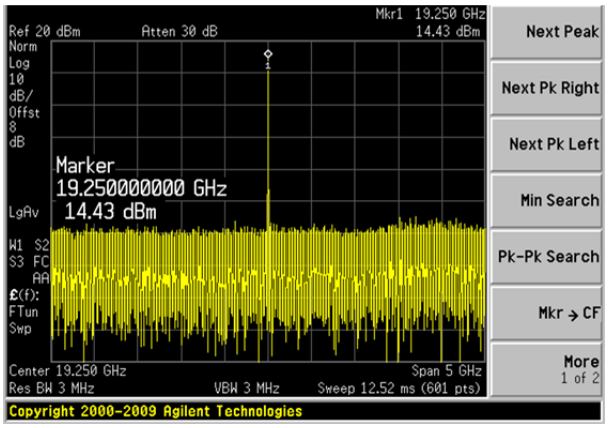

Fig. 10. Measurement results of the output power at the 19.25 GHz output frequency (after multiplication by two).

of the implemented PLDRO at the 9.625 GHz output frequency before multiplication by two and at the 19.25 GHz output frequency after multiplication by two are shown in Figs. 11 and 12, respectively.

The phase noises measured at a 19.25-GHz output frequency after multiplication by two are –96.5 dBc/Hz and –103.3 dBc/Hz at 1 kHz and 10 kHz offset frequencies, respectively. As shown in Table 6, the phase noises are improved by at least 22 dBc/Hz under IESS-308, which is a standard for Intelsat base stations, and the 19.25 GHz K-band after multiplication by two.

In addition, the measurement results are consistent with the

Table 6. Comparison of phase noises measured at 9.625 GHz, 19.25 GHz after multiplication, and IESS-308 standard

Offset freq.	100 Hz	1 kHz	10 kHz	100 kHz	1 MHz
9.625 GHz	-75.2	-99.9	-109.1	-117.8	-132
19.25 GHz	-69.4	-96.5	-103.2	-113.4	-127
IESS-308	-60	-70	-80	-90	-

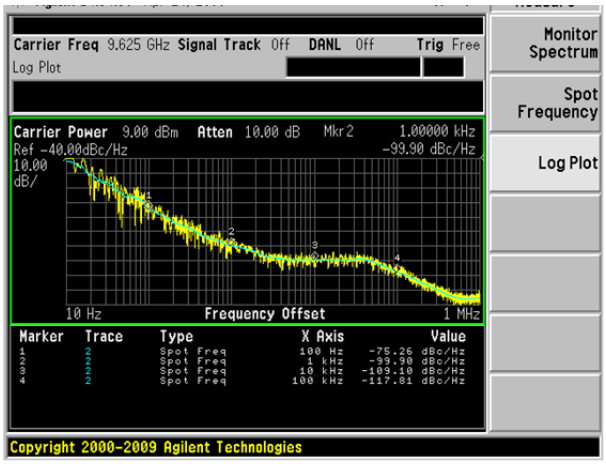

Fig. 11. Measurement results of the phase noises at the 9.625 GHz output frequency (before multiplication by two).

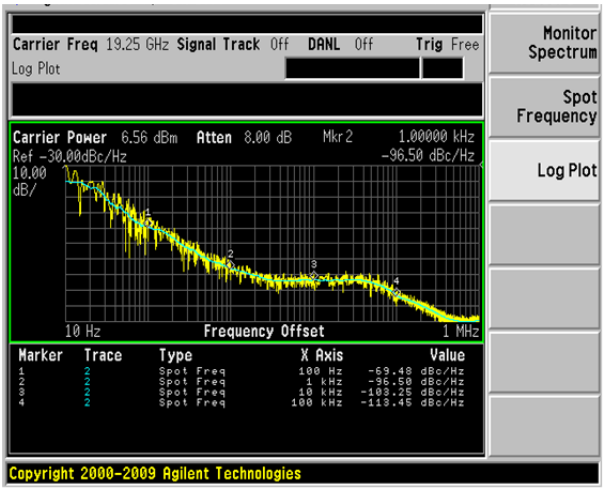

Fig. 12. Measurement results of the phase noises at 19.25 GHz output frequency (after multiplication by two).

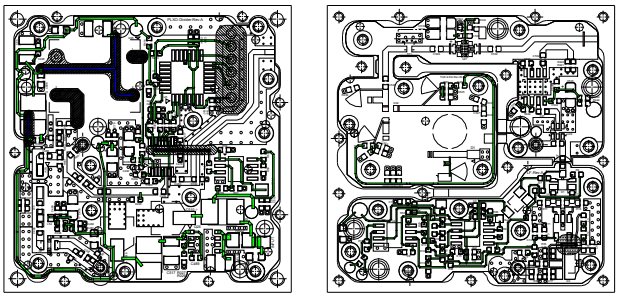

Fig. 13. CAD model of the proposed PLDRO.

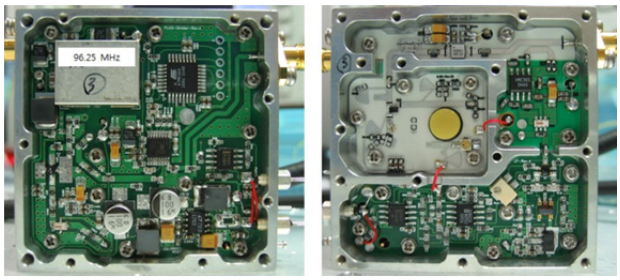

Fig. 14. Real photos of the proposed PLDRO.

phase noise values analyzed and predicted in Section III. The results demonstrate that the proposed PLDRO structure is effective.

Figs. 13 and 14 show the CAD file and photos of the inside of the proposed PLDRO actually fabricated. The left figure illustrates the digital PLL circuit and the right one shows the analog PLL circuit.

V. Conclusion

In the present study, a new PLDRO structure with excellent phase noise characteristics is proposed. PLDROs with low phase noises have been developed to be used as local oscillators in the field of wireless communication, in which PLDROs are installed at the front end of devices.

Based on the proposed structure, the PLDRO in the new form is designed to be used as a local oscillator of transmitter/receiver modules of microwave communication systems, such as radars and EW, without any deterioration of phase noises despite increases in the N divider ratio.

The proposed PLDRO structure enables the free adjustment of output frequencies without any deterioration of phase noise characteristics. Moreover, it enables the phase locking at all frequencies regardless of the precision of the frequency of the internal VCXO.

The proposed PLDRO structure is designed in a way that the output frequency of the DRO is coupled and made to pass the divider. The phase is directly compared at the external reference frequency (10 MHz) in the PLLIC, and the error voltage corresponding to the phase difference is used to control the VT terminal of the VCXO. Therefore, the proposed structure does not cause any phase noise deterioration within the loop filter bandwidth in analog PLL circuits. The measured values of the phase noises at the K-band (19.25 GHz) after multiplying 9.625 GHz by two are –96.5 dBc/Hz and –103.3 dBc/Hz at 1 kHz and 10 kHz offsets frequencies, respectively.

This study paves the way for future studies on areas in which complicated (integer multiple of the reference frequency) output frequencies are required using the general external frequency of 10 MHz without causing phase noise deterioration.

References

[1] X. Gai, G. Liu, S. Chartier, A. Trasser, and H. Schumacher, "A PLL with ultra low phase noise for millimeter wave applications," in *Proceeding of the 40th European Microwave Conference (EuMC)*, Paris, France, 2010, pp. 69–72.

[2] W. I. Chang and C. S. Park, "Implementation of a PLDRO with a fractional multiple frequency of reference," *Progress in Electromagnetics Research Letters*, vol. 46, pp. 13–18, 2014.

[3] A. Lazaro, D. Girbau, P. De Paco, and L. Pradell, "Low cost PLDROs for LMDS/MVDS applications for 40 GHz band," in *Proceedings of the 32nd European Microwave Conference (EuMC)*, Milan, Italy, 2002, pp. 1–4.

[4] *Performance characteristics for intermediate data rate digital carriers using convolutional encoding/Viterbi encoding and QPSK modulation (QPSK/IDR)*, Intelsat Earth Station Standards, IESS-308, 1998.

[5] S. Long, "Phase locked loop circuits," UCSB/ECE Department, 2008 [Online]. Available: http://www.ece.ucsb.edu/Faculty/rodwell/Classes/ece218b/notes/PLL_intro_FMD_FS.pdf.

[6] K. K. Kan, "A 2-V 1.8-GHz fully-integrated CMOS frequency synthesizer for DCS-1800 wireless systems," PhD dissertation, Hong Kong University of Science and Technology, 1999.

[7] B. Razavi, "A study of phase noise in CMOS oscillators," *IEEE Journal of Solid-State Circuit*, vol. 31, no. 3, pp. 331–343, 1996.

[8] A. Brillant, "Understanding phase-locked DRO design aspects," *Microwave Journal*, vol. 42, no. 9, p. 22, 2000.

Yuseok Jeon

obtained his B.S. in electronic communication engineering from Chungju National University, Chungju, Korea, in 2000 and his M.S. in electronic engineering from Chungbuk National University, Cheongju, Korea in 2004. He is currently pursuing his Ph.D. degree in electronic and electric engineering in Dankook University, Yongin, Korea. He worked at Broadern Inc., Hwaseong, Korea, from 1999 to 2017. His research interests include the development of transceivers, receivers, and synthesizers using chip and wire processes for EW and radar system applications.

Sungil Bang

obtained his B.S. in electronic engineering from Dankook University, Seoul, Korea in 1984, his M.S. in electronic engineering at Dankook University, Seoul, Korea in 1986, and his Ph.D. in electronic engineering at Dankook University, Seoul, Korea in 1992. From 1994 to 1997, he worked as the director of the research division at LC Tech Inc., Anyang, Korea. Since 1994, he has been a Professor of Electronic and Electric Engineering at Dankook University, Yongin, Korea. His research interests include RF Amp, UWB, OFDM, and RFID for telecommunication applications.

JOURNAL OF ELECTROMAGNETIC ENGINEERING AND SCIENCE, VOL. 17, NO. 3, 147~152, JUL. 2017

http://dx.doi.org/10.5515/JKIEES.2017.17.3.147
ISSN 2234-8395 (Online) · ISSN 2234-8409 (Print)

A G-Band Frequency Doubler Using a Commercial 150 nm GaAs pHEMT Technology

Iljin Lee[1] · Junghyun Kim[2] · Sanggeun Jeon[1,*]

Abstract

This paper presents a frequency doubler operating at G-band that exceeds the maximum oscillation frequency (f_{max}) of the given transistor technology. A common-source transistor is biased on class-B to obtain sufficient output power at the second harmonic frequency. The input and output impedances are matched to achieve high output power and high return loss. The frequency doubler is fabricated in a commercial 150-nm GaAs pHEMT process and obtains a measured conversion gain of −5.5 dB and a saturated output power of −7.5 dBm at 184 GHz.

Key Words: Frequency Doubler, G-Band, GaAs pHEMT, Harmonic Matching.

I. INTRODUCTION

A signal source is one of the essential circuit blocks used for high-resolution imaging or high-speed wireless communication at mm-wave and terahertz bands. However, designing a fundamental oscillator at such a high frequency remains challenging because of the limitation of transistor speed, which is usually quantified by a maximum oscillation frequency (f_{max}).

Instead of a fundamental oscillator, harmonic oscillators and frequency multipliers [1–4] have been widely used for signal generation at a high frequency that is close to f_{max}. With the advancements in transistor technology, several frequency doublers operating at hundreds of GHz have been reported recently [5–9]. However, they mostly utilize advanced semiconductor processes, which may suffer from high cost and limited accessibility.

In this paper, we implement a G-band frequency doubler using a relatively low-cost commercial 150-nm GaAs pHEMT technology. This technology is not optimum for the doubler design because the transistor f_{max} is only 160 GHz, which is lower than the doubler operation frequency. However, the transistor topology, bias condition, and impedance matching are optimized to obtain sufficient output power at G-band. The proposed frequency doubler demonstrates the feasibility of implementing a low-cost terahertz source based on a less-advanced transistor technology.

II. G-BAND FREQUENCY DOUBLER DESIGN

To determine the optimum structure for the frequency doubler, the second-harmonic output power of three different transistor topologies, namely, common-gate (CG), common-source (CS), and cascode, are compared, as shown in Fig. 1. The input power is fixed to 0 dBm, and no impedance matching is considered in each topology. As frequency increases, the output power of cascode and CS gradually reduces. Specifically, the decrease

Manuscript received April 7, 2017 ; Revised July 7, 2017 ; Accepted July 11, 2017. (ID No. 20170407-017J)
[1]School of Electrical Engineering, Korea University, Seoul, Korea.
[2]Devision of Electronic Engineering, Hanyang University, Ansan, Korea.
[*]Corresponding Author: Sanggeun Jeon (e-mail: sgjeon@korea.ac.kr)

in cascode power is more pronounced because the cascode transistor presents loss rather than gain beyond f_{max} of the transistor. Therefore, the cascode topology is excluded in this G-band frequency doubler.

On the other hand, the output power of CG increases with frequency. At the target frequency of 220 GHz, CG generates a 2.5-dB higher output power than CS. However, it should be noted that no impedance matching is considered in the simulation of Fig. 1. Therefore, determining the optimum topology between CS and CG is not yet straightforward.

For a more practical comparison, the second-harmonic power is re-simulated while the input and output impedances are matched to 50 Ω at 110 and 220 GHz, respectively. As expected, cascode exhibits the lowest output power in Fig. 2. CS and CG generate comparable output power at a low input level. However, the saturated power of CS is considerably higher than that of CG. Although CG can benefit from a better bandwidth than CS because of wider input matching, we still choose the CS topology to obtain higher output power.

A schematic of the G-band frequency doubler is illustrated in Fig. 3. A single-stage CS structure with simple stub matching is employed to minimize the effect of device model inaccuracy at high frequency. The gate width of the transistor is determined as 2 × 25 μm, which yields the highest second-harmonic power at 220 GHz.

The gate bias voltage (V_{gs}) is also selected to maximize the second-harmonic power. Fig. 4 shows the simulated drain current at the fundamental and second-harmonic frequencies versus V_{gs}. The drain bias voltage (V_{ds}) is fixed to 1 V. The second-harmonic current has two peaks at V_{gs} = −1.1 V and −0.2 V. Although showing a higher current at 220 GHz, the peak at V_{gs} = −0.2 V is avoided because of its large DC power consumption and high harmonic generation. Therefore, the other peak at V_{gs} = −1.1 V is chosen. Furthermore, this class-B bias condition brings the advantage of zero DC power consumption when no RF input is applied.

Through a harmonic load-pull simulation, the optimum output impedance yielding the maximum second-harmonic power is obtained. The impedance turns out to be close to the conjugate matching impedance. Therefore, the output is conjugately matched at 220 GHz to achieve high output power and high return loss. The input is also conjugately matched at 110 GHz.

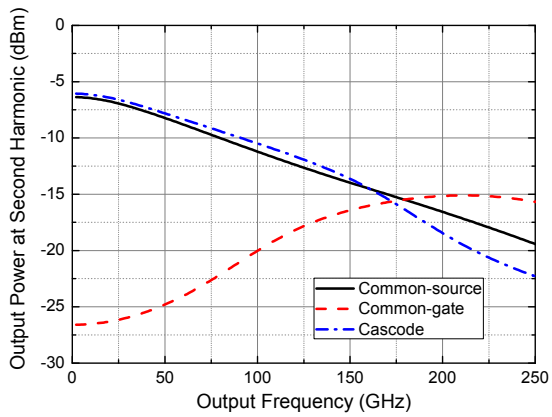

Fig. 1. Comparison of second-harmonic output power among three different transistor topologies at P_{in} = 0 dBm.

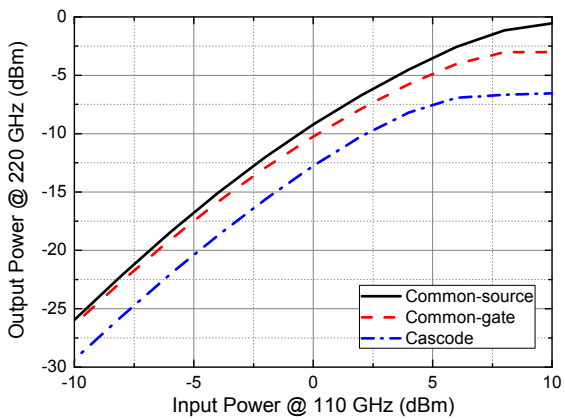

Fig. 2. Comparison of output power at 220 GHz versus input power at 110 GHz among three different transistor topologies.

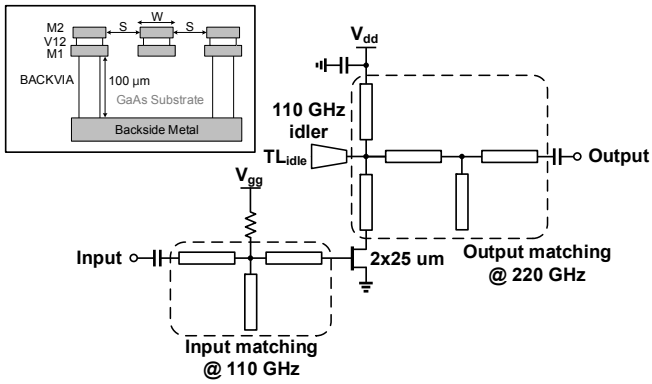

Fig. 3. Schematic of the G-band frequency doubler.

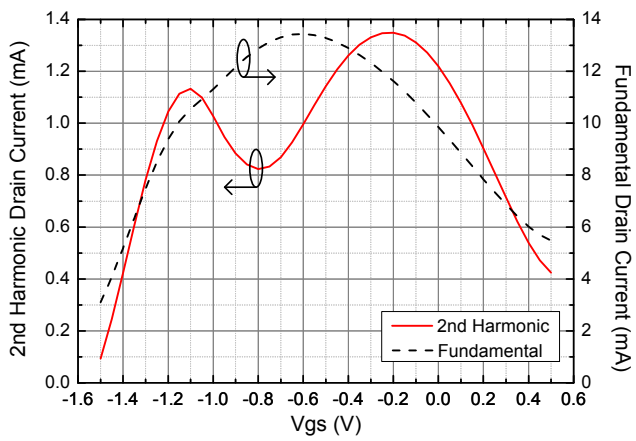

Fig. 4. Simulated drain currents at the fundamental and second-harmonic frequencies versus V_{gs} (V_{ds} = 1 V).

A radial stub is inserted into the output to suppress the fundamental component. The input and output matching network is implemented using a CPW structure, as shown in the inset of Fig. 3. Compared with a microstrip line, CPW benefits from a relatively low radiation loss and a narrow line width. The width (W) and spacing (S) for a 50-Ω characteristic impedance are 15 μm and 10.5 μm, respectively. All CPW lines are simulated using a commercial electromagnetic (EM) simulator (Agilent Momentum).

Fig. 5 shows the simulated port matching performance. The return loss at the input and output is higher than 10 dB at 110 GHz and 220 GHz, respectively. Fig. 6 shows the simulated conversion gain and fundamental suppression versus output frequency when the input power is 2 dBm. The conversion gain is −14.5 dB at 220 GHz, and the fundamental component is suppressed by more than 20 dB at the output.

III. Measurements

The G-band frequency doubler was fabricated in a commercial 150-nm GaAs pHEMT process. The transistor f_{max} is 160

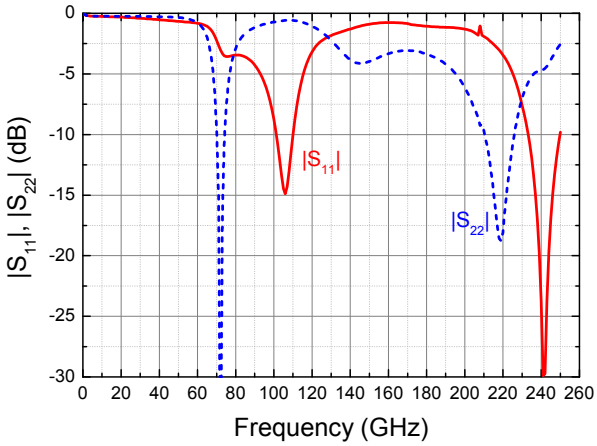

Fig. 5. Simulated input and output matching performance.

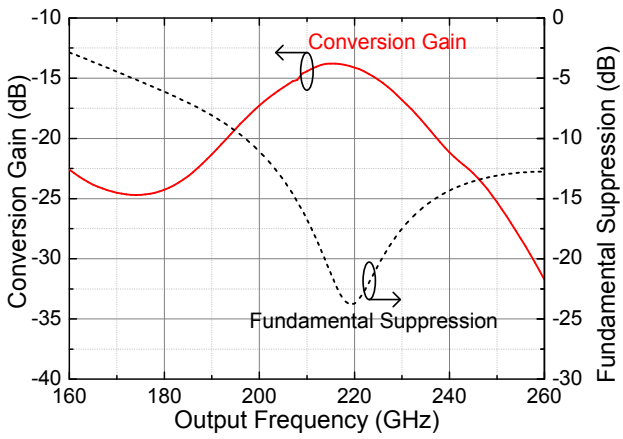

Fig. 6. Simulated conversion gain and fundamental suppression versus output frequency at P_{in} = 2 dBm.

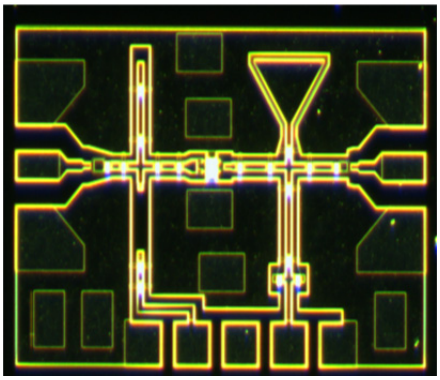

Fig. 7. Chip micrograph of the G-band frequency doubler (1.0 mm × 0.63 mm).

GHz, which is considerably below the operating frequency of the frequency doubler. Fig. 7 shows a chip micrograph, which occupies an area of 1.0 mm × 0.63 mm.

The chip is measured with a waveguide-based on-chip probing setup, as shown in Fig. 8. The input signal is generated by a W-band source module with a built-in variable attenuator. The chip is probed by waveguide probes and sections. The output power is measured with a calorimeter-based power meter. The loss of waveguide probes and sections, as indicated in Fig. 8, are de-embedded in the measurement.

Fig. 9 shows the measured conversion gain versus the output frequency when the input power is −16 dBm. A peak conversion gain of −5.5 dB is measured at 184 GHz. The conversion gain is higher than −7.6 dB from 180 GHz to 196 GHz. Compared to simulation (long-dashed line), the operating frequency is shifted down and the gain increases. This is presumably due to the underestimation of the electrical length of CPW lines. Therefore, we perform additional simulation with extra length considered. The post-simulation result (short-dashed line) becomes closer to the measurement. A residual discrepancy is due to the inaccuracy of the transistor model at the frequency above transistor f_{max}.

Fig. 10 shows the measured output power and conversion

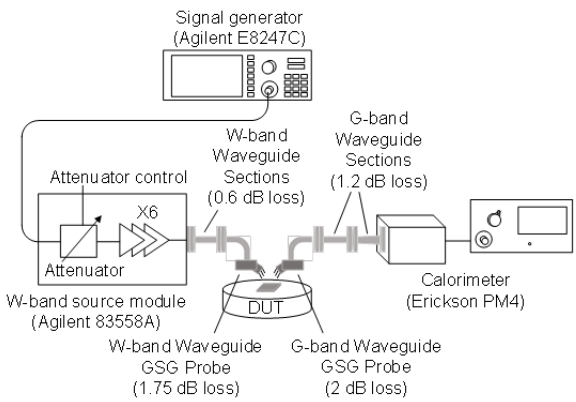

Fig. 8. On-chip power measurement setup for the G-band frequency doubler.

Table 1. Comparison of this work with other millimeter wave frequency multipliers

	This work	[2]	[4]	[5]	[6]	[7]	[8]	[9]
Frequency f_{out} (GHz)	180–196	92.5–96.5	DC–100	150–220	200–235	250–310	138–170	170–190
Conversion gain (dB)	−5.5	-	−3	3	−7	-	4.9	−6.4
Saturated output power (dBm)	−7.5	3	−8	−6	−4	−6.4	5.6	0
Technology	150-nm GaAs pHEMT	100-nm GaAs HEMT	InP DHBT	50-nm GaAs mHEMT	50-nm mHEMT	50-nm mHEMT	130-nm SiGe HBT	45-nm SOI CMOS
f_T, f_{max} (GHz)	85, 160	>100, -	180, 220	-, 380	380, 380	400, 420	300, 500	200, -
f_{out}/f_{max} ratio	1.15	-	0.45	0.47	0.57	0.67	0.31	-

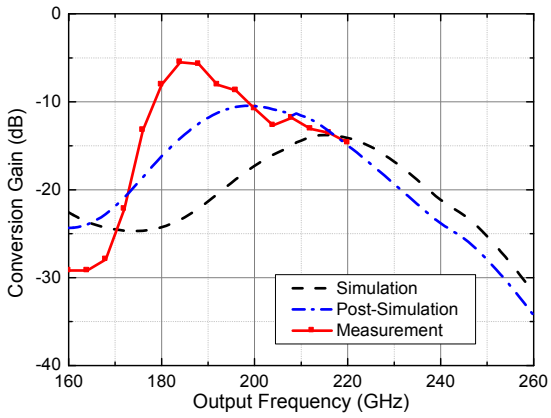

Fig. 9. Measured conversion gain at P_{in} = −16 dBm.

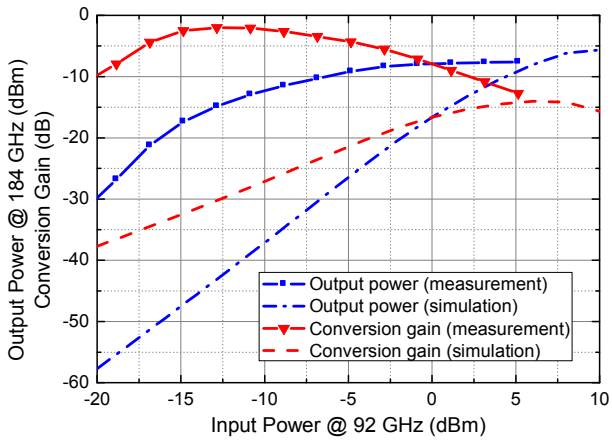

Fig. 10. Measured output power and conversion gain at 184 GHz versus input power.

gain at 184 GHz as the input power increases from −20 dBm to 5 dBm. The maximum output power is −7.5 dBm. The discrepancy between the simulation and measurement is also due to the inaccuracy of the transistor model and EM simulation. The DC drain current flows 2.6 mA at V_{ds} = 1 V when an RF input power of 5 dBm is applied.

The frequency doubler is compared with other reported mm-wave frequency multipliers operating at similar frequencies in Table 1. The saturated output power and conversion gain are comparable with those of other works. However, it should be noted that all other multipliers were fabricated in advanced and (or) research-oriented processes that offer excellent transistor f_{max} above 220 GHz. Conversely, the frequency doubler in this work utilizes a low-cost commercial process offering low transistor f_{max}, even lower than the operating frequency. The ratio of output frequency to transistor f_{max} exceeds unity only in this frequency doubler.

IV. Conclusion

In this paper, a G-band frequency doubler is demonstrated using a commercial 150-nm GaAs pHEMT process offering transistor f_{max} lower than the operating frequency. The measurements show that the conversion gain is −5.5 dB and the saturated output power is −7.5 dBm at 184 GHz. The conversion gain is no lower than −7.6 dB over the frequency from 180 GHz to 196 GHz. The frequency doubler can be used as a low-cost terahertz source for imaging and wireless communication.

This work was supported by the Research Service Program funded by the Korea Astronomy and Space Institute (Deveopment of millimeter wave low noise LNA).

References

[1] Y. Kwon, D. Pavlidis, P. Marsh, M. Tutt, G. I. Ng, and T. Brock, "180 GHz InAlAs/InGaAs HEMT monolithic integrated frequency doubler," in *Proceedings of 13th Annual Gallium Arsenide Integrated Circuit (GaAs IC) Symposium*, Monterey, CA, 1991, pp. 165–168.

[2] H. Wang, K. W. Chang, D. Smith, G. S. Dow, K. L. Tan,

A. K. Oki, and B. R. Allen, "A W-band source module using MMIC's," *IEEE Transactions on Microwave Theory and Techniques*, vol. 43, no. 5, pp. 1010–1016, 1995.

[3] V. Puyal, A. Konczykowska, P. Nouet, S. Bernard, M. Riet, F. Jorge, and J. Godin, "A broad-band active frequency doubler operating up to 120 GHz," in *Proceedings of European Gallium Arsenide and Other Semiconductor Application Symposium (GAAS 2005),* Paris, France, 2005, pp. 557-560.

[4] V. Puyal, A. Konczykowska, P. Nouet, S. Bernard, S. Blayac, F. Jorge, M. Riet, and J. Godin, "DC-100-GHz frequency doublers in InP DHBT technology," *IEEE Transactions on Microwave Theory and Techniques*, vol. 53, no. 4, pp. 1338–1344, 2005.

[5] C. Schworer, Y. C. Roca, A. Leuther, A. Tessmann, M. Seelmann-Eggebert, H. Massler, M. Schlechtweg, and G. Weimann, "A 150 to 220 GHz balanced doubler MMIC using a 50 nm metamorphic HEMT technology," in *Proceedings of European Gallium Arsenide and Other Semiconductor Application Symposium (GAAS 2005)*, 2005, Paris, France, pp. 565–568.

[6] Y. Campos-Roca, C. Schworer, A. Leuther, and M. Seelmann-Eggebert, "G-band metamorphic HEMT-based frequency multipliers," *IEEE Transactions on Microwave Theory and Techniques*, vol. 54, no. 7, pp. 2983–2992, 2006.

[7] I. Kallfass, A. Tessmann, H. Massler, D. Lopez-Diaz, A. Leuther, M. Schlechtweg and O. Ambacher, "A 300 GHz active frequency-doubler and integrated resistive mixer MMIC," in *Proceedings of European Microwave Integrated Circuits Conference (EuMIC 2009)*, Rome, Italy, 2009, pp. 200–203.

[8] C. Coen, S. Zeinolabedinzadeh, M. Kaynak, B. Tillack, and J. D. Cressler, "A highly-efficient 138–170 GHz SiGe HBT frequency doubler for power-constrained applications," in *Proceedings of 2016 IEEE Radio Frequency Integrated Circuits Symposium (RFIC)*, San Francisco, CA, 2016, pp. 23–26.

[9] B. Cetinoneri, Y. A. Atesal, A. Fung, and G. M. Rebeiz, "W-Band amplifiers with 6-dB noise figure and milliwattlevel 170–200-GHz doublers in 45-nm CMOS," *IEEE Transactions on Microwave Theory and Techniques*, vol. 60, no. 3, pp. 692–701, 2012.

Iljin Lee

(S'14) received the B.S. degree from the School of Electrical Engineering, Korea University Seoul, Korea, in 2013, and is currently working toward the Ph.D. degree at the School of Electrical Engineering Korea University, Seoul, Korea. His primary research interests are millimeter-wave and terahertz integrated circuits and systems for broadband communication applications.

Junghyun Kim

(S'99–M'05) was born in Busan, Korea. He received his Ph.D. degree in electrical engineering from Seoul National University, Seoul, Korea, in 2005. In 2000, he joined, as a Student Co-Founder, WavICs, a power amplifier design company which is now fully owned by Broadcom, where he invented the switchless stage-bypass power amplifier architecture called CoolPAM. From 2005 to 2007, he was with Wireless Semiconductor Division, Avago Technologies, as a Group Manager of Integrated Circuit (IC) Design Group. In 2007, he joined the faculty of the Department of Electronic System Engineering, Hanyang University, Ansan, Korea, where he is currently an Associate Professor. Since 2013, he has also been an External Director with Broadcom. He holds more than 40 US patents on power-amplifier technology and RF integrated circuits (RFICs). His current research activities include monolithic microwave integrated circuit (MMIC) design for mobile communication and millimeter-wave systems, the thermal packaging analysis of high power device, and intermodulation and noise analysis of nonlinear circuits.

Sanggeun Jeon

(S'05–M'06) received the B.S. and M.S. degrees in electrical engineering from the Seoul National University, Seoul, Korea, in 1997 and 1999, respectively, and the M.S. and Ph.D. degrees in electrical engineering from the California Institute of Technology, Pasadena, CA, USA, in 2004 and 2006, respectively. From 1999 to 2002, he was a Full-Time Instructor of electronics engineering at the Korea Air Force Academy. From 2006 to 2008, he was a Research Engineer in the High-speed Integrated Circuits Group, California Institute of Technology, in which he worked on CMOS phased-array receiver design. Since 2008, he has been with the School of Electrical Engineering, Korea University, Seoul, Korea, where he is currently a Professor. His research interests include integrated circuits and systems at microwave, millimeter-wave, and terahertz bands for high-speed wireless communication and high-resolution imaging applications.

JOURNAL OF ELECTROMAGNETIC ENGINEERING AND SCIENCE, VOL. 17, NO. 3, 153~158, JUL. 2017

http://dx.doi.org/10.5515/JKIEES.2017.17.3.153
ISSN 2234-8395 (Online) · ISSN 2234-8409 (Print)

Effect of Plasma Area on Frequency of Monostatic Radar Cross Section Reduction

Jungje Ha[1] · Woongjae Shin[1] · Joo Hwan Lee[1] · Yuna Kim[1] · Doosoo Kim[2] · Yongshik Lee[1,*] · Jong-Gwan Yook[1]

Abstract

This work reports on the effect of plasma area on the frequency characteristics of the monostatic radar cross section (RCS) of a square metallic plate. A dielectric barrier discharge (DBD) plasma actuator consisting of 10 rings is proposed. The actuator is fabricated in three different configurations such that only three inner rings, seven inner rings, and all rings can be biased. By applying an 18-kV bias at 1 kHz, the three types of DBD actuators generate plasma with a total area of 16.96, 36.74, and 53.69 cm^2, respectively, in a ring or circular form. The experimental results reveal that when the DBD actuator is placed in front of a 20 mm × 20 cm conducting plate, the monostatic RCS is reduced by as much as 18.5 dB in the range of 9.41–11.65 GHz. Furthermore, by generating the plasma and changing the area, the frequency of maximum reduction in the monostatic RCS of the plate can be controlled. The frequency is reduced by nearly 20% in the X band when all rings are biased. Finally, an electromagnetic model of the plasma is obtained by comparing the experimental and full-wave simulated results.

Key Words: Dielectric-Barrier-Discharge Plasma, Frequency Tunable, Radar Cross Section Reduction, Surface Area of Plasma.

I. INTRODUCTION

On the battlefield, efficient surveillance radars use high-gain beams to obtain target information such as location and velocity. To counter the development of such radars, various stealth technologies have been developed to increase the survivability of weapon systems [1–3].

Electromagnetic stealth technology aims to reduce a target's radar cross section (RCS); the RCS describes how much electromagnetic power is scattered by the target. The most important factors that affect an object's RCS are its size, shape, and material. Thus, engineers have been developing planes with specific shapes that can redirect electromagnetic waves from radars. For instance, the shape of the F-117 is optimized to minimize the amount of radar signals reflected back to the emitting radar [4]. However, stealth shaping techniques may have a limited effect because aerodynamic properties cannot be sacrificed.

Other popular methods for RCS reduction are radar-absorbing materials (RAM) and radar-absorbing structures (RAS) [5–8]. In these methods, lossy radar-absorbing materials are used to reduce the reflection of incident electromagnetic waves from the aircraft. However, these methods suffer from problems such as narrow band performance, high weight, and high fabrication and maintenance costs.

Recently, researchers have been investigating plasma technol-

Manuscript received June 26, 2017 ; Revised July 22, 2017 ; Accepted July 24, 2017. (ID No. 20170626-027J)
[1]Department of Electrical and Electronic Engineering, Yonsei University, Seoul, Korea.
[2]Agency for Defense Development, Daejeon, Korea.
[*]Corresponding Author: Yongshik Lee (e-mail: yongshik.lee@yonsei.ac.kr)

ogy as an alternative stealth method [9]; for example, one study investigated refraction, reflection, and absorption based on plasma surrounding a 2D cylinder. Popular methods for generating plasma include dielectric barrier discharge (DBD), plasma torch, and plasma jet [10]. Although all plasma-generating methods can be used to realize the low-observable characteristic, DBD is better than other plasma sources because it has the simplest structure and its size can be adjusted easily.

This work reports on the effect of plasma area on the frequency characteristics of the monostatic RCS of a square metallic plate. A DBD plasma actuator consisting of 10 rings is modified into three different configurations that have different plasma areas with connections of multiple electrodes. In this work, the three types of DBD actuators with different plasma areas are used by applying 18 kV bias at 1 kHz. For verification, the RCS is measured for the fabricated DBD in front of a 20-cm square metal plate. The experimental results reveal that the generated plasma area can be controlled to reduce the RCS, and also adjust the frequency of maximum reduction in the monostatic RCS of the plate. Furthermore, an electromagnetic model of the plasma is obtained by comparing the experimental and full-wave simulated results.

II. Proposed DBD Plasma Actuator and Electromagnetic Modeling of Plasma

Fig. 1 shows the proposed DBD plasma actuator. The actuator consists of concentric ring-shaped electrodes printed on both sides of a 200 mm × 200 mm FR-4 substrate with $\epsilon_r = 4.4$, $\tan\delta = 0.025$, 0.8-mm thickness, and 35-μm copper cladding. Ten rings are on the top layer and nine, on the other side. The outer radius of the largest ring is 88.5 mm, and the inner radius of the smallest ring is 15.5 mm. The gap between two adjacent rings is $d = 3$ mm.

To generate plasma, an AC source is applied between the top and the bottom electrodes with a voltage that is higher than the breakdown voltage of the environment. The minimum breakdown voltage is described by Paschen's law [11, 12]:

$$V_b = \frac{B \times pd}{C + \ln(pd)} \tag{1}$$

where B and C are constants determined by the type of environmental gases, and p and d denote the pressure and distance between electrodes, respectively. In the atmosphere, the constants are $B = 365\ \mathrm{V \cdot cm^{-1} \cdot Torr^{-1}}$ and $C = 1.18$ [10, 11]. From Eq. (1), the calculated minimum breakdown voltage is 8.9 kV. Based on the result, 18 kV is used for the stable generation of stable plasma, that is, glow discharge. Moreover, to prevent arc discharge between the plasma actuator and the nearby metallic object, namely, the copper plate, the two are separated by $g = 2.0$ mm.

Fig. 2 shows the measurement setup for the monostatic RCS of the 200 × 200 mm² square copper plate with the DBD actuator placed in front. An acrylic jig is used for accurate placement of the actuator and the copper target. The RCS measurement is performed in the 4–18 GHz range by using a pair of DRH-002G-018G double-ridged horn antennas and a 37247D vector network analyzer from Anritsu. Because the fabricated actuator comprises ring-shaped electrodes, the scattering characteristic is independent of the polarization of incident waves. In this work, only the incidence of a vertical-polarized wave is considered.

Fig. 3 shows the measured RCS for the fabricated DBD actuator in front of a 200 × 200 mm² copper plate with and

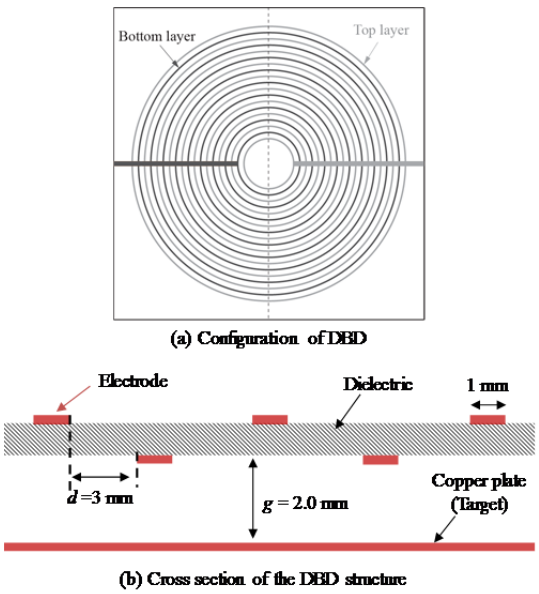

Fig. 1. Configuration of fabricated DBD plasma actuator.

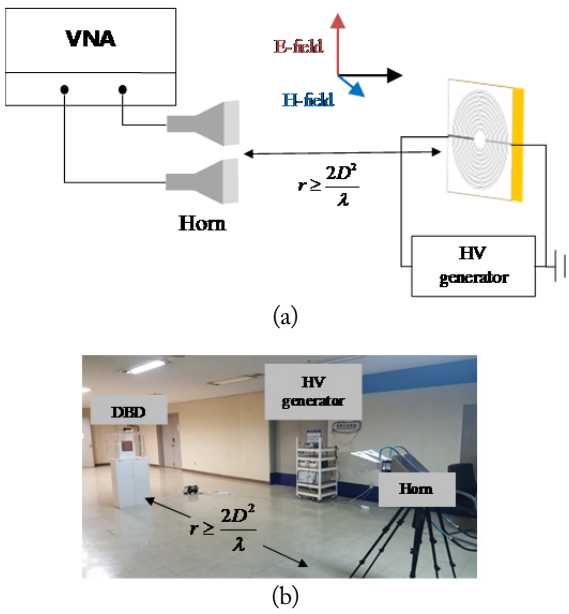

Fig. 2. Monostatic RCS measurement setup: (a) diagram, (b) photograph.

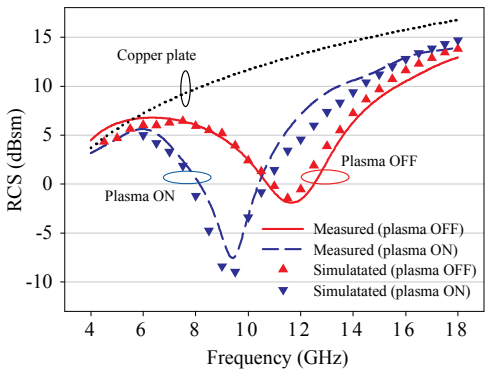

Fig. 3. Measured monostatic RCS of 200 mm × 200 mm copper plate with and without DBD actuator in front.

without plasma generation. Compared to both measured results, frequency shift can be achieved by plasma generation.

To obtain the equivalent model of the generated plasma, the electrical properties of the generated plasma are required. These can be derived from the dispersion relation of a wave in plasma. According to [12], this relation can be expressed as

$$k = \sqrt{\frac{\omega^2}{c^2} - \frac{\omega_p^2}{c^2\left(1 - j\frac{\nu}{\omega}\right)}} \tag{2}$$

where k is a complex wavenumber; ω, the operating angular frequency; c, the speed of light; ν, the electron-neutral collision frequency; and ω_p, the plasma angular frequency, which can be calculated as follows [13]:

$$\omega_p = \sqrt{\frac{n_e e^2}{m_e \epsilon_0}} \cong 8\sqrt{n_e} \tag{3}$$

where n_e is the electron density; e, the charge of an electron; m_e, the electron mass; and ϵ_0, the permittivity of free space. From Eq. (1), the effective permittivity of the plasma can be derived as

$$\epsilon = \epsilon_0 \left\{1 - \frac{\omega_p^2/\omega^2}{1 + \nu^2/\omega^2} - j\left(\frac{\nu}{\omega}\right)\left(\frac{\omega_p^2/\omega^2}{1 + \nu^2/\omega^2}\right)\right\} \tag{4}$$

Generally, the electron density at atmospheric pressure is $n_e = 10^{20}$–10^{21} m^{-3} [14]; then, the plasma frequency becomes 12.6–40.2 GHz. If ν/ω is small enough to be ignored, the effective permittivity of the plasma becomes an epsilon-negative medium, which provides electromagnetic characteristics similar to those of metals such as silver or gold [15]. In this work, the generated plasma is assumed to be a material with high conductivity ($\sigma \geq 1{,}000$).

In addition to the electromagnetic material characteristic, the geometric structure of the generated plasma is required. Fig. 4 shows the modelled structure of the generated plasma. The effective width W_{pi} and thickness T_{pi} of the generated plasma around the ith ring are assumed to be inversely proportional to the radius of the ith electrode ring. It is assumed that each ring

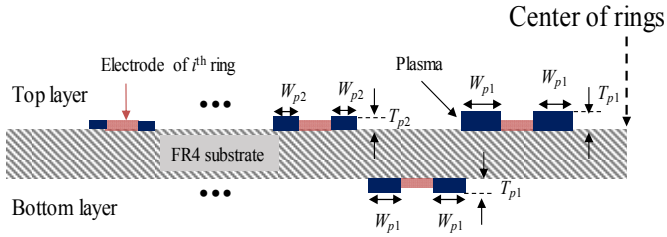

Fig. 4. Geometrically modelled structure of generated plasma.

Table 1. Physically modelled parameters for generated plasma

i^{th} ring	Top layer		Bottom layer	
	$W_{p,i}$ (μm)	$T_{p,i}$ (μm)	$W_{p,i}$ (μm)	$T_{p,i}$ (μm)
1st	1,406	2,344	1,125	1,875
2nd	937	1,563	803	1,339
3rd	703	1,172	625	1,042
4th	562	937	511	852
5th	468	781	432	721
6th	402	669	375	625
7th	351	586	331	551
8th	312	521	296	493
9th	281	469	268	446
10th	255	426	-	-

generates the same volume of plasma. By using a commercial software (ANSYS High Frequency Structure Simulator v10.0), the EM simulation is optimized; the physically modelled parameters for the generated plasma are summarized in Table 1.

The full-wave simulated RCS of the modeled plasma is plotted with the measured RCS in Fig. 3. Both results are in good agreement. Therefore, the simulated results indicate that plasma generation changes the scattering characteristic of an object by working as a high-conductivity material. These phenomena can also be observed in the ionosphere, where electromagnetic waves of 3–30 MHz are reflected [16].

III. Effect of Plasma Area on Frequency of Monostatic RCS Reduction

As mentioned in the previous section, the generated plasma changes the scattering characteristic of the metal plate. In other words, different forms of generated plasma result in different scattering performances. Therefore, in this work, the minimum RCS frequency can be tuned by adjusting the area of the generated plasma. This can be achieved by switching the AC voltage between multiple rings. For verification, three cases are considered. In Type I, the DBD plasma actuator is constructed by connecting three inner rings on each side; Type II comprises seven inner rings on top and six rings on the other side; and Type III comprises all-connected rings on each side. Fig. 5 shows photographs of the different areas with the application of a high voltage of 18 kV.

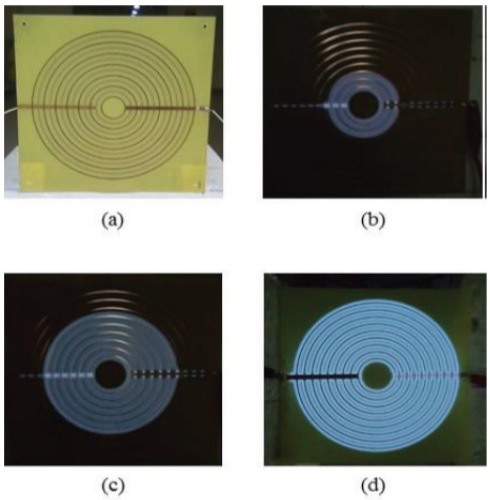

Fig. 5. Photographs of different models. (a) Plasma off, (b) Type I, (c) Type II, and (d) Type III.

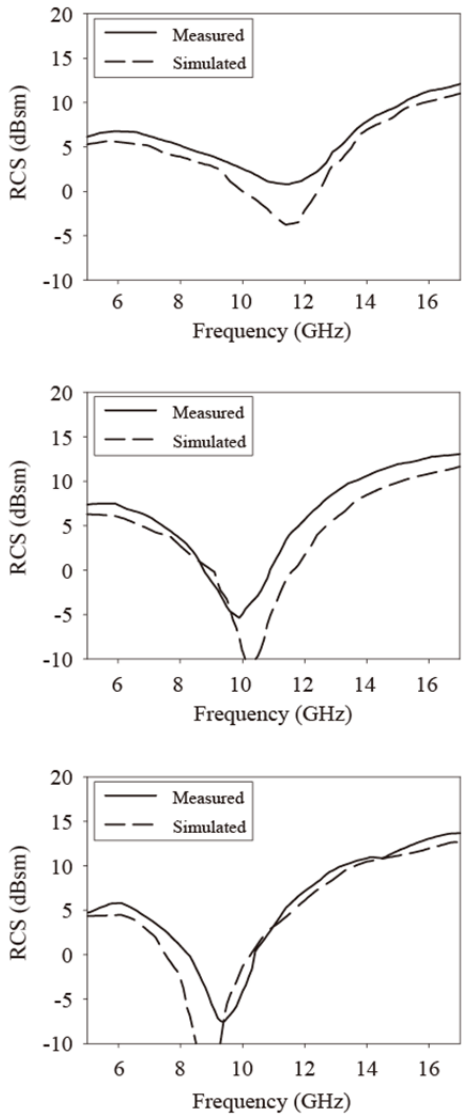

Fig. 6. Comparison with measurement results for all cases to shift monostatic RCS reduction frequency.

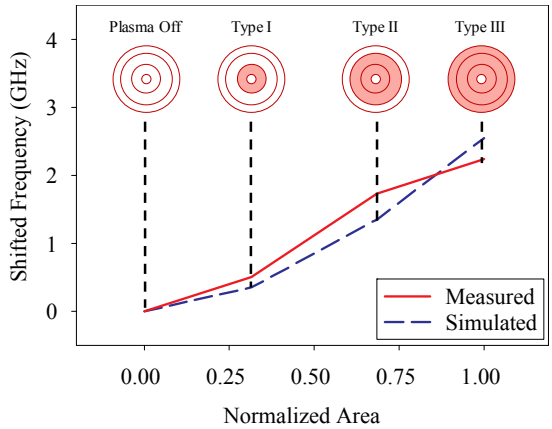

Fig. 7. Frequency shift with respect to normalized plasma area.

Fig. 6 shows the results of experiments with various areas of generated plasma. Although the measurement is conducted in a laboratory environment and not an anechoic chamber, we used time gating to neglect undesired waves reflected by the other obstacles; therefore, the measurement results are in good agreement with the simulation results, as shown in Fig. 6.

Fig. 6 shows that the frequency for minimum RCS is 11.65 GHz for the plasma off state. When applying a high voltage to the electrodes, the lowest RCS frequency becomes 11.25, 9.92, and 9.41 GHz for Types I, II, and III, respectively. Fig. 7 shows the amount of measured and simulated frequency shift depending on the generated plasma area. The amount of frequency shift increases with the plasma area, as shown in this figure.

IV. Conclusion

This work reports on the frequency effect of plasma area for monostatic RCS. To confirm the effect of plasma area, three types of DBD actuators are fabricated. The plasma areas are adjusted by the number of connected electrodes. For verification, the RCS of the fabricated DBD are simulated and measured. As a result, with an increase in the generated plasma area, the RCS is reduced as much as 18.5 dB and the frequency for minimum monostatic RCS changes from 11.65 to 9.41 GHz. Unlike plasma generated by previous DBD plasma actuators, the plasma generated in this work operates as a scattering material rather than an absorbing material. This phenomenon has not been observed in the microwave frequency regime. Therefore, future research could analyze the propagation characteristic in plasma. This can be extended to a very large structure by arranging the proposed DBD periodically.

This work was supported by the Low Observable Technology Research Center program of the Defense Acquisition Program Administration and Agency for Defense Development.

References

[1] Y. Sui, H. Gu, and C. Yang, "Reconfigurable stealth radome using active frequency selective surface technology," in *Proceedings of 2017 IEEE International Conference on Computational Electromagnetics (ICCEM)*, Kumamoto, Japan, 2017, pp. 273-275.

[2] J. Pinto, J. C. G. Matthews, and G. C. Sarno, "Stealth technology for wind turbines," *IET Radar, Sonar and Navigation*, vol. 4, no. 1, pp. 126-133, 2010.

[3] Y. C. Hou, W. J. Liao, C. C. Tsai, and S. H. Chen, "Planar multilayer structure for broadband broad-angle RCS reduction," *IEEE Transactions on Antennas and Propagation*, vol. 64, no. 5, pp. 1859-1866, 2016.

[4] J. Pike, "F-117A Nighthawk," 2016; https://fas.org/man/dod-101/sys/ac/f-117.htm.

[5] I. G. Lee, S. H. Yoon, J. S. Lee, and I. P. Hong, "Design of wideband radar absorbing material with improved optical transmittance by using printed metal-mesh," *Electronics Letters*, vol. 52, no. 7, pp. 555-557, 2016.

[6] Y. Zhao, J. Liu, Z. Song, and X. Xi, "Microstructure design method for multineedle Whisker radar absorbing material," *IEEE Antennas and Wireless Propagation Letters*, vol. 15, pp. 1163-1166, 2016.

[7] H. Singh and R. M. Jha, *Active Radar Cross Section Reduction: Theory and Applications*. Delhi: Cambridge University Press, 2015.

[8] J. Lee and B. Lee, "Design of thin RC absorbers using a silver nanowire resistive screen," *Journal of Electromagnetic Engineering and Science*, vol. 16, no. 2, pp. 106-111, 2016.

[9] L. X. Ma, H. Zhang, Z. Li, and C. X. Zhang, "Analysis on the stealth characteristic of two dimensional cylinder plasma envelopes," *Progress in Electromagnetics Research Letters*, vol. 13, pp. 83-92, 2010.

[10] A. Schutze, J. Y. Jeong, S. E. Babayan, J. Park, G. S. Selwyn, and R. F. Hicks, "The atmospheric-pressure plasma jet: a review and comparison to other plasma sources," *IEEE Transactions on Plasma Science*, vol. 26, no. 6, pp. 1685-1694, 1988.

[11] G. G. Raju and R. Hackam, "Note on Paschen law and the similarity theorem at the minimum breakdown voltage," *IEEE Transactions on Plasma Science*, vol. 2, no. 2, pp. 63-66, 1974.

[12] A. A. Fridman and L. A. Kennedy, *Plasma Physics and Engineering.* Boca Raton, FL: CRC Press, 2004.

[13] D. K. Cheng, *Field and Wave Electromagnetics*, 2nd ed. Reading, MA: Addison-Wesley, 1989.

[14] L. Wei, S. Ying, and Q. Jinghui, "Experimental research on electromagnetic wave attenuation in plasma," in *Proceedings of the International Symposium on Antennas & Propagation (ISAP)*, Nanjing, China, 2013, pp. 1072-1074.

[15] N. Engheta and R. W. Ziolkowski, *Metamaterials: Physics and Engineering Explorations*, New York, NY: John Wiley & Sons, 2006.

[16] P. A. Fialer, "Field-aligned scattering from a heated region of the ionosphere: observations at HF and VHF," *Radio Science*, vol. 9, no. 11, pp. 923-940, 1974.

Jungje Ha

was born in Jinju, Gyeongnam, Korea, in 1985. He received the B.S., M.S., and Ph.D. degrees in Electrical Engineering from Yonsei University, Seoul, Korea, in 2009, 2011, and 2017, respectively. He received a Gold Award in the 2012 Qualcomm-Yonsei Innovation Award and the Grand Prize in the 2015 Creative Design Competition for Future Radio Wave. His current research interests include multiband planar circuits for microwave applications.

Woongjae Shin

was born in Seoul, Korea, in 1990. He received the B.S. and M.S. degrees in Electrical and Electronic Engineering from Chung-Ang University and Yonsei University, Seoul, Korea, in 2015 and 2017, respectively. His current research interests include low-observable applications based on plasma.

Joo Hwan Lee

was born in Seoul, Korea, in 1991. He received the B.S. degree in Information and Communication Engineering from Sejong University, Seoul, Korea, in 2016, and is currently working toward the M.S. degree in Electrical and Electronic Engineering at Yonsei University. His current research interests include low-observable applications based on plasma.

Yunna Kim

was born in Jinju, Korea, in 1988. She received the B.S. degree in Electrical and Electronic Engineering from Yonsei University, Seoul, Korea, in 2012, and is currently working toward the Ph.D. degree in Electrical and Electronic Engineering at Yonsei University. Her current research interest is analysis based on multi-physics including thermodynamics and electromagnetics. Recent research has focused on electric problems caused by high temperatures in circuit.

Doosoo Kim

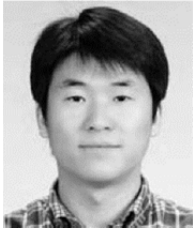

was born in Gwangju, Korea. He received the B.S. degree from Sogang University, Seoul, Korea, in 2001, and the M.S. degree in Electrical and Electronic Engineering from Postech, Pohang, Korea, in 2006. Currently, he works for the Agency for Defense Development (ADD), Daejeon, Korea, as a senior researcher. His current research interests include active phased array antenna systems and optimization algorithms.

Yongshik Lee

was born in Seoul, Korea. He received the B.S. degree from Yonsei University, Seoul, Korea, in 1998, and the M.S. and Ph.D. degrees in Electrical Engineering from the University of Michigan at Ann Arbor in 2001 and 2004, respectively. In 2004, he was a postdoctoral research associate at Purdue University, West Lafayette, IN, USA. From 2004 to 2005, he was with EMAG Technologies, Inc., Ann Arbor, MI, USA as a Research Engineer. In September 2005, he joined Yonsei University, Seoul, Korea, where he is currently an Associate Professor. His current research interests include passive and active circuitry for microwave and millimeter-wave applications and electromagnetic metamaterials.

Jong-Gwan Yook

was born in Seoul, South Korea. He received the B.S. and M.S. degrees in Electronics Engineering from Yonsei University, Seoul, South Korea, in 1987 and 1989, respectively, and the Ph.D. degree from the University of Michigan, Ann Arbor, MI, USA, in 1996. Currently, he is a Professor with the School of Electrical and Electronic Engineering, Yonsei University, Seoul, South Korea. His main research interests are in the areas of theoretical/numerical electromagnetic modeling and characterization of microwave/millimeter-wave circuits and components, design of radio frequency integrated circuits and monolithic microwave integrated circuits, and analysis and optimization of high-frequency high-speed interconnects, including signal/power integrity, based on frequency as well as time-domain full-wave methods. Recently, his research team developed various biosensors, such as carbon nanotube RF biosensors for nanometer-sized antigen-antibody detection as well as remote wireless vital signal monitoring sensors.

JOURNAL OF ELECTROMAGNETIC ENGINEERING AND SCIENCE, VOL. 17, NO. 3, 159~164, JUL. 2017

http://dx.doi.org/10.5515/JKIEES.2017.17.3.159
ISSN 2234-8395 (Online) · ISSN 2234-8409 (Print)

Fully Printed Chipless RFID Tags Using Dipole Array Structures with Enhanced Reading Ranges

Dongho Jeon · Min-Sik Kim · Seung-Jin Ryu · Dae-Heon Lee · Jong-Kyu Kim*

Abstract

This article proposes a design of chipless RFID tag with dipole array structure that is fully printable using conductive ink. The proposed tags encode data based on spectral signature modulations. The reading range is considerably increased (2 m) while maintaining low transmission power (1 mW). Several prototype chipless RFID tags were fabricated and measured in the SHF and UHF bands. The proposed dipole array structure enhances the antenna gain of the passive tags and contributes to overcoming the low conductivity of conductive ink. In order to verify the utility of our proposal, the tags are manufactured on paper, using conductive ink, for the purpose of economic mass production.

Key Words: Chipless RFID Tags, Conductive Ink, Dipole Array Structure, Screen Printing.

I. INTRODUCTION

Since Cardullo and Parks [1] introduced RFID supporting passive radio transponders with memory in the early 1970s, a number of research studies have been conducted. The RFID system without an IC chip, so-called chipless RFID, is suggested as a substitute for the barcode system. Chipless RFID tags are classified into three types depending on the modulation mechanisms, such as time, frequency, or phase [2]. Among the three types, RFID tags using spectral signature modulation is considered to be a good candidate for the upcoming market due to its encoding capacity. Early versions of spectral signatures were realized on microstrip substrate using copper.

Jalaly and Robertson [3] introduced the RF barcode using multiple dipole antennas. Each element resonates at different frequencies depending on their width and gap capacitance. Multi-resonator based chipless RFID tags, which support up to 35 bits of encoding capacity, were presented [4, 5]. They used multi-resonating circuits with 35 spiral resonators and two cross-polarized antennas. However, most previous models have not achieved the goal of chipless RFID tags because of their bulky size and high cost.

In recent years, rapid advancements in materials have led RFID tags to be printed on paper using conductive ink [6-10]. This type of fabrication has remarkably lowered the cost and size of RFID tags, but the low conductivity issue remains as a drawback. Preradovic and Menicanin [11] presented a fully printable 3D stacked chipless RFID tag. Multiple dipole elements were printed on 5 μm polyimide film with conductive ink. The cross-polarization expanded the data capacity to 8 bits. However, the reading range was relatively short (less than 20 cm) due to low conductivity.

In this paper, we present novel, fully printable chipless RFID tags based on dipole array structures. The tags encode data by using spectral signature modulation. The reading range of the proposed dipole array structure is greatly enhanced by the tags'

Manuscript received June 30, 2017 ; Revised July 25, 2017 ; Accepted July 25, 2017. (ID No. 20170630-028J)
National Security Research Institute, Daejeon, Korea.
*Corresponding Author: Jong-Kyu Kim (e-mail: contai@nsr.re.kr)

increased antenna gain. The tags are screen-printed onto plain paper using conductive ink. In addition, it will be shown that tags can be designed at any desired frequency within the UHF and SHF bands. The effect of the proposed chipless RFID tags is also discussed in terms of RFID tag types, number of elements, reading ranges, and so on.

II. Design of Chipless RFID Tags

Two different types of chipless RFID tags are depicted in Figs. 1 and 2, respectively, and are differentiated according to the number of operating frequencies they support.

The geometry shown in Fig. 1 supports a single frequency. The tag is composed of a number of identical elements. The length of the dipole antenna, l, is determined by the operating frequency, which is about a half-wavelength. Here, g represents the distance between dipole elements, which is also about a half-wavelength; w represents the line width of the dipole element. The dipole elements are arranged in the form of an $m \times n$ array where m and n denote the number of array elements in rows and columns, respectively. The design shown in Fig. 2, which is composed of different lengths of dipoles, supports multi-frequencies. The dipole set with a length of l_1, l_2, $\cdots$, l_N is considered to be one element, so a 2×1 array is formed in Fig. 2. The dipoles resonate at different frequencies by interacting with their pair antennas, which are located a half-wavelength ($\lambda_1/2$, $\lambda_2/2$, $\cdots$, $\lambda_N/2$) away from each other. This structure is better suited to the UHF band due to the available space between the array pairs. Two suggested structures are designed based on a half-wavelength antenna array. A number of studies have shown, through theoretical and experimental results, that the array structure improves antenna gain [12, 13].

The operating principle of the proposed RFID tags is simply based on presence and absence states [11]. When tags are located between two reader antennas, they contribute to a strong stopband. Encoding 0 or 1 can be easily determined by distinguishing their presence or absence. Fig. 3 shows several types of the fabricated RFID tags: Fig. 3(a)-(c) show the RFID tags supporting single frequency. Fig. 3(d) shows the multi-frequency RF tag operating between 2.5 and 4 GHz, which supports 3 bits of encoding capacity. The specific dimensions of the tags are given in Table 1.

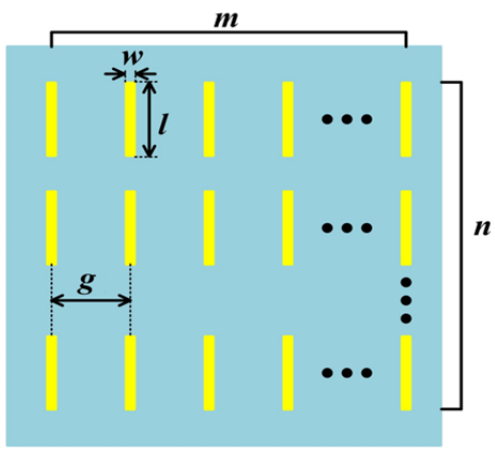

Fig. 1. Design for single-frequency dipole array structure.

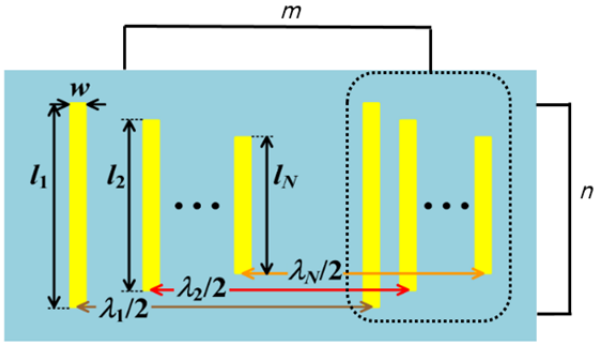

Fig. 2. Design for multi-frequency dipole array structure.

III. Printing Chipless RFID Tags on Paper

For the fabrication, we chose Silveray-RM conductive ink, which is formulated for printed electronics applications, such as RFID and membrane switches. The ink contains 55%–66% silver paste that provides 5–10 μm of thickness. The curable temperature is 150℃ and the time is less than 30 minutes. The average resistance of the ink is 23.01 mΩ/□. Its conductivity is approximately 6%–7% compared to that of copper. The thickness of a single sheet for a fabricated RFID tag on paper is about 110 μm.

A partial microscopic view of the fabricated RFID tag is shown in Fig. 4. It is obvious that the conductivity of printed

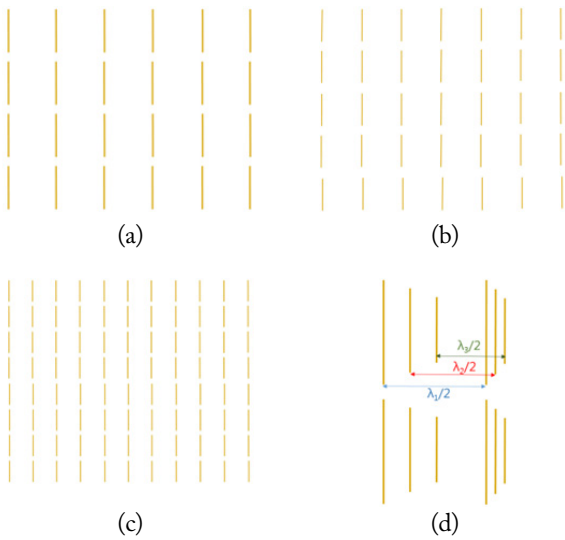

Fig. 3. Fabricated chipless RFID tags. (a) RFID tag at 8.7 GHz (A-4), (b) RFID tag at 10 GHz (B-3), (c) RFID tag at 14 GHz (C-1), and (d) RFID tag at 2.5/3/4 GHz (D).

lines is lower than that of a metal-based medium, since the small particles of conductive ink are not homogeneous. Therefore, the proposed array structure can be more advantageous for overcoming the innate limitation of conductive ink.

Paper has a number of advantages as a substrate. Firstly, it is cost-effective and therefore well suited to mass production. Secondly, it supports inkjet-, screen-, and reel-to-reel printing techniques. We chose the screen-printing method to demonstrate that it is a good candidate for mass production. Moreover, unlike chemical substrates such as FR-4 and PET films, paper is an environmentally benign material: it is not harmful, and it decomposes easily. However, the electrical characteristics of paper should be considered before designing RFID tags on it. Previous studies [14-16] have already shown that paper has appropriate electrical properties as a substrate for UHF and SHF frequency bands.

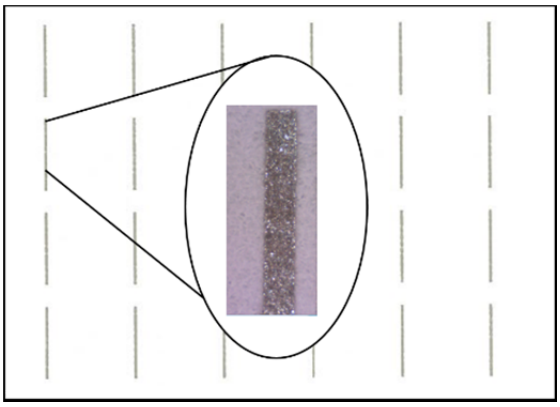

Fig. 4. Microscopic view of RFID tag (A-4).

IV. Experimental Results

Various measurements were made to validate the proposed chipless RFID system. Fig. 5 illustrates the measurement setup. Two vertically polarized horn antennas are placed bi-statically at a distance of d within an anechoic chamber. The horn antenna (LB-7180) covers 0.7–18 GHz and has gain of 12 dBi. A vector network analyzer (N5230A) is used; the Tx power is set to 0 dBm and is employed in all experiments. The chipless RFID tags under test are placed at the center, between two horn antennas.

Fig. 6 shows simulated and measured S_{21} values for various combinations of RFID tags. The distance d is fixed at 1 m. In order to realize the 3 bits of data, we used three prototypes (A-1, B-1, and C-1) corresponding to Table 1. The total thickness of tags under test is approximately 330 μm. The '111' coding case in Fig. 6 shows that the simulated and measured results are in

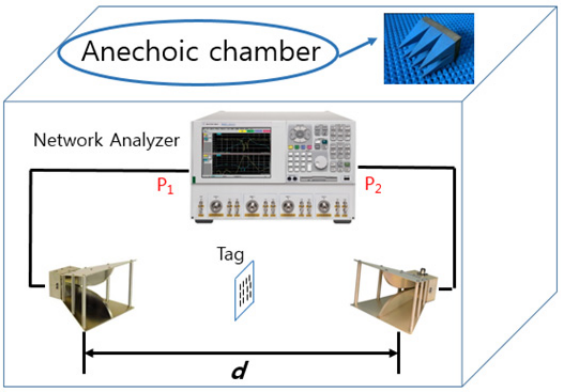

Fig. 5. Diagram of measurement setup.

Table 1. Dimensions of fabricated chipless RFID tags

Type	f (GHz)	l (mm)	g (mm)	ω (mm)	$m \times n$ (array)	Total size (cm^2)
(A-1)	8.7	15	18	0.5	11 × 8	20 × 14
(A-2)					9 × 6	16 × 10.8
(A-3)					7 × 5	14 × 9.0
(A-4)					6 × 4	10 × 6.9
(B-1)	10.5	13	14	0.5	11 × 8	14 × 11.7
(B-2)					9 × 6	11.2 × 8.8
(B-3)					7 × 5	9.8 × 7.3
(B-4)					6 × 4	7.0 × 5.8
(C-1)	14	10	11	0.5	11 × 8	11 × 9.8
(C-2)					9 × 6	8.8 × 7.0
(C-3)					7 × 5	7.2 × 5.8
(C-4)					6 × 4	5.5 × 4.1
(D)	2.5	55	65 ($\lambda_1/2$)	0.5	2 × 2	7.5 × 12.5
	3	45	55 ($\lambda_2/2$)			
	4	35	45 ($\lambda_3/2$)			

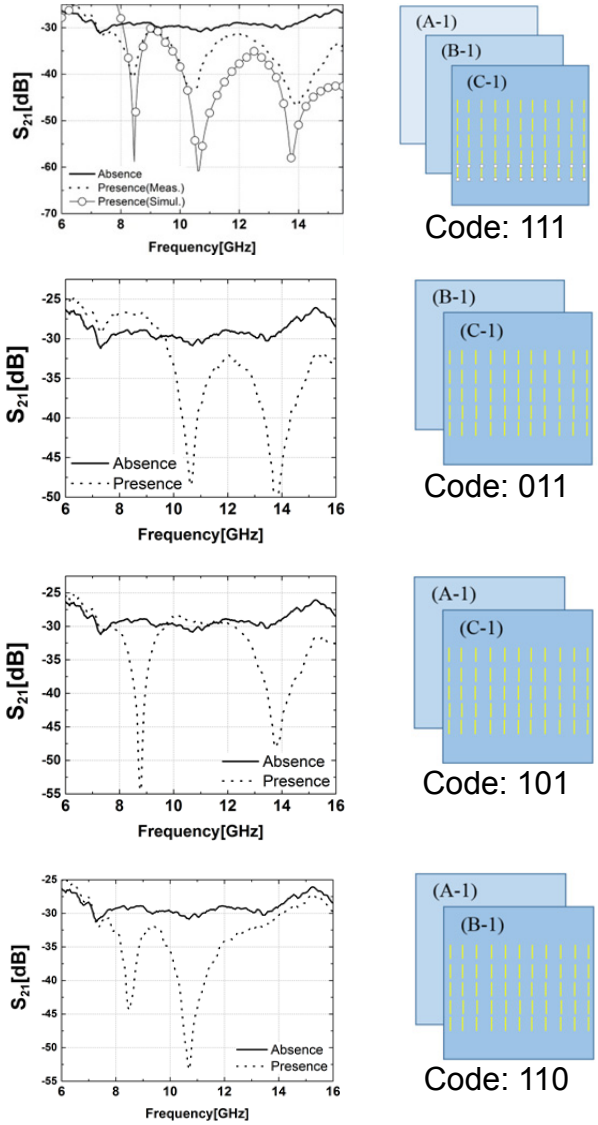

Fig. 6. Measured attenuation of 3-bit chipless RFID tags in SHF band.

agreement. The other measurements in Fig. 6 (codes '011', '101', and '110', respectively) were obtained using two different chipless RFID tags. The results reveal distinctive difference in S_{21} with a strong nulling effect, and also prove that the closely stuck tags did not cause any interference or frequency shift. However, the mutual coupling effect should be considered when expanding the number of bits.

Fig. 7 shows the attenuation in dB scale with respect to the number of dipole elements used in the array structure. The distance d is fixed at 1 m. The attenuation values in Fig. 7 are calculated by subtracting the present case of S_{21} values from the absent case. The 11 × 8 array tag presents up to 18 dB difference while the 6 × 4 array tag exhibits an average difference of 4 dB. A slight center-frequency shift is observed in Fig. 7. It is presumed that this is caused by a minor error in the measurement position or angle. Fig. 8 shows the measured attenuation with respect to distance variation, using tags (A-1) and (C-1) in

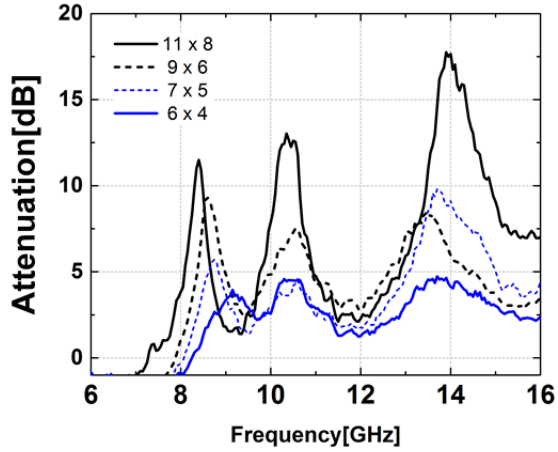

Fig. 7. Measured attenuation results with respect to the number of array elements.

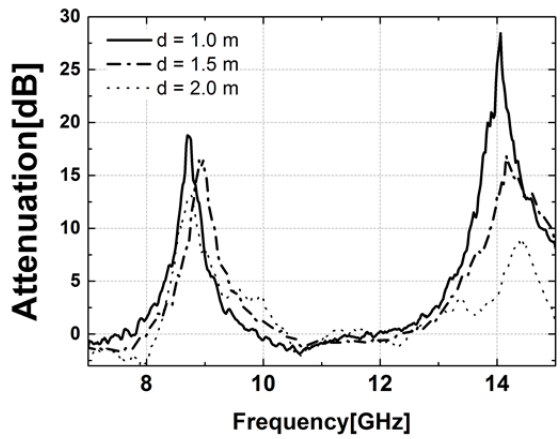

Fig. 8. Measured attenuation with respect to distance d using tags (A-1) and (C-1).

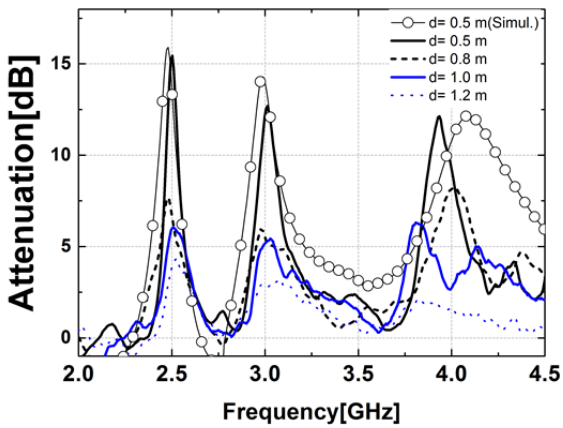

Fig. 9. Measured attenuation of 3-bit chipless RFID tag in UHF band using tag (D).

Table 1. The results indicate that RFID tags create more than 10 dB difference when d varies from 1 to 2 meters. Furthermore, the attenuation values gradually decrease as d increases. Fig. 9 shows the simulated and measured attenuation values for the RFID tag operating in the UHF and SHF bands. Tag (D) in Table 1 is used, and the distance d is varied from 0.5 m to 1.2 m.

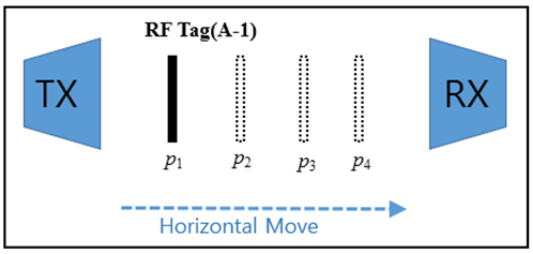

Fig. 10. Measurement setup for various RFID tag positions, P_N.

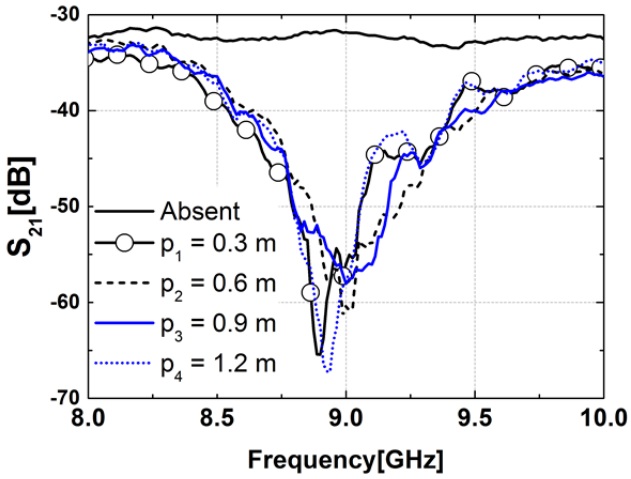

Fig. 11. Measured result for various RFID tag positions, P_N.

This type of design supports 3 bits of encoding capacity with a single layer of printed paper. The simulated and measured results at a distance of 0.5 m show relatively positive agreement. Meanwhile, an average 5 dB difference is observed at a distance of 1 m.

Fig. 10 shows the measurement setup with respect to the different positions of the RFID tags. The distance, *d*, is fixed at 1.5 m. Tag (A-1) in Table 1 is used in this test. Each position P_N denotes the distance from the Tx antenna. The measured S_{21} values are given in Fig. 11 with respect to position variation. The results indicate that changing the position of the tag horizontally does not affect frequency shift.

V. Conclusion

This study presented a fully printable chipless RFID system with a dipole array structure. We enhanced the reading range up to 2 m, which is 5 to 10 times further than earlier studies [9, 11]. The tags were printed on eco-friendly paper using conductive ink. The dipole array structure played an important role in increasing the gain of the passive tags, and compensated for the low conductivity of the conductive ink while maintaining the low transmission power of 0 dBm. It was shown that various combinations of multi-layer tags can provide up to 6 bits of information. Additionally, we verified that the tags can be designed at any desired frequency within the UHF and SHF bands. In conclusion, the proposed chipless RFID system, with its low cost, eco-friendly application, and longer reading range, showed great potential to replace current RFID systems.

References

[1] M. W. Cardullo and W. L. Parks, "Transponder apparatus and system," U.S. Patent 3 624 125, July 16, 1970.

[2] S. Preradovic and N. C. Karmakar, "Chipless RFID: bar code of the future," *IEEE Microwave Magazine*, vol. 11, no. 7, pp. 87-97, 2010.

[3] I. Jalaly and I. D. Robertson, "RF barcodes using multiple frequency bands," in *Proceedings of IEEE MTT-S International Microwave Symposium Digest*, Long Beach, CA, 2005.

[4] S. Preradovic and N. C. Karmakar, "Design of fully printable planar chipless RFID transponder with 35-bit data capacity," in *Proceedings of the 39th European Microwave Conference (EuMC)*, Rome, Italy, 2009, pp. 13-16.

[5] S. Preradovic, I. Balbin, N. C. Karmakar, and G. F. Swiegers, "Multiresonator-based chipless RFID system for low-cost item tracking," *IEEE Transactions on Microwave Theory and Techniques*, vol. 57, no. 5, pp. 1411-1419, 2009.

[6] A. Rida, L. Yang, R. Vyas, and M. M. Tentzeris, "Conductive inkjet-printed antennas on flexible low-cost paper-based substrates for RFID and WSN applications," *IEEE Antennas and Propagation Magazine*, vol. 51, no. 3, pp. 13-23, 2009.

[7] S. Kim, A. Traille, H. Lee, H. Aubert, K. Yoshihito, A. Georgiadis, C. Manos, and M. M. Tentzeris, "Inkjet-printed sensors on paper substrate for agricultural applications," in *Proceedings of IEEE European Microwave Conference (EuMC)*, Nuremberg, Germany, 2013, pp. 866-869.

[8] P. Hajizadeh, H. R. Hassani, and S. H. Sedighy, "Planar artificial transmission lines loading for miniaturization of RFID printed Quasi-Yagi antenna," *IEEE Antennas and Wireless Propagation Letters*, vol. 12, pp. 464-467, 2013.

[9] A. Vena, E. Perret, S. Tedjini, G. E. P. Tourtollet, A. Delattre, F. Garet, and Y. Boutant, "Design of chipless RFID tags printed on paper by flexography," *IEEE Transactions on Antennas and Propagation*, vol. 61, no. 12, pp. 5868-5877, 2013.

[10] H. S. Jang, W. G. Lim, K. S. Oh, S. M. Moon, and J. W. Yu, "Design of low-cost chipless system using printable chipless tag with electromagnetic code," *IEEE Microwave and Wireless Components Letters*, vol. 20, no. 11, pp. 640-642, 2010.

[11] S. Preradovic and A. Menicanin, "Printed 3-D stacked chipless RFID tag with spectral and polarization encoding capacity," in *Proceedings of 2016 39th International Spring Seminar on Electronics Technology (ISSE)*, Pilsen, Czech

Republic, 2016, pp. 500-505.
[12] C. Yu, W. Hong, and Z. Kuai, "Substrate integrated waveguide power divider fed dual-dipole array antenna," *Journal of the Korean Institute of Electromagnetic Engineering*, vol. 10, no. 3, pp. 171-174, 2010.
[13] J. P. Kim and C. W. Lee, "Short-ended electro-magnetically coupled coaxial dipole array antenna," *Journal of the Korean Institute of Electromagnetic Engineering*, vol. 2, no. 2, pp. 87-92, 2002.
[14] B. S. Cook and A. Shamim, "Inkjet printing of novel wideband and high gain antennas on low-cost paper substrate," *IEEE Transactions on Antennas and Propagation*, vol. 60, no. 9, pp. 4148-4156, 2012.
[15] L. Yang and M. M. Tentzeris, "3D multilayer integration and packaging on organic/paper low-cost substrates for RF and wireless applications," in *Proceedings of International Symposium on Signals, Systems and Electronics (ISSSE)*, Montreal, Canada, 2007, pp. 267-270.
[16] L. Yang, A. Rida, R. Vyas, and M. M. Tentzeris, "RFID tag and RF structures on a paper substrate using inkjet-printing technology," *IEEE Transactions on Microwave Theory and Techniques*, vol. 55, no. 12, pp. 2894-2901, 2007.

Not include authors' biography and photo.

JOURNAL OF ELECTROMAGNETIC ENGINEERING AND SCIENCE, VOL. 17, NO. 3, 165~167, JUL. 2017

http://dx.doi.org/10.5515/JKIEES.2017.17.3.165
ISSN 2234-8395 (Online) · ISSN 2234-8409 (Print)

Prediction of Electromagnetic Wave Propagation in Space Environments Based on Geometrical Optics

Changseong Kim · Yong Bae Park*

Abstract

We predict the electromagnetic wave propagation in space environments using geometrical optics. The effective indices of the troposphere, stratosphere, and ionosphere are computed, and the reflection, refraction, and attenuation of electromagnetic waves in space environments are calculated based on the ray tracing technique and geometrical optics. The influence of the refractive index and loss of atmosphere and the incident angle of the antenna on electromagnetic wave propagation is discussed.

Key Words: Electromagnetic Wave Propagation, Geometrical Optics, Ray Tracing Technique, Space Environment.

I. INTRODUCTION

In order to model the communication channel between terrestrial antennas and satellites, the influence of the space environment on electromagnetic (EM) wave propagation should be considered. The space environment consists of the atmosphere and the vacuum atmosphere. The altitude of the atmosphere is about 1,000 km from the ground. The atmosphere consists of a number of layers, including the troposphere, the stratosphere, the mesosphere, and the thermosphere. The ionosphere, a region of Earth's upper atmosphere, ranges from about 60 km to 1,000 km altitude. It is ionized by solar radiation and plays an important role in atmospheric electricity, forming the inner edge of the magnetosphere. EM wave propagation through the atmosphere is affected by variations in the refractive indices of each atmospheric layer. The refractive index depends on the altitude, and the EM wave is reflected, refracted, and attenuated when it propagates through the atmosphere. The ray tracing technique and high-frequency EM analysis methods such as geometrical optics are needed to evaluate these propagation characteristics.

Ionosonde, coherent scattering radar (CSR), interplanetary scintillation (IPS), and solar flux monitors are used to observe the space propagation environment [1, 2]. The prediction of EM wave propagation between terrestrial antennas and satellites using high-frequency EM analysis methods has been studied for a 1:1,000 scale model [3]. However, no study has presented a prediction for an actual-size earth space model.

In this paper, we propose a prediction method for EM wave propagation between terrestrial antennas and geostationary orbit (GEO) satellites based on geometrical optics. In order to predict EM wave propagation in space environments, it is necessary to calculate the refractive indices of the troposphere and the stratosphere, and the reflection and transmission of EM waves at the interfaces of the spheres. We use the ray tracing technique and geometrical optics to calculate EM wave propagation at the interface between the troposphere, the stratosphere, and the ionosphere, and analyze the EM wave characteristics in

Manuscript received June 12, 2017 ; Revised July 12, 2017 ; Accepted July 12, 2017. (ID No. 20170612-025J)
Department of Electrical and Computer Engineering, Ajou University, Suwon, Korea.
*Corresponding Author: Yong Bae Park (e-mail: yong@ajou.ac.kr)

a space environment.

II. PROPAGATION IN A SPACE ENVIRONMENT

We calculate the refractive index according to the altitude. The refractive indices of the troposphere and the stratosphere can be approximated by Eqs. (1) and (2) in [3]. The refractive index is determined by temperature, pressure, and water vapor pressure.

Fig. 1 shows Osan, South Korea's refractive index from 0 to 50 km, calculated using weather information from the University of Wyoming [4]. Since the ionosphere has a plasma ion layer, it affects the attenuation and refraction of EM waves [5]. Table 1 shows the relative permittivity and electrical conductivity considering the atmospheric environments, including the ionosphere [6]. The relative permeability of the atmosphere is assumed to be 1 and the anisotropy of the electrical conductivity of the ionosphere is not considered.

Fig. 2 shows the geometrical optics model when a ray passes through several atmospheric layers. The intersection between the ray and the interface is determined to calculate the transmission of the wave at the interface. We resolve the arbitrarily polarized incident wave into components parallel and perpendicular to the plane of incidence and calculate the reflection and transmission coefficients of each component.

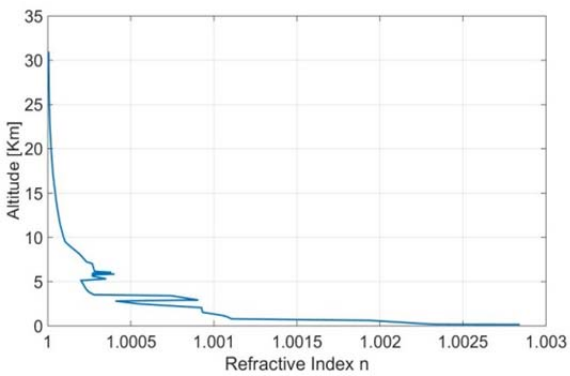

Fig. 1. Refraction index of the troposphere and stratosphere (May 22, 2017, Osan, South Korea).

Table 1. Relative permittivity and conductivity of the atmosphere

Altitude (km)	ε_r	σ
0–10	1.003	10^{-14}
10–20	1.0002	10^{-13}
20–50	1	10^{-12}
50–100	1	10^{-11}
100–120	0.9999	10^{-6}
120–400	1	10^{-10}
400–35,768	1	10^{-20}

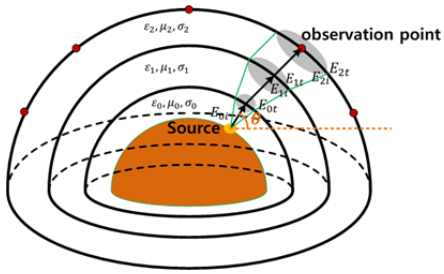

Fig. 2. Geometrical optics model in a space environment.

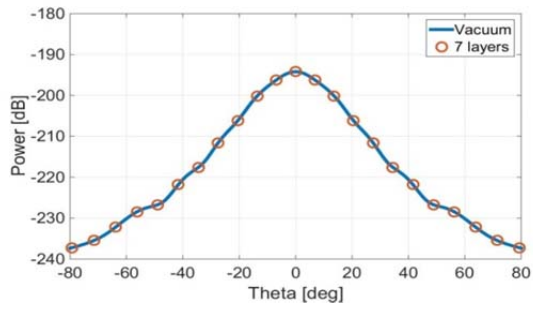

Fig. 3. Radiation pattern of the antenna using geometrical optics ($\varepsilon_r = 1, \sigma = 0$).

Geometrical optics is a high-frequency method that approximates the incidence, reflection, and refraction of EM fields. Using the following formula, the EM field at the observation point can be calculated using the EM field of reference point, the spatial attenuation factor, and the phase factor [7, 8].

$$\mathbf{E}(s) = \mathbf{E_0}(0)e^{j\phi_0(0)}\sqrt{\frac{dA_0}{dA}}e^{-\alpha s}e^{-j\beta s}. \tag{1}$$

In order to check the accuracy of the proposed method, we compare the radiation pattern of the antenna itself with the radiation pattern of the antenna considering the seven layers of the atmosphere with the same refractive index ($\varepsilon_r = 1, \sigma = 0$) from the ground to the GEO satellite. We use a pyramidal horn antenna with an operating frequency of 10 GHz, a maximum gain of 18.8 dB, and an incident power of 1.2 dBm. Fig. 3 shows good agreement between the two cases.

III. CALCULATION RESULTS

We calculate the radiation pattern of the above antenna in a space environment based on Table 1. Figs. 4 and 5 show the radiation patterns when the direction of the antenna is perpendicular to the ground and when the direction of the antenna is at 30° with respect to the ground, respectively.

Note that the position of the main beam is not changed and the maximum power is reduced by 32.72 dB in Fig. 4. In Fig. 5,

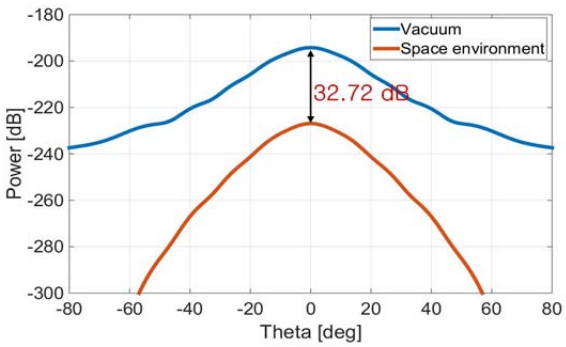

Fig. 4. Radiation pattern of an antenna in a space environment (angle between ground and incidence vector = 90°).

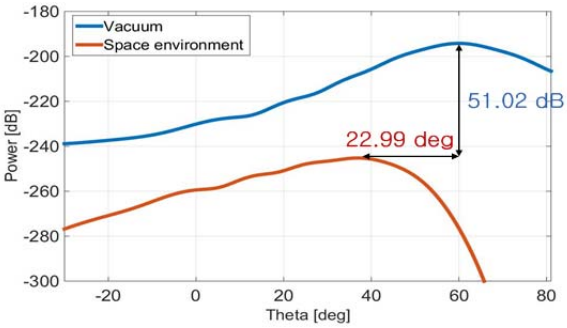

Fig. 5. Radiation pattern of an antenna in a space environment (angle between ground and incidence vector = 30°).

the position of the main beam shifts from 60° to 37.01° and the maximum power is reduced by 51.02 dB. This is because the refraction at the interface and the attenuation along the path are different when the incident angles of the antenna are different.

Since Table 1 roughly divides the atmosphere, it is necessary to divide the atmosphere more precisely for more accurate predictions. In addition, EM wave propagation in the ionosphere should be analyzed more accurately using full-wave EM analysis such as finite-difference time-domain method (FDTD).

IV. Conclusion

We have calculated the reflection, refraction, and transmission of EM waves using the ray tracing technique and geometrical optics in space propagation environments. We have shown that EM wave propagation in space environments depends on the refractive index and loss of atmosphere and the incident angle of the antenna. It is necessary to accurately monitor the atmospheric state of the atmosphere, including the ionosphere, and to calculate the refractive index and loss of atmosphere for accurate prediction of EM wave propagation in space environments. Our method is useful to calculate EM wave propagation for an actual-size earth space model, unlike full-wave analysis such as FDTD and method of moments.

This work was supported by the research fund of Signal Intelligence Research Center, supervised by the Defense Acquisition Program Administration and Agency for Defense Development of Korea.

References

[1] J. M. Smith, F. S. Rodrigues, B. G. Fejer, and M. A. Milla, "Coherent and incoherent scatter radar study of the climatology and day-to-day variability of mean F region vertical drifts and equatorial spread F," *Journal of Geophysical Research: Space Physics*, vol. 121, no. 2, pp. 1466–1482, 2016.

[2] E. Aguilar-Rodriguez, M. Rodriguez-Martinez, E. Romero-Hernandez, J. C. Mejia-Ambriz, J. A. Gonzalez-Esparza, and M. Tokumaru, "The wavelet transform function to analyze interplanetary scintillation observations," *Geophysical Research Letters*, vol. 41, pp. 3331-3335, 2014.

[3] C. Kim and Y. B. Park, "Prediction of antenna propagation characteristic in space environment using ray tracing method," *Journal of Korean Institute of Electromagnetic Engineering and Science (JKIEES)*, vol. 27, no. 11, pp. 1023–1026, 2016.

[4] University of Wyoming, Department of Atmospheric Science, "Atmospheric soundings," [Online]. Available: http://weather.uwyo.edu/upperair/sounding.html.

[5] C. H. Papas, *Theory of Electromagnetic Wave Propagation*. New York, NY: Dover Publications, 2014.

[6] J. M. Rosen and D. J. Hofmann, "Balloon-borne measurements of electrical conductivity, mobility, and the recombination coefficient," *Journal of Geophysical Research*, vol. 86, no. C8, pp. 7406–7410, 1981.

[7] C. A. Balanis, *Advanced Engineering Electromagnetics*, 2nd ed. Hoboken, NJ: John Wiley & Sons, 2012.

[8] S. Y. Kim, "Review of the hidden rays of diffraction," *Journal of Electromagnetic Engineering and Science*, vol. 15, no. 1, pp. 1–5, 2015.

JEES Journal of Electromagnetic Engineering and Science

Instructions for Authors

Journal of Electromagnetic Engineering and Science (*J. Electromagn. Eng. Sci.*; *JEES*) is an official English journal of the Korean Institute of Electromagnetic and Engineering Science (KIEES). The objective of *JEES* is to publish academic as well as industrial research results and foundings on electromagnetic engineering and science. The journal covers all aspects of researches and technology related to electromagnetics: Electromagnetic Compatibility/Electromagnetic Interference, Microwave and Millimeter-Wave Engineering, Antenna and Propagation, Electromagnetic Theory, Wireless Communication, Lightwave and Electro-Optics, Materials and Components, Software Defined Radar, Radar, Bioelectromagnetics, and etc.

I. Copyright and Creative Commons Attribution Licensing

The copyright and the transfer rights of the digital content of published papers and the journal is owned by the KIEES. All published materials are also assigned a Creative Commons Attribution License (http://creativecommons.org/licebses/by-nc/3.0/). The journal accepts manuscripts for consideration with the understanding that the manuscript has not been published previously and is not currently under consideration for publication elsewhere, and in addition, that the authors (or their employer, if it holds the copyright) are authorizing the transfer of the copyright to the Institute when the manuscript is submitted. Author should check the copyright transfer conditions and forms at http://www.jees.kr.

II. Research and Publication Ethics

Research published in *JEES* must have followed institutional, national, and international guidelines. For policies on research and publication ethics that are not stated in these instructions, please refer to the *Committee on Publication Ethics* (*COPE*) *Guidelines* (http://publicationethics.org/resources/code-conduct).

1. Originality and Duplicate Publication

A manuscript submitted for publication in *JEES* should be an original work with technical values. It must not have been previously published and is not under consideration for publication elsewhere. *JEES* assumes that the materials submitted for its publications are properly available for general dissemination for the readership of those publications. It is the responsibility of the authors, not *JEES*, to determine whether disclosure of their materials requires prior consent of other parties and, if so, to obtain it. If an author uses charts, photographs, or other graphics from any previously printed materials, he/she is responsible for obtaining written permissions from the publisher to use them in his/her manuscript. Responsibility for the contents of published papers rests upon the authors, not *JEES*.

2. Conflict of Interest

Authors are required to complete a declaration of conflict of interests. All conflict of interests that are declared will be listed at the end of published articles.

3. Authorship

Authorship should be restricted to those individuals who have met each of the following three criteria:
1) made a significant contribution to the conception and design of the project, or the analysis and interpretation of the data, or other substantial scholarly effort; 2) participated in drafting, reviewing and/or revising the work; and 3) approved the final version for publication. After the initial submission of a manuscript, any changes whatsoever in authorship (adding author(s), deleting author(s), or re-arranging the order of authors) must be explained by a letter to the editor from the authors concerned. The content of this

letter must be acknowledged and agreed upon by all of the authors of the paper.

If you accept the policies on research and publication issued by KIEES, authors must click the response of "The Code of Research Ethics" through online.

III. Submission of Manuscripts

Authors are expected to be members of the KIEES except for some special cases approved by the Editorial Board of KIEES. All manuscripts should be submitted electronically through the online submission and review site (https://mc03.manuscriptcentral.com/jees). For the first submission, you may be required to create an account on the submission site. A manuscript can be submitted at any time of the year. When submitting a manuscript, authors need to make sure that their manuscripts do not provide any of their identities such as authors' names and affiliations as the review is double-blinded. More detailed submission instruction is available in the upper right corner of the submission site. All manuscripts submitted to the Journal must comply with the instruction and the standard format of the Journal. Otherwise, it will result in return of the manuscript and possible delay in publication. For assistance, please contact us via e-mail (admin-jees@kiees.or.kr).

IV. Peer Review Process

The manuscript will be forwarded to three reviewers selected for their expertise in the field of the submitted manuscript. The acceptance criteria for all papers are based on the quality and originality of the research and its clinical and scientific significance. During the review process, the author is often asked to expand, rewrite, or clearly explain the specific contents of his/her paper. It is not uncommon that an author is asked to provide another draft with the suggested changes for further review. A revised manuscript should be submitted to the homepage within a month from the date on which any change of the manuscript is requested to the author. Once a manuscript has received the final approval of the reviewers and Editor-in-Chief, the author will be notified and asked to prepare the manuscript for final publication and to possibly complete an additional information form.

V. Publication Type

The papers are classified into five categories.

Regular Paper should be an original work that contributes to the academic interests of the KIEES members with technical values. The paper should also be written within 12 pages with A4 size including figures, charts, and tables (The main body of text consists of two columns).

Letter consists of reports of preliminary results or short reports on completed work that are of current interest to many researchers in the field. Comments on material previously published in the journal, suggestions for new directions, and errata could be included. Their length must be less than 3 pages (with a two-column format) including paper title, author affiliation, reference, etc.

Review Paper will be published by direct submission as well as from invited experts. In both cases, the work will be subject to editorial review. Review papers should critically review topics not only to inform the reader of the background, but also to communicate the state of the art and outstanding research problems.

Technical Report is on innovative technical achievements of interest to the community and usually a report of an extensive series of measurements. Report is often involving display in the form of tables or graphs, with text describing the conditions and procedures of measurement.

Editorial is a brief report of research findings adequate for the journal's scope and of particular interest to the community.

VI. Manuscript Preparation

All manuscripts must be written in MS-Word and adhere to the following guidelines:

1. A cover of each paper manuscript should include a title, authors' names (main author and co-authors), author's organizations, contact information (e-mail and phone number), and the author's area of expertise.
2. The first page of a main text should only contain title, abstract with a length of about 150 words, and key words with around five words.
3. The contents of the manuscript should be arranged in the order of abstract, main text, acknowledgments, references, and appendix.
4. The numbers corresponding to chapters in the manuscript should be written in Roman numerals (I, II, III, IV...) and the numbers corresponding to sections should be written in Arabic numerals (1, 2, 3, 4...).
5. Equation numbers should be given in Arabic numerals enclosed in parentheses on the right-hand margin. They should be cited in the text as, for example Eq. (1) or Eqs. (1)-(3).
6. All tables should be numbered consecutively with Arabic numerals. They should be referred to in the text and should be numbered according to their order of mention in the text. In addition, all tables should, not only list all abbreviations in the table in footnotes at the end, but also have a title that is concise and describes the table's contents. Vertical lines are not used. The table should be self-explanatory and supplement, not duplicate, the text. If the table or any data therein have been published, a footnote to the table must give permission information to the original source. The structure should be clear, with simple column headings giving all units. A table should not exceed one page when printed. Use lowercase letters in superscripts $^{a,b,c...}$ for special remarks.
7. All figures should be of high quality meeting with the publishing requirement with legible symbols and legends. In preparing the figures, authors should consider a size reduction during the printing process to have acceptable line clarity and character sizes. Use only figures that are necessary to illustrate the meaning of the text. Figures must be black and white of high contrast. All figures should be referred to in the text as, for example, Fig. 1, Fig. 2(a), or Figs. 1-3.
8. Only those references cited in the text should be listed in the references. Authors are responsible for the accuracy and completeness of their references and the correct text citations. In the text the reference should be numbered in bracket in ascending order (e.g., [1, 3], or [4-6]; Lee [2] and Kim and Park [5]; Jang et al. [7]). In case of the paper title, only the first letter is to be capitalized. However, in case of journal and book titles, the first letter of each word should be capitalized and all of the letters should be italicized. See the example below.

Books

[1] F. Giannini and G. Leuzzi, *Nonlinear Microwave Circuit Design.* NewYork, NY: John Wiley & Sons Inc., 2004.

Journals

[2] H. Ahn and B. Kim, "Equivalent transmission-line sections for very high impedances and their application to branch-line hybrids with very weak coupling power," *Journal of Electromagnetic Engineering and Science*, vol. 9, no. 2, pp. 85-97, Jun. 2009.

Report

[3] E. E. Reber, R. L. Michell, and C. J. Carter, "Oxygen absorption in the earth's atmosphere," Aerospace Corp., Los Angeles, CA, Tech. Rep. TR-0200 (4230-46)-3, Nov. 1988.

Conference Proceedings

[4] S. P. Bingulac, "On the compatibility of adaptive controllers," in *Proceedings of the 4th Annual Allerton Conference on Circuit and System Theory*, NewYork, pp. 8-16, 1994.

Papers Presented at Conferences

[5] J. G. Kreifeldt, "An analysis of surface-detected EMG as an amplitude-modulated noise," presented at the 8th International Conference on Medical and Biological Engineering, Chicago, IL, 1969.

[6] J. Arrillaga and B. Giessner, "Limitation of short-circuit levels by means of HVDC links," presented at the IEEE Summer Power Meeting, Los Angeles, CA, Jul. 1990.

Theses (M.S.) and Dissertations (Ph.D.)

[7] N. Kawasaki, "Parametric study of thermal and chemical nonequilibrium nozzle flow," M.S. thesis, Department of Electronic Engineering, Osaka University, Osaka, Japan, 1993.

[8] J. O. Williams, "Narrow-band analyzer," Ph.D. dissertation, Department of Electronic Engineering, Harvard University, Cambridge, MA, 1993.

Standards

[9] *IEEE Criteria for Class IE Electric Systems*, IEEE Standard 308, 1969.

Online Sources

[10] R. Bartle, "Early MUD History," Nov. 1990; www.ludd.luth.se/aber/mud-history.html.

9. When citing any paper published in JEES, it should be indicated the name of the journal as *Journal of Electromagnetic Engineering and Science* or *J. Electromagn. Eng. Sci*.

10. Acknowledgment, if needed, appears before the reference. Sponsorship or financial support acknowledgment should be included here.

11. Unit and Abbreviation:If the authors describe length, height, weight, and volume, they should use standard metric units. Temperature should be given in degrees Celsius. All other units should follow the International System of Units (SI). All units must be preceded by one space except percentages (%) and temperatures (°C).

Abbreviations must be used as an aid to the reader, rather than as a convenience of the author, and therefore their use should be limited. Generally, abbreviations that are used less than 3 times in the text, including tables and figure legends, should be avoided. Standard SI abbreviations are recommended. Other common abbreviations are as follows (the same abbreviations are used for plural forms): h (hour), min (minute), s (second), d (day), wk (week), mo (month), y (year), L (liter), mL (milliliter), μL (microliter), g (gram), kg (kilogram), mg (milligram), μg (microgram), ng (nanogram), pg (picogram), *g* (gravity; not g), nm (nanometer), μm (micrometer), mV (millivolt), mA (milliampere), mW (milliwatt), C (coulomb), μF (microfarad), mH (millihenry), n (samplesize), SD (standard deviation of the mean), and SE (standard error of the mean).

VII. Accepted Manuscript

Once the review process has been completed with a decision of acceptance, the final manuscript accommodating all of the reviewers' comments should be submitted along with photos of the authors and their brief biographies (including major research areas). The accepted papers will be published, in principle, in the order of initially submitted dates subject to decision of the Editorial Board.

1. Page Proofs

Authors will be given an opportunity to review the laser printed version of their manuscripts before printing. One set of page proofs in PDF format will be sent by e-mail to the corresponding author. The review should be solely dedicated to detecting typographical errors.

2. Publishing Charge

The publishing charge for general publishing is KRW 150,000 (US$150) for up to the first 6 pages. For 7 to 8 pages, an extra charge of KRW 30,000 (US$30) per page, and for 9 pages or more, an extra charge of KRW 40,000 (US$40) per page. Furthermore, the KIEES charges extra KRW 100,000 (US$100) for the paper acknowledging a financial support from an institution, in addition to the above mentioned page charge. Twenty reprints without a cover will be supplied without an additional charge.

Contact Us

Editorial office of the Korean Institute of Electromagnetic Engineering and Science
217, Saechang-ro, Yongsan-gu, Seoul, 04376, Korea
Tel: +82-2-337-9666/332-9665 Fax: +82-2-6390-7550
http://www.jees.kr, E-mail: admin-jees@kiees.or.kr

AUTHOR CHECKLIST

Title : _____

General

☐ This paper has not been and will not be published in any other journal.

☐ This paper follows the format of the KIEES paper submission guideline, is less than 12 pages long, including figures and tables (3 pages for a letter), and has a two-column layout.

☐ This paper includes a cover page, an abstract, keywords, main text, appendix, and references in the correct order. Each page has a consecutive page number.

Cover page

☐ The cover page includes the title, authors, affiliation of all authors, identifier of the corresponding author, and provides contact information for the corresponding author (phone number, e-mail address, and mobile number).

Abstract and key words

☐ An abstract is provided and is less than 500 words long.

☐ Fewer than 5 keywords are provided.

Main text

☐ The reference number is written next to the quote.

☐ The chapter numbers are written in Roman numerals (I, II, III, IV…) and subheading numbers are written in Arabic numerals (1, 2, 3, 4…).

References

☐ Sufficient Korean as well as international literature is referenced in the paper.

☐ Only the references used in the main text are included in the reference list and these are numbered according to their order of appearance.

☐ All reference citations follow the correct format indicated in the submission regulations.

Figures and tables

☐ For the figures and tables, the first letter of the very first word is capitalized.

☐ All figure legends include both a title and a detailed explanation to help in understanding what the figure depicts.

☐ All tables are self-explanatory and do not repeat the content from figures or sources included in the main text.

* Check each box after confirming that the statement is true.

The authors of this paper have confirmed the above items, following the paper submission regulations of *the Korean Institute of Electromagnetic Engineering and Science (KIEES)*, and are requesting publication of this paper.

_____/_____/ 2017

Representative author: _____ (signature)

Journal of Electromagnetic Engineering and Science

http://www.jees.kr

JEES
Volume 17, Number 3,
July, 2017

INVITED PAPER

REGULAR PAPERS

LETTER